

AN ABSTRACT OF THE DISSERTATION OF

YOONSUK KIM for the degree of Doctor of Philosophy in Electrical and Computer Engineering presented on JUNE 3, 1999.

Title: CHARACTERIZATION OF COUPLED MICROSTRIP
STRUCTURE USING FDTD

Redacted for privacy

Abstract approved: _____

Vijai K. Tripathi

Redacted for privacy

Abstract approved: _____

Andreas Weisshaar

A new CAD-oriented methodology for the full-wave broadband characterization of coupled microstrip structures for RF/microwave and high-speed digital circuits is presented. The characterization methodology is based on the finite difference time domain (FDTD) technique combined with a systematic extraction procedure using the normal mode approach and multiport network concepts.

The characterization approach is first applied to uniform coupled lines on a lossless substrate to determine their frequency-dependent propagation characteristics. The $2n$ -port admittance matrix corresponding to n uniform coupled lines is extracted from the port voltages and currents, which in turn provides the frequency-dependent distributed inductance and capacitance matrices. To illustrate the technique, several typical coupled line structures, including an asymmetric three-line structure, are analyzed. Comparison with results obtained with a full-wave spectral domain method shows good agreement.

The new characterization methodology is applied to microstrip lines on lossy silicon substrate. The frequency-dependent propagation characteristics and dis-

tributed line parameters for single and symmetric coupled microstrip lines are extracted from FDTD simulation. Results show that the lossy substrate can significantly affect the transmission line characteristics. To reduce the substrate effects on the microstrip characteristics, a new substrate shielding structure consisting of orthogonal grounded lines at the silicon/oxide interface is examined. It is shown for a single and symmetric coupled microstrip lines that the substrate shield leads to a reduction in transmission line loss without significantly changing the characteristic impedance and effective permittivity of the microstrip structure.

Using the FDTD approach combined with a new extraction procedure, the characteristics of several discontinuities in single and coupled microstrip lines are determined. The new extraction procedure for characterizing discontinuities is based on successive excitation of each port and determination of the voltages for the incident and reflected waves. The method is applied to several example structures including coupled step and coupled gap discontinuities.

©Copyright by YOONSUK KIM

JUNE 3, 1999

All Rights Reserved

CHARACTERIZATION OF COUPLED MICROSTRIP
STRUCTURE USING FDTD

by
YOONSUK KIM

A DISSERTATION
submitted to
Oregon State University

in partial fulfillment of the
requirements for the degree of
Doctor of Philosophy

Completed JUNE 3, 1999
Commencement June 2000

Doctor of Philosophy dissertation of YOONSUK KIM presented on JUNE 3, 1999

APPROVED:

Redacted for privacy

Co-Major Professor, representing Electrical and Computer Engineering

Redacted for privacy

Co-Major Professor, representing Electrical and Computer Engineering

Redacted for privacy

Head of Department of Electrical and Computer Engineering

Redacted for privacy

Dean of Graduate School

I understand that my dissertation will become part of the permanent collection of Oregon State University libraries. My signature below authorizes release of my dissertation to any reader upon request.

Redacted for privacy

YOONSUK KIM, Author

ACKNOWLEDGEMENTS

I would like to express my sincere thanks to Dr. Vijai K. Tripathi, my major professor, for his guidance, advice, patience, encouragement and support throughout my Ph.D work.

Professors Dr. Ronald Mohler, Dr. Ben Lee, Dr. Andreas weisshaar, Dr. Raghu K. Settaluri and Dr. Goran Jovonovic are acknowledged for serving on my graduate committee and for reviewing the manuscript.

Appreciation is due to my fellow microwave group colleagues, Maynard Falconer, Alok Tripathi, Kate remly, Rick Lutz, Yeonchang Hahm, Garth Sundberg, Chiyoung Lim and Ji Zheng for their valuable assistance.

I wish to express my thanks gratitude to the KOREA AIR FORCE for financial support and the KOREA AIR FORCE ACADEMY for the opportunity to pursue this advance education.

I would like to give special thanks for the support and encouragement of all my family members, my mother, my brothers and sisters, my wife's parents, my wife's sisters and all of my friends, in memory of my father.

Final thanks is due to my wife MEEYOUNG, my daughters JIHAE, HAEREE and my son SOO for their understanding and help.

This research was supported in part by the National Science Foundation (NSF), the NSF Center for the Design of Analog and Digital Integrated Circuits (CDADIC) and the Oregon State University Graduate Research Assistanceship Program.

TABLE OF CONTENTS

	<u>Page</u>
1 INTRODUCTION	1
1.1 BACKGROUND	2
1.2 ORGANIZATION OF THE DISSERTATION	5
2 THE FINITE DIFFERENCE TIME DOMAIN METHOD	 7
2.1 INTRODUCTION	7
2.2 FDTD TECHNIQUE	8
2.3 NUMERICAL STABILITY	13
2.4 PERFECTLY MATCHED LAYER (PML) ABSORBING BOUND- ARY CONDITION	 14
2.5 IMPLEMENTATION OF THE FDTD	20
2.5.1 MICROSTRIP CONDUCTOR	23
2.5.2 MATERIAL BOUNDARY CONDITIONS	24
2.5.3 EXCITATION SOURCE	26
2.6 UNIFORM SINGLE MICROSTRIP LINE AS A SIMPLE EXAMPLE	 28
2.6.1 MODELING OF A SINGLE MICROSTRIP STRUC- TURE	 29
2.6.2 PROPAGATION CHARACTERISTICS	30
2.6.3 EQUIVALENT CIRCUIT MODEL	38
2.7 CONCLUDING REMARKS	39
3 CHARACTERIZATION OF MULTIPLE COUPLED LINE STRUC- TURES	 42
3.1 INTRODUCTION	42
3.2 EQUIVALENT CIRCUIT MODEL FOR NORMAL MODE APPROACH	 43

TABLE OF CONTENTS (CONTINUED)

	<u>Page</u>
3.3 ANALYSIS OF SYMMETRIC COUPLED LINES	50
3.4 ANALYSIS OF ASYMMETRIC COUPLED LINES	54
3.5 ANALYSIS OF ASYMMETRIC THREE COUPLED LINES	61
3.6 CONCLUDING REMARKS	62
4 TRANSMISSION LINES ON LOSSY SILICON SUBSTRATE	69
4.1 INTRODUCTION	69
4.2 SINGLE MICROSTRIP MIS STRUCTURE	72
4.3 SYMMETRIC COUPLED LINE MIS STRUCTURE	74
4.4 SINGLE MIS LINE WITH SUBSTRATE SHIELDING	81
4.5 SYMMETRIC COUPLED MIS LINES WITH SUBSTRATE SHIELDING	92
4.6 CONCLUDING REMARKS	92
5 MICROSTRIP DISCONTINUITIES	98
5.1 INTRODUCTION	98
5.2 NETWORK FORMULATION FOR DISCONTINUITIES	99
5.3 SINGLE LINE DISCONTINUITIES	102
5.3.1 MICROSTRIP OPEN-END DISCONTINUITY	102
5.3.2 MICROSTRIP STEP-IN-WIDTH	105
5.3.3 ASYMMETRIC MICROSTRIP GAP	107
5.3.4 MICROSTRIP CROSS-JUNCTION	107
5.4 COUPLED LINE DISCONTINUITIES	109
5.4.1 ASYMMETRIC COUPLED GAP	115
5.4.2 ASYMMETRIC COUPLED STEP-IN-WIDTH	115

TABLE OF CONTENTS (CONTINUED)

	<u>Page</u>
5.5 CONCLUDING REMARKS	119
6 CONCLUSION AND SUGGESTIONS FOR FUTURE WORK	123
BIBLIOGRAPHY	125
APPENDIX	136

LIST OF FIGURES

<u>Figure</u>	<u>Page</u>
2.1. Yee's unit cell	11
2.2. Perfect Electric Wall	17
2.3. Implementation of the FDTD	21
2.4. Modeling of a perfectly conducting microstrip	23
2.5. Effective dielectric constant	25
2.6. Effective conductivity constant	26
2.7. Resistive voltage source	27
2.8. Uniform single microstrip line structure including PML absorbing boundary cells.	28
2.9. Gaussian input source and its spectrum for the single microstrip example.	31
2.10. Voltage and current contours for a microstrip line.	32
2.11. (a) Different recording positions for voltage and current and (b) the average of the two currents.	33
2.12. Propagation waveform of single microstrip along the Z-direction at 600 and 800 timesteps, respectively.	35
2.13. Voltage and current waveforms at different positions: $50\Delta z$, $60\Delta z$, $70\Delta z$, $80\Delta z$, and $90\Delta z$ along the Z-direction.	36
2.14. Effective dielectric constant as a function of frequency (Solid: FDTD, Diamond: Static value).	37
2.15. Characteristic impedance as a function of frequency (Solid: FDTD, Diamond: Static value).	38
2.16. Equivalent circuit model for short section of a uniform single microstrip line.	39
2.17. Inductance and capacitance per unit length for a single microstrip as a function of frequency.	40
3.1. General multiconductor coupled lines	44

LIST OF FIGURES (CONTINUED)

<u>Figure</u>	<u>Page</u>
3.2. Flow chart for determine admittance matrix for a general $2n$ -port n multiple coupled line structure.	47
3.3. Procedure for determining the normal mode parameters of a $2n$ -port multiple coupled line structure.	49
3.4. Entire computational domain for multiple coupled line structure including PML absorbing boundary cells.	51
3.5. Propagation waveform along the Z-direction at 1200 time steps for symmetric coupled lines.	52
3.6. Propagation waveform along the Z-direction at 900 time steps for the odd-mode excitation of symmetric coupled lines.	53
3.7. The transient time (a) voltage and (b) current recorded on the active and sense line for symmetric coupled lines.	55
3.8. Comparison with two approaches (a) Characteristic impedance and (b) effective dielectric constant as functions of frequency for a symmetric coupled line structure.	56
3.9. (a) Inductance and (b) capacitance as functions of frequency for symmetric coupled lines.	57
3.10. Propagation waveform along Z-axis at 800 time steps for an asymmetric coupled line structure.	58
3.11. The transient time (a) voltage and (b) current recorded on the active and sense line for an asymmetric coupled line structure.	59
3.12. Comparison between FDTD and a full-wave spectral domain method of the characteristic impedance for an asymmetric coupled line structure.	60
3.13. Comparison between FDTD and a full-wave spectral domain method of effective dielectric constant for an asymmetric coupled line structure.	61

LIST OF FIGURES (CONTINUED)

<u>Figure</u>	<u>Page</u>
3.14. Comparison between FDTD and a full-wave spectral domain method of line-mode voltage ratio for an asymmetric coupled line structure.	62
3.15. (a) Inductance and (b) capacitance as functions of frequency for an asymmetric coupled line structure.	63
3.16. Propagation waveform along Z-direction at 900 time steps for an asymmetric three coupled line structure.	64
3.17. The transient (a) voltage and (b) current recorded on active line and two sense lines for a three coupled line structure.	65
3.18. Line mode characteristic impedance for a three coupled line structure.	66
3.19. Line mode effective dielectric constant for an asymmetric three coupled line structure (SPDM = full-wave spectral domain method).	66
3.20. Line mode voltage ratio for a three coupled line structure.	67
3.21. (a) Inductance and (b) capacitance as functions of frequency for a three coupled line structure.	68
4.1. (a) Single microstrip and (b) symmetric coupled microstrip MIS structure.	71
4.2. The distributed equivalent circuit for a single microstrip MIS structure.	72
4.3. (a) Effective dielectric constant and (b) characteristic impedance for a single MIS line for the substrate conductivity of $\sigma = 10(S/m)$	75
4.4. (a) Total inductance and (b) conductance for a single MIS line for the substrate conductivity of $\sigma = 10(S/m)$	76

LIST OF FIGURES (CONTINUED)

<u>Figure</u>	<u>Page</u>
4.5. (a) Total capacitance and (b) attenuation constant for a single MIS line structure for the substrate conductivity of $\sigma = 10(S/m)$	77
4.6. (a) Capacitance C_{ox} and (b) conductance G_{si} for a single MIS line for the substrate conductivity of $\sigma = 10(S/m)$	78
4.7. Capacitance C_{si} for a single MIS line for the substrate conductivity of $\sigma = 10(S/m)$	79
4.8. (a) Effective dielectric constant and (b) characteristic impedance for the symmetric coupled MIS structure.	82
4.9. (a) Total inductance and (b) conductance for the symmetric coupled MIS structure.	83
4.10. (a) Total capacitance and (b) attenuation constant for the symmetric coupled MIS structure.	84
4.11. (a) Side view and (b) top view of single microstrip MIS structure with embedded grounded cross bars for substrate shielding.	85
4.12. Computational domain for FDTD simulation of a single MIS line with a cross bar substrate shielding structure.	86
4.13. (a) Effective dielectric constant and (b) characteristic impedance for $\sigma = 10(S/m)$	88
4.14. (a) Total inductance and (b) conductance for $\sigma = 10(S/m)$	89
4.15. (a) Total capacitance and (b) attenuation constant for $\sigma = 10(S/m)$	90
4.16. (a) Quality factor(Q) as a function of frequency and (b) Quality factor(Q) with the normalized spacing for $\sigma = 10$ siemens/meter.	91
4.17. Computational domain in FDTD simulation of symmetric coupled lines with the cross bar shielding structure.	93

LIST OF FIGURES (CONTINUED)

<u>Figure</u>	<u>Page</u>
4.18. (a) Effective dielective constant and (b) Characteristic impedance for symmetric coupled lines with $\sigma = 10(\text{S/m})$	94
4.19. (a) Even- and odd-mode inductance and (b) conductance for a symmetric coupled line structure with substrate conductivity $\sigma=10(\text{S/m})$	95
4.20. (a) Even- and odd-mode capacitance and (b) attenuation constant for symmetric coupled line structure with substrate conductivity $\sigma=10(\text{S/m})$	96
5.1. Various kinds of single microstrip discontinuities.	100
5.2. n-port network with different characteristic impedances.	101
5.3. Single open-end structure with uniform reference line.	103
5.4. (a) Monitored voltage waveform and (b) scattering parameter for open-end structure.	104
5.5. (a) Two-port network for scattering parameters and (b) single step-in-width structure.	106
5.6. (a) Magnitude and (b) phase of scattering parameters for single step-in-width structure.	108
5.7. Asymmetric gap structure.	109
5.8. (a) Magnitude and (b) phase for the asymmetric gap structure.	110
5.9. Four-port network for the scattering parameters.	111
5.10. (a) Symmetric cross-junction structure and (b) monitored voltages	112
5.11. Propagation of waveform at 900 time steps for symmetric cross-junction structure.	113

LIST OF FIGURES (CONTINUED)

<u>Figure</u>		<u>Page</u>
5.12.	(a) Magnitude and (b) phase of scattering parameters for symmetric cross-junction structure.	114
5.13.	Asymmetric coupled gap structure.	115
5.14.	propagation waveform at 1500 time steps of asymmetric coupled gap.	116
5.15.	(a) Magnitude and (b) phase of scattering parameters for asymmetric coupled gap.	117
5.16.	(a) Magnitude and (b) phase of scattering parameters for asymmetric coupled gap.	118
5.17.	Asymmetric coupled step-in-width structure.	119
5.18.	Propagation waveform at 1200 time steps for asymmetric coupled step-in-width structure.	120
5.19.	(a) Magnitude and (b) phase of asymmetric coupled step structure at port 1 excitation.	121
5.20.	(a) Magnitude and (b) phase of asymmetric coupled step structure at port 2 excitation.	122

CHARACTERIZATION OF COUPLED MICROSTRIP STRUCTURE USING FDTD

Chapter 1 INTRODUCTION

There is currently an increasing interest in accurate modeling and design of interconnects for RF/microwave, high-speed digital, and mixed-signal electronic circuits [1],[2],[3],[4],[5],[6]. With the rapid increase in clock speed as well as denser integration of devices and components in high performance circuits, the interconnect behavior is becoming a dominant factor in the overall circuit performance. Some of the adverse effects associated with interconnects include time delay, loss, and coupling. In digital circuits, for example, electromagnetic coupling between interconnects can lead to considerable crosstalk noise reducing noise margins, as well as timing fluctuations (jitter). These signal integrity and noise effects can impose serious limitations on maximum operating speed and performance of the circuit. Similarly, higher integration densities in microwave circuits at both the off- and on-chip levels and use of different substrate materials, such as silicon lead to a stronger frequency-dependence of the interconnect characteristics including increased coupling.

Therefore, accurate interconnect models should be included in the design process in order to meet the stringent design specifications for high-performance analog or digital circuit. In this thesis a full-wave electromagnetic technique — the finite difference time domain (FDTD) technique — is applied and a systematic extraction procedure is developed to accurately determine the characteristics of several important coupled interconnect structures used in RF/microwave and

high-speed digital circuits.

1.1 BACKGROUND

In general, interconnects in high-frequency and high-speed electronic circuits must be considered as a distributed coupled system. Coupled interconnects at the off-chip level are typically modeled in terms of a set of multi-conductor coupled transmission lines, and discontinuities such as bends and changes in width are represented by lumped element equivalent circuits. The transmission line parameters and lumped element values for the discontinuities usually are extracted from quasi-static electromagnetic (EM) simulation. At the on-chip level, the distributed resistance of interconnects is significantly increased due to the small conductor cross-sections. Digital on-chip interconnects have been modeled in terms of distributed RC networks, thus neglecting the transmission line behavior. To extract the R and C parameters including mutual coupling capacitances from circuit layouts, fast quasi-static EM techniques have been developed and are available in commercial VLSI design software tools.

Recent studies by researchers at IBM [7] and others, however, show that with rising clock speed the transmission line effects in digital on-chip interconnects can no longer be neglected. Furthermore, the substrate characteristics can have a strong effect on the interconnect performance. In silicon-based technology, and especially in BiCMOS and CMOS processes, the lossy substrate can lead to a significant increase in interconnect loss, strong dispersive transmission line behavior, and increased noise coupling through the substrate. These effects can be detrimental for both RF/microwave and high-speed digital integrated circuits. To mitigate these substrate effects, shielding structures using, for example, patterned ground planes have been suggested in some BiCMOS RF ICs[8].

To accurately extract the distributed parameters of uniform and non-uniform coupled interconnects in a general multi-layered multilevel lossy substrate envi-

ronment including interconnects over patterned substrate shielding structures, quasi-static EM techniques may not be adequate at higher frequencies, and the full-wave EM characteristics must be considered. For many years, full-wave techniques have been applied by many researchers to analyze and simulate a range of transmission line structures. However, the computational burden has prevented the general use of full-wave solvers on desktop computers. With the rapid increase in processor speed and memory size of general desktop computers over the last few years, full-wave electromagnetic field solvers are now becoming a viable tool for computer-aided design of electronic systems and components, including complicated interconnect structures.

Traditionally, most full-wave techniques in electromagnetics are frequency-domain methods [9]. Frequency-domain EM analysis is advantageous, for example, for narrow-band characterization of a variety of components and circuits, and for determining the modal solutions of guided wave structures. On the other hand, time-domain methods are better suited for broadband characterization of structures such as digital or broadband analog interconnects. Time-domain methods also enable transient analysis to be directly performed, which is important for signal integrity and crosstalk noise analysis in digital and mixed-signal systems.

In this thesis, a new CAD-oriented methodology is developed for broadband characterization of several important coupled interconnect structures, including substrate shielding structures, which are used in RF/microwave and high-speed digital circuits. The new characterization methodology is based on the well-known EM full-wave time-domain technique, the *finite difference time domain* (FDTD) method, combined with a systematic extraction procedure using a normal mode approach and multiport network concepts. Since 1966 when Yee [10] first introduced FDTD in electromagnetics for solving scattering problems, FDTD has been applied by many researchers to solve scattering problems and to analyze

various transmission line, antenna and other structures. During this period also a number of significant improvements on the technique have been made.

A number of researchers have applied FDTD to characterize microstrip structures. In 1986, Choi and Hoefler [11] developed a novel procedure which increases the numerical efficiency of the time-domain approach for the application of the FDTD method to the solution of three-dimensional eigenvalue problems. Zhang and his co-workers have calculated the dispersive characteristics of microstrip lines [12], and Shibata and Kimura [1] also reported calculation of the frequency characteristics for microstrip circuits and established a frequency-domain MMIC design method based on time-domain electromagnetic field analysis. The formulation and application of the FDTD method for numerical modeling of electromagnetic wave interactions with arbitrary structures and for electromagnetic wave scattering and radar cross section have been introduced by Taflovie [13], [14].

In 1989, Liang and Mei presented a full-wave analysis of a co-planar waveguide (CPW) and a slotline structure using FDTD [15]. A Metal - Insulator - Semiconductor (MIS) co-planar structure was analyzed with FDTD by Shibata and Sano [16]. In this work, the authors were concerned with on-chip co-planar lines in high-speed silicon ICs. They presented a rigorous full-wave analysis which includes the semiconducting substrate effect and the loss in metal lines. Wu and Chang [17] investigated the shielding effects on the frequency-dependent effective dielectric constant of a waveguide-shielded microstrip structure. In 1992, Wolff reported the application of FDTD to a realistic microwave circuit design and nonlinear microwave integrated circuit design [2]. The extraction of equivalent circuits for transmission lines was presented by Mittra [3].

In the area of discontinuity problems, Zhang and Mei determined the scattering parameters for single symmetric microstrip discontinuities such as open end, cross-junction, T-junction, step-in-width, and microstrip gap using FDTD [18]. Sheen calculated the frequency-dependent scattering parameters for several

printed microstrip circuits such as a line-fed rectangular patch antenna, low-pass filter, and a rectangular branch line coupler [19], [20]. Moore [21] reported the scattering parameters for a single microstrip right-angle bend, and Feix [22] characterized single mitered and unmitered bend structures in 1990 and 1992, respectively.

FDTD has also been applied to analyze and characterize various other structures including microstrip patch antennas (e.g. [23], [24], [25], [26]) and packaging structures [27], [28]. To improve modeling of radiative systems, the FDTD method has been combined with near-to-near and near-to-far field transformation techniques [29], [30], [31], [32].

1.2 ORGANIZATION OF THE DISSERTATION

This thesis describes a new CAD-oriented methodology for broadband characterization of coupled off- and on-chip interconnects for high-frequency and high-speed circuits. The methodology is applied to several representative coupled microstrip structures including discontinuities and substrate shielding. The approach is validated by comparison with other full-wave techniques.

Chapter 2 gives an overview of the FDTD technique and reviews the numerical stability issues, the Perfectly Matched Layer (PML) absorbing boundary condition, as well as implementation issues for FDTD to accurately model single and coupled microstrip structures. Using the example of a single microstrip, the model for line excitation and the procedure for extracting the frequency-dependent characteristics from the time-domain electromagnetic fields are described.

In chapter 3 it is shown how multiple coupled line structures, including asymmetric coupled three-line structures, can be analyzed using the FDTD method combined with the normal mode approach. The frequency-dependent results for representative coupled two- and three-line structures are shown and compared

with other full-wave solutions.

In Chapter 4 the FDTD method is applied to single and symmetric coupled microstrip structures on lossy silicon substrate. The broadband behavior of the distributed line parameters is extracted from the time-domain EM fields and compared with other methods. A cross-bar shielding structure for reducing substrate loss and improving the quality factor is also considered. The characteristics of shielded microstrip lines are studied for different shielding dimensions.

Chapter 5 covers various types of discontinuities in single and coupled microstrip lines. Various two and four port microstrip circuit elements such as single step-in-width, asymmetric single gap, open-end, cross-junction, asymmetric coupled gaps and coupled step-in-width are analyzed.

Chapter 6 summarizes the results obtained in this thesis and gives suggestions for possible future work.

Chapter 2

THE FINITE DIFFERENCE TIME DOMAIN METHOD

2.1 INTRODUCTION

The development of the Finite Difference Time Domain (FDTD) method in electromagnetics was first presented in a paper by Kane S. Yee in the mid-60's [10]. At that time, the method was handicapped due to the lack of computer resources. However, present generation computer systems with large memory capacities and fast processor speeds enable the use of FDTD for electromagnetic (EM) analysis and simulation of complicated structures. In FDTD the propagation of an electromagnetic wave into a volume space containing dielectric and conducting materials is being modeled. Since its first introduction by Yee the FDTD method has been adapted, modified, and expanded to suit many electromagnetic applications. For example, in 1980 Taflové applied FDTD for predicting the sinusoidal electromagnetic fields penetrating an arbitrary dielectric or conducting body [33, 34]. Choi has proposed the application of the FDTD method to the solution of three-dimensional eigenvalue problems [11].

Fang et al. [12], [18] were among the first to investigate the dispersive characteristics of microstrips using FDTD. There has been a lot of interest in applying the FDTD method to microstrip, coplanar waveguide, slotline, and other strip line circuits such as filters and couplers. FDTD has also been used to analyze transmission lines in multichip modules (MCM), as well as microstrip patch antennas [1]-[16].

In order to model open-region problems, an absorbing boundary condition (ABC) is usually used to truncate the computational domain. Early techniques

have included differential-based ABCs proposed by Engquist and Madja [35] and Mur [36]. In the mid-1980s, these ABC techniques were improved by formulations proposed by Higdon [37],[38]. More recently, Berenger [39],[40] proposed a new absorbing boundary condition known as Perfectly Matched Layer (PML) with significantly improved performance. The PML boundary conditions are used in all FDTD simulations in this thesis.

This chapter first reviews the formulation of the FDTD technique including the PML absorbing boundary condition, briefly discusses implementation issues, and ends with a simple application example of a transmission line problem.

2.2 FDTD TECHNIQUE

The Finite-Difference Time-Domain method is a direct implementation of the Maxwell's equations in differential form by use of a finite-difference approximation. With this method the central difference approximations are applied to both space and time derivatives. In a source-free region of space consisting of electrical parameters that are independent of time Maxwell's time-dependent curl equations are given by

$$\frac{\partial \vec{H}}{\partial t} = -\frac{1}{\mu} \nabla \times \vec{E} \quad (2.1)$$

$$\frac{\partial \vec{E}}{\partial t} = \frac{1}{\epsilon} (\nabla \times \vec{H} - \sigma \vec{E}) \quad (2.2)$$

where \vec{E} is the electric field in volts/meter, \vec{H} is the magnetic field in amperes/meter, ϵ is the electrical permittivity in farads/meter, μ is the magnetic

permeability in henrys/meter, and σ is the electrical conductivity in mhos/meter of the medium.

In a Cartesian coordinate system, equations (2.1) and (2.2) can be written as a set of first-order partial differential equations as

$$\frac{\partial \vec{H}_x}{\partial t} = \frac{1}{\mu} \left(\frac{\partial \vec{E}_y}{\partial z} - \frac{\partial \vec{E}_z}{\partial y} \right) \quad (2.3)$$

$$\frac{\partial \vec{H}_y}{\partial t} = \frac{1}{\mu} \left(\frac{\partial \vec{E}_z}{\partial x} - \frac{\partial \vec{E}_x}{\partial z} \right) \quad (2.4)$$

$$\frac{\partial \vec{H}_z}{\partial t} = \frac{1}{\mu} \left(\frac{\partial \vec{E}_x}{\partial y} - \frac{\partial \vec{E}_y}{\partial x} \right) \quad (2.5)$$

$$\frac{\partial \vec{E}_x}{\partial t} = \frac{1}{\epsilon} \left(\frac{\partial \vec{H}_z}{\partial y} - \frac{\partial \vec{H}_y}{\partial z} - \sigma \vec{E}_x \right) \quad (2.6)$$

$$\frac{\partial \vec{E}_y}{\partial t} = \frac{1}{\epsilon} \left(\frac{\partial \vec{H}_x}{\partial z} - \frac{\partial \vec{H}_z}{\partial x} - \sigma \vec{E}_y \right) \quad (2.7)$$

$$\frac{\partial \vec{E}_z}{\partial t} = \frac{1}{\epsilon} \left(\frac{\partial \vec{H}_y}{\partial x} - \frac{\partial \vec{H}_x}{\partial y} - \sigma \vec{E}_z \right) \quad (2.8)$$

Equations (2.3) – (2.8) are a system of six coupled partial differential equations which form the basis of the FDTD algorithm. In order to find approximate EM solutions, the problem is discretized. Following Yee's notation [10], a grid point in the computational space is denoted as

$$(i, j, k) = (i\Delta x, j\Delta y, k\Delta z) \quad (2.9)$$

and a function of the three spatial coordinates and time is expressed as

$$F^n(i, j, k) = F(i\Delta x, j\Delta y, k\Delta z, n\Delta t) \quad (2.10)$$

where Δx , Δy and Δz are the lattice space increments in the x-, y- and z-directions, respectively. In (2.10), Δt is the time increment, (i, j, k) are integers denoting the location inside the FDTD lattice, and n is an integer denoting the time stepping index.

In Yee's method, centered difference approximations are used for the first-order space and time partial derivatives, i.e.,

$$\frac{\partial F^n(i, j, k)}{\partial x} = \frac{F^n(i + 1/2, j, k) - F^n(i - 1/2, j, k)}{\Delta x} + O([\Delta x]^2) \quad (2.11)$$

$$\frac{\partial F^n(i, j, k)}{\partial t} = \frac{F^{n+1/2}(i, j, k) - F^{n-1/2}(i, j, k)}{\Delta t} + O([\Delta t]^2) \quad (2.12)$$

The centered difference approximations have second-order accuracy in space and time. In order to achieve the accuracy of 2.11 and to implement all space derivatives in (2.3) – (2.8), Yee positioned the components of \vec{E} and \vec{H} about a unit cell of the lattice as shown in Figure 2.1. The \vec{E} and \vec{H} fields are computed at alternate half time steps in order to achieve centered differences for the time derivatives.

The resulting system of finite-difference equations is given by

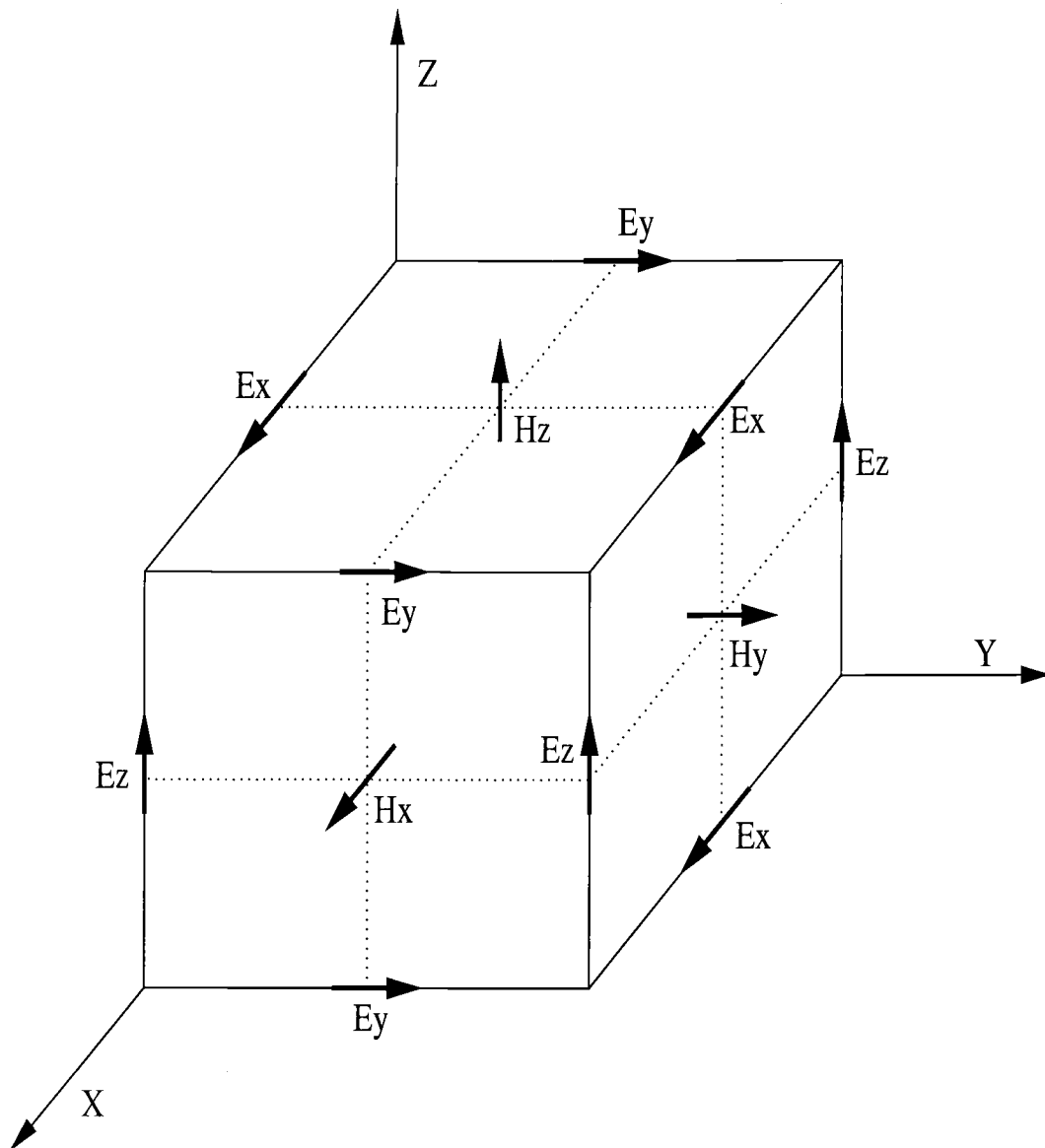


Figure 2.1. Yee's unit cell

$$\begin{aligned}
H_x^{n+\frac{1}{2}}(i, j + \frac{1}{2}, k + \frac{1}{2}) &= \left(\frac{2\mu - \sigma_m \Delta t}{2\mu + \sigma_m \Delta t} \right) H_x^{n-\frac{1}{2}}(i, j + \frac{1}{2}, k + \frac{1}{2}) + \left(\frac{2\Delta t}{2\mu + \sigma_m \Delta t} \right) \\
&\cdot \left\{ \frac{1}{\Delta y} \left[E_z^n(i, j + 1, k + \frac{1}{2}) - E_z^n(i, j, k + \frac{1}{2}) \right] \right. \\
&\left. + \frac{1}{\Delta z} \left[E_y^n(i, j + \frac{1}{2}, k + 1) - E_y^n(i, j + \frac{1}{2}, k) \right] \right\} \quad (2.13)
\end{aligned}$$

$$\begin{aligned}
H_y^{n+\frac{1}{2}}(i + \frac{1}{2}, j, k + \frac{1}{2}) &= \left(\frac{2\mu - \sigma_m \Delta t}{2\mu + \sigma_m \Delta t} \right) H_y^{n-\frac{1}{2}}(i + \frac{1}{2}, j, k + \frac{1}{2}) + \left(\frac{2\Delta t}{2\mu + \sigma_m \Delta t} \right) \\
&\cdot \left\{ \frac{1}{\Delta z} \left[E_x^n(i + \frac{1}{2}, j, k + 1) - E_x^n(i + \frac{1}{2}, j, k) \right] \right. \\
&\left. + \frac{1}{\Delta x} \left[E_z^n(i + 1, j, k + \frac{1}{2}) - E_z^n(i, j, k + \frac{1}{2}) \right] \right\} \quad (2.14)
\end{aligned}$$

$$\begin{aligned}
H_z^{n+\frac{1}{2}}(i + \frac{1}{2}, j + \frac{1}{2}, k) &= \left(\frac{2\mu - \sigma_m \Delta t}{2\mu + \sigma_m \Delta t} \right) H_z^{n-\frac{1}{2}}(i + \frac{1}{2}, j + \frac{1}{2}, k) + \left(\frac{2\Delta t}{2\mu + \sigma_m \Delta t} \right) \\
&\cdot \left\{ \frac{1}{\Delta x} \left[E_y^n(i + 1, j + \frac{1}{2}, k) - E_y^n(i, j + \frac{1}{2}, k) \right] \right. \\
&\left. + \frac{1}{\Delta y} \left[E_x^n(i + \frac{1}{2}, j + 1, k) - E_x^n(i + \frac{1}{2}, j, k) \right] \right\} \quad (2.15)
\end{aligned}$$

$$\begin{aligned}
E_x^{n+1}(i + \frac{1}{2}, j, k) &= \left(\frac{2\epsilon - \sigma_e \Delta t}{2\epsilon + \sigma_e \Delta t} \right) E_x^n(i + \frac{1}{2}, j, k) + \left(\frac{2\Delta t}{2\epsilon + \sigma_e \Delta t} \right) \\
&\cdot \left\{ \frac{1}{\Delta y} \left[H_z^{n+\frac{1}{2}}(i + \frac{1}{2}, j + \frac{1}{2}, k) - H_z^{n+\frac{1}{2}}(i + \frac{1}{2}, j - \frac{1}{2}, k) \right] \right. \\
&\left. + \frac{1}{\Delta z} \left[H_y^{n+\frac{1}{2}}(i + \frac{1}{2}, j, k + \frac{1}{2}) - H_y^{n+\frac{1}{2}}(i + \frac{1}{2}, j, k - \frac{1}{2}) \right] \right\} \quad (2.16)
\end{aligned}$$

$$E_y^{n+1}(i, j + \frac{1}{2}, k) = \left(\frac{2\epsilon - \sigma_e \Delta t}{2\epsilon + \sigma_e \Delta t} \right) E_y^n(i, j + \frac{1}{2}, k) + \left(\frac{2\Delta t}{2\epsilon + \sigma_e \Delta t} \right)$$

$$\cdot \left\{ \frac{1}{\Delta z} \left[H_x^{n+\frac{1}{2}}(i, j + \frac{1}{2}, k + \frac{1}{2}) - H_x^{n+\frac{1}{2}}(i + \frac{1}{2}, j, k - \frac{1}{2}) \right] \right. \\ \left. + \frac{1}{\Delta x} \left[H_z^{n+\frac{1}{2}}(i + \frac{1}{2}, j + \frac{1}{2}, k) - H_z^{n+\frac{1}{2}}(i - \frac{1}{2}, j + \frac{1}{2}, k) \right] \right\} \quad (2.17)$$

$$E_z^{n+1}(i, j, k + \frac{1}{2}) = \left(\frac{2\epsilon - \sigma_e \Delta t}{2\epsilon + \sigma_e \Delta t} \right) E_z^n(i, j, k + \frac{1}{2}) + \left(\frac{2\Delta t}{2\epsilon + \sigma_e \Delta t} \right) \\ \cdot \left\{ \frac{1}{\Delta x} \left[H_y^{n+\frac{1}{2}}(i + \frac{1}{2}, j, k + \frac{1}{2}) - H_y^{n+\frac{1}{2}}(i - \frac{1}{2}, j, k + \frac{1}{2}) \right] \right. \\ \left. + \frac{1}{\Delta y} \left[H_x^{n+\frac{1}{2}}(i, j + \frac{1}{2}, k + \frac{1}{2}) - H_x^{n+\frac{1}{2}}(i, j - \frac{1}{2}, k + \frac{1}{2}) \right] \right\} \quad (2.18)$$

2.3 NUMERICAL STABILITY

The accuracy of the computed field quantities as well as the stability of time stepping algorithm in FDTD are directly related to the spatial step size Δ and time increment Δt . The finite difference equations (2.13) – (2.18) are not stable if the time step is too large. The step sizes for Δx , Δy , Δz and Δt should be chosen such that the velocity of the numerical signals in the FDTD lattice is not less than the velocity of light in the medium being modeled. The stability condition which needs to be satisfied is given by

$$\Delta t \leq \frac{1}{C_{max}} \left[\frac{1}{(\Delta x)^2} + \frac{1}{(\Delta y)^2} + \frac{1}{(\Delta z)^2} \right]^{-\frac{1}{2}} \quad (2.19)$$

where C_{max} is the maximum phase velocity expected within the problem space. To ensure the accuracy of the computed spatial derivatives of the electromagnetic

fields, $\Delta(x, y, z)$ must be small compared to the smallest wavelength. Following Taflove et al., the width of the Gaussian source pulse is chosen for at least 20 grid spacings per wavelength at the highest frequency component in order to minimize the effects of numerical dispersion and truncation errors due to gridding. To accomplish this, the grid spacings should satisfy

$$\Delta \leq \frac{\lambda}{20} \quad (2.20)$$

2.4 PERFECTLY MATCHED LAYER (PML) ABSORBING BOUNDARY CONDITION

Due to limited computational and memory resources, the computational domain must be truncated for open boundary problems such as a microstrip. The ideal boundary conditions, called perfect absorbing boundary conditions, introduce no reflections for any outgoing wave incident on the boundaries of the computational domain. However, practical absorbing boundary conditions can only partially absorb outgoing waves and cause more or less reflections.

The first simulation space truncation technique comprised of implementing Dirichlet and Neumann boundary conditions. This technique resulted in the total reflection of the incident wave from the edge of the simulation space. The Dirichlet and Neumann boundaries were implemented by setting the appropriate tangential fields to zero at the edges of the simulation space. The first absorbing boundary condition (ABC) is often referred to as the Mur ABC [36]. Berenger's perfectly matched layer(PML) absorbing boundary condition provides orders of magnitude improvement in performance over all previously reported ABCs for the FDTD method [39], [40]. The PML boundary condition relies on introducing

a fictitious magnetic loss and on decomposing Maxwell's equations into twelve equations instead of the typical six equations for three dimensional problems. This increases the complexity and requires additional memory usage around the edges of the simulation space. However, the PML does not make a plane wave assumption, and therefore can be placed closer to the simulation structure. In many cases this results in a smaller computational domain and, hence, significantly reduced memory requirements.

The fictitious magnetic loss, denoted as σ^* , provides two functions: impedance matching between cells and additional attenuation of outgoing waves. The equivalent magnetic conductivity is introduced into Maxwell's equations as follows.

$$\nabla \times \vec{E} = -\sigma^* \vec{H} - \mu \frac{\partial \vec{H}}{\partial t} \quad (2.21)$$

$$\nabla \times \vec{H} = \sigma \vec{E} + \epsilon \frac{\partial \vec{E}}{\partial t} \quad (2.22)$$

Letting Ψ be any component of a wave in the PML region interfacing with a vacuum region, Berenger has shown that [39]

$$\begin{aligned} \Psi = & \Psi_o \exp(j\omega \left(t - \frac{x \cos \phi + y \sin \phi}{cG} \right)) \exp\left(-\frac{\sigma_x \cos \phi}{\epsilon_o cG} x\right) \\ & \cdot \exp\left(-\frac{\sigma_y \sin \phi}{\epsilon_o cG} y\right) \end{aligned} \quad (2.23)$$

$$Z = \frac{\sqrt{\frac{\mu_o}{\epsilon_o}}}{G} \quad (2.24)$$

where Z is the wave impedance, c is the speed of light, ϕ is the angle between the wave field vector and the y -axis, and

$$G = \sqrt{\omega_x \cos^2 \phi + \omega_y \sin^2 \phi} \quad (2.25)$$

$$\omega_x = \frac{1 - \frac{j\sigma_x}{\omega\epsilon_o}}{1 - \frac{j\sigma_x^*}{\omega\mu_o}} \quad (2.26)$$

$$\omega_y = \frac{1 - \frac{j\sigma_y}{\omega\epsilon_o}}{1 - \frac{j\sigma_y^*}{\omega\mu_o}} \quad (2.27)$$

Choosing the electric and magnetic losses so they satisfy

$$\frac{\sigma}{\epsilon_o} = \frac{\sigma^*}{\mu_o} \quad (2.28)$$

results in ω_x , ω_y and G equal to one at all frequencies. In this case, the wave components and the wave impedance are

$$\begin{aligned} \Psi = & \Psi_o \exp\left(j\omega\left(t - \frac{x \cos \phi + y \sin \phi}{c}\right)\right) \exp\left(-\frac{\sigma_x \cos \phi}{\epsilon_o c} x\right) \\ & \cdot \exp\left(-\frac{\sigma_y \sin \phi}{\epsilon_o c} y\right) \end{aligned} \quad (2.29)$$

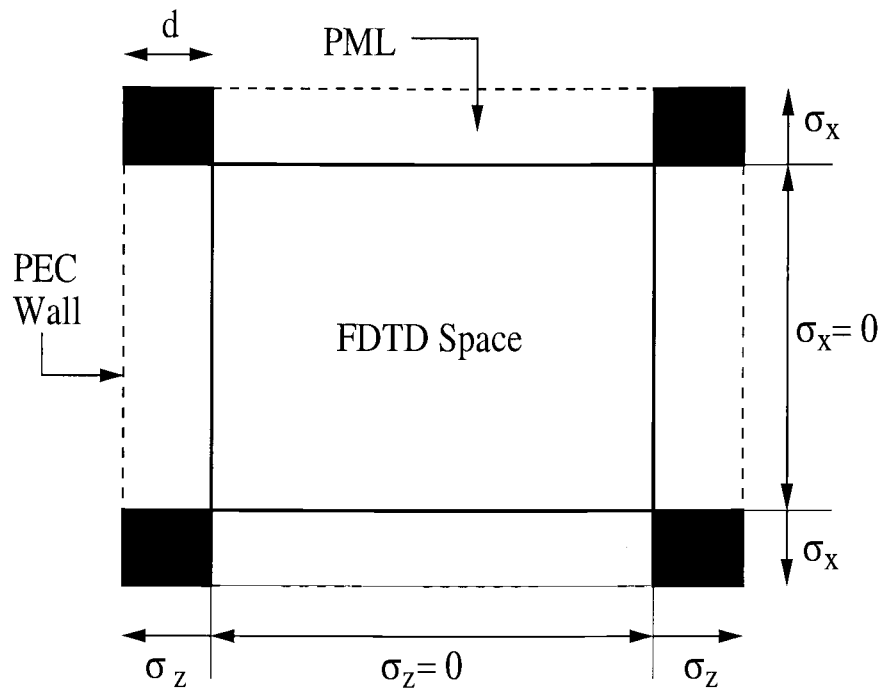


Figure 2.2. Perfect Electric Wall

and

$$Z = \sqrt{\frac{\mu_0}{\epsilon_0}} \quad (2.30)$$

The derivation presented above shows that in the PML media the wave propagates at the speed of light and is attenuated exponentially along the x and y axes, and that the wave impedance matches the impedance of the vacuum independent of frequency and angle of incidence. Ideally the attenuation could be made extremely high by choosing large σ and σ^* in the ABC regions. This

would require a PML layer of only one cell thickness. However the large attenuation would cause large numerical dispersion in the FDTD technique resulting in a reflection. To compensate for the reflections due to numerical dispersion, Berenger proposed that the loss should increase gradually with depth through several layers of PML media as follows

$$\sigma(\rho) = \sigma_{max} \left(\frac{\rho}{\delta}\right)^n \quad (2.31)$$

Where, ρ is the depth into the PML region, δ is the total PML thickness, and n is the growth factor. Deriving a theoretical reflection coefficient, R_{th} , for waves normally incident on the PML boundary the value of σ_{max} can be defined as

$$\sigma_{max} = -\frac{(n+1)\epsilon_0 c}{2\delta} \ln(R_{th}) \quad (2.32)$$

This results in three user defined parameters for the implementation of PML boundary conditions: 1) the number of PML layers, 2) n , the growth factor, 3) R_{th} , the theoretical reflection coefficient. Splitting Maxwell's equations into twelve equations allows the attenuation to be provided on only the outgoing component of the wave, leaving the tangential components of the wave unaffected. The loss components are defined in the twelve equations as follows:

$$\mu_0 \frac{\partial H_{xy}}{\partial t} + \sigma_y^* H_{xy} = -\frac{\partial(E_{zx} + E_{zy})}{\partial y} \quad (2.33)$$

$$\mu_0 \frac{\partial H_{xz}}{\partial t} + \sigma_z^* H_{xz} = \frac{\partial(E_{yx} + E_{yz})}{\partial z} \quad (2.34)$$

$$\mu_0 \frac{\partial H_{yz}}{\partial t} + \sigma_z^* H_{yz} = -\frac{\partial(E_{xy} + E_{xz})}{\partial z} \quad (2.35)$$

$$\mu_o \frac{\partial H_{yx}}{\partial t} + \sigma_x^* H_{yx} = \frac{\partial(E_{zx} + E_{zy})}{\partial x} \quad (2.36)$$

$$\mu_o \frac{\partial H_{zx}}{\partial t} + \sigma_x^* H_{zx} = -\frac{\partial(E_{yx} + E_{yz})}{\partial x} \quad (2.37)$$

$$\mu_o \frac{\partial H_{zy}}{\partial t} + \sigma_y^* H_{zy} = -\frac{\partial(E_{xy} + E_{xz})}{\partial y} \quad (2.38)$$

$$\epsilon_o \frac{\partial E_{xy}}{\partial t} + \sigma_y E_{xy} = \frac{\partial(H_{zx} + H_{zy})}{\partial y} \quad (2.39)$$

$$\epsilon_o \frac{\partial E_{xz}}{\partial t} + \sigma_z E_{xz} = -\frac{\partial(H_{yx} + H_{yz})}{\partial z} \quad (2.40)$$

$$\epsilon_o \frac{\partial E_{yz}}{\partial t} + \sigma_z E_{yz} = \frac{\partial(H_{xy} + H_{xz})}{\partial z} \quad (2.41)$$

$$\epsilon_o \frac{\partial E_{yx}}{\partial t} + \sigma_x E_{yx} = -\frac{\partial(H_{zx} + H_{zy})}{\partial x} \quad (2.42)$$

$$\epsilon_o \frac{\partial E_{zx}}{\partial t} + \sigma_x E_{zx} = \frac{\partial(H_{yx} + H_{yz})}{\partial x} \quad (2.43)$$

$$\epsilon_o \frac{\partial E_{zy}}{\partial t} + \sigma_y E_{zy} = -\frac{\partial(H_{xy} + H_{xz})}{\partial y} \quad (2.44)$$

There are currently several papers on implementing the PML using approaches that differ from the twelve component equations, however, the implementation here uses the original twelve equation approach proposed by Berenger.

2.5 IMPLEMENTATION OF THE FDTD

In this section, the specific implementation of the FDTD method including PML boundary conditions, for the analysis of planar microstrip circuits is described. The time stepping equations in Equations (2.3) – (2.8) can be used in the manner prescribed in Figure 2.1 to track the time evolution of the electromagnetic fields within the computational domain for a given set of initial and boundary conditions. The flow chart for the FDTD algorithm is shown in Fig. 2.3.

Initially, all field values within the computational domain are set to zero. An excitation is then introduced by specifying the electric field at the near end point of conductor strips. The value of \vec{H} is then computed at time $t = (n + \frac{1}{2})\Delta t$, followed by the computation of \vec{E} at time $t = (n + 1)\Delta t$. Boundary conditions on the perfect electric conductors are enforced by setting the tangential components of \vec{E} to zero at mesh points coincident with the conductors. Because of this, it is essential that conduction surfaces coincide with the unit cell faces. This time-stepping procedure is repeated until the desired number of time steps is reached.

To minimize the memory and computational burden, a preprocessing step is performed before the FDTD simulation begins [41]. The standard FDTD equation can be rewritten from its standard form

$$\begin{aligned}
 E_z^{n+1}(i, j, k + \frac{1}{2}) &= \left(\frac{2\epsilon - \sigma_e \Delta t}{2\epsilon + \sigma_e \Delta t} \right) E_z^n(i, j, k + \frac{1}{2}) + \left(\frac{2\Delta t}{2\epsilon + \sigma_e \Delta t} \right) \\
 &\quad \left\{ \frac{1}{\Delta x} \left[H_y^{n+\frac{1}{2}}(i + \frac{1}{2}, j, k + \frac{1}{2}) - H_y^{n+\frac{1}{2}}(i - \frac{1}{2}, j, k + \frac{1}{2}) \right] \right. \\
 &\quad \left. + \frac{1}{\Delta y} \left[H_x^{n+\frac{1}{2}}(i, j + \frac{1}{2}, k + \frac{1}{2}) - H_x^{n+\frac{1}{2}}(i, j - \frac{1}{2}, k + \frac{1}{2}) \right] \right\}
 \end{aligned} \tag{2.45}$$

into the less computationally intensive form of

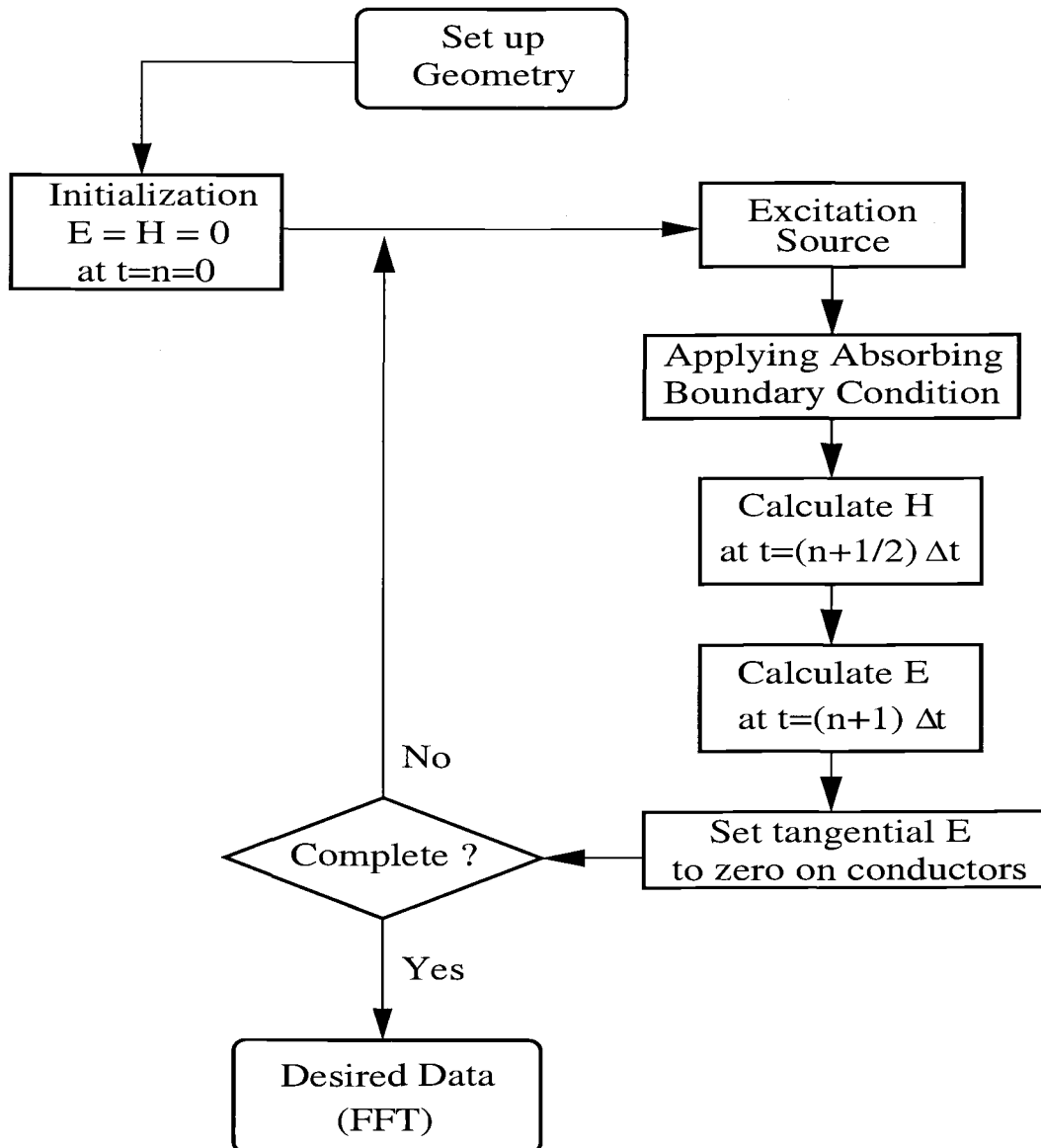


Figure 2.3. Implementation of the FDTD

$$\begin{aligned}
E_z^{n+1}(i, j, k + \frac{1}{2}) &= C_A E_z^n(i, j, k + \frac{1}{2}) + C_B \left\{ C_1 H_y^{n+\frac{1}{2}}(i + \frac{1}{2}, j, k + \frac{1}{2}) \right. \\
&\quad + C_2 H_y^{n+\frac{1}{2}}(i - \frac{1}{2}, j, k + \frac{1}{2}) + C_3 H_x^{n+\frac{1}{2}}(i, j + \frac{1}{2}, k + \frac{1}{2}) \\
&\quad \left. + C_4 H_x^{n+\frac{1}{2}}(i, j - \frac{1}{2}, k + \frac{1}{2}) \right\} \quad (2.46)
\end{aligned}$$

In equation (2.46), C_A , C_B , C_1 , C_2 , C_3 , and C_4 are all constant during the simulation. The actual values of the constants are not stored in each cell with the field information, but a short integer which is used as an index to locate the proper constant value is stored in each cell. This results in a large computer memory savings by storing only a type short integer in each cell instead of two type doubles such as C_A and C_B . Additionally many of the cells will have the same C_A and C_B pair, so the redundant information is eliminated, and only the unique constant pairs are stored as double precision numbers.

The spatial constants (C_1 , C_2 , C_3 , and C_4) are looked up by using the grid indexes (i, j, k) , and since the grid is orthogonal, the information is stored in three one dimensional arrays representing each the X , Y , and Z axes, The spatial constants are preprocessed to determine the value of each constant and which neighboring cells will need to be accessed for the calculation of the spatial derivatives. This results in both a memory savings and a reduction in computational burden.

After both the material constants and spatial constants have been calculated, there are no divisions performed inside of the main FDTD loops for typical cells. Some special case cells may perform divisions, but these are few in number compared to the overall number of cells.

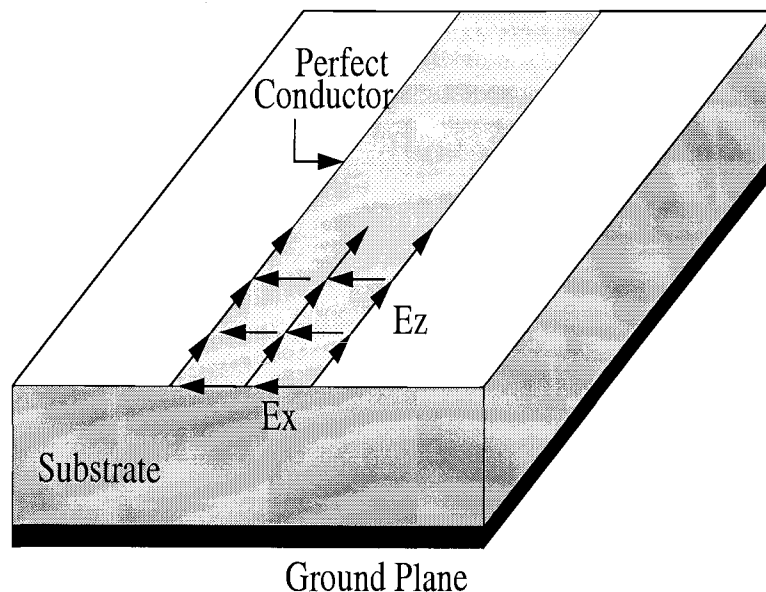


Figure 2.4. Modeling of a perfectly conducting microstrip

2.5.1 MICROSTRIP CONDUCTOR

The interconnect structures considered in this dissertation consist of a conducting ground plane, a multi-layer lossy dielectric substrate, and conducting strips. The emphasis of this work is to include coupling and substrate effects in the interconnect characteristics and to develop a systematic extraction methodology. Therefore, for simplicity, conductor loss is ignored and all conductors are assumed to be perfectly conducting and to have zero thickness. The boundary conditions for a perfect conductor are zero tangential electric fields and zero normal magnetic fields on the conducting surface. This is achieved in the FDTD algorithm by setting the electric fields on the appropriate faces of the unit cell. An example of a perfectly conducting microstrip conductor is shown in Figure 2.4. In this case, the electric fields are set to zero on the top of the unit cells that are at the dielectric air interface and by zeroing the electric fields at the bottom of the lowest unit cells, i. e. the ground plane. The boundary condition on the normal

magnetic field is automatically satisfied by the finite difference calculations if the tangential electric fields have been zeroed.

2.5.2 MATERIAL BOUNDARY CONDITIONS

To allow interfaces between materials with different dielectric constants, conductivities or magnetic properties, the FDTD method requires modification to the basic equations previously presented. However, without proper handling of the material interface conditions the FDTD technique typically becomes unstable. The derivation of the FDTD equations at a general material boundary interface was presented in [41] and is summarized below. Calculating the components of the dielectric constant and conductivity is based on the weighted mean of the material properties in the cells tangential to the electric field component. Figure 2.5 shows the material properties in relation to the vertical E_x component, represented by the black dot.

The effective dielectric and conductivity constants are calculated as follows with the variables defined in Figure 2.5.

$$\epsilon_{\text{reff}} = \frac{\epsilon_{r1}dy1dz2 + \epsilon_{r2}dy1dz1 + \epsilon_{r3}dy2dz2 + \epsilon_{r4}dy2dz1}{(dy1 + dy2) \cdot (dz1 + dz2)} \quad (2.47)$$

$$\sigma_{\text{eff}} = \frac{\sigma_1dy1dz2 + \sigma_2dy1dz1 + \sigma_3dy2dz2 + \sigma_4dy2dz1}{(dy1 + dy2) \cdot (dz1 + dz2)} \quad (2.48)$$

The effective magnetic constants are computed as a weighted harmonic mean of the cell properties normal to the magnetic field component. Figure 2.6 shows

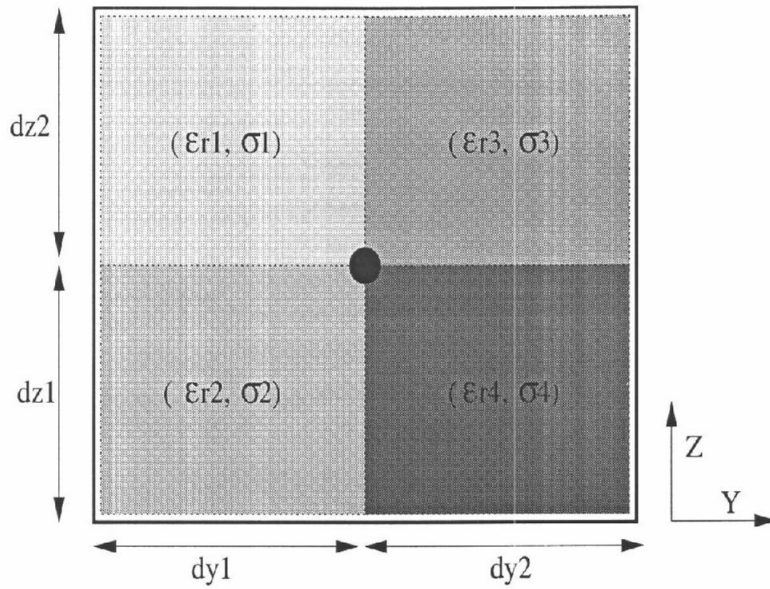


Figure 2.5. Effective dielectric constant

the material properties in relation to the H_x component for the calculation of the effective material constants.

The effective permeability and magnetic conductivity constants are calculated as follows with the variables defined in Figure 2.6.

$$\mu_{eff} = \frac{\mu_1\mu_2(dx1 + dx2)}{\mu_1dx2 + \mu_2dx1} \quad (2.49)$$

$$\sigma_{eff}^* = \frac{\sigma_1^*\sigma_2^*(dx1 + dx2)}{\sigma_1^*dx2 + \sigma_2^*dx1} \quad (2.50)$$

These electric and magnetic material properties are necessary for the correct implementation of the multi-layered lossy substrate environment in FDTD. To reduce the computational and memory demands, the material properties are calculated as a preprocessing step and redundant values are eliminated.

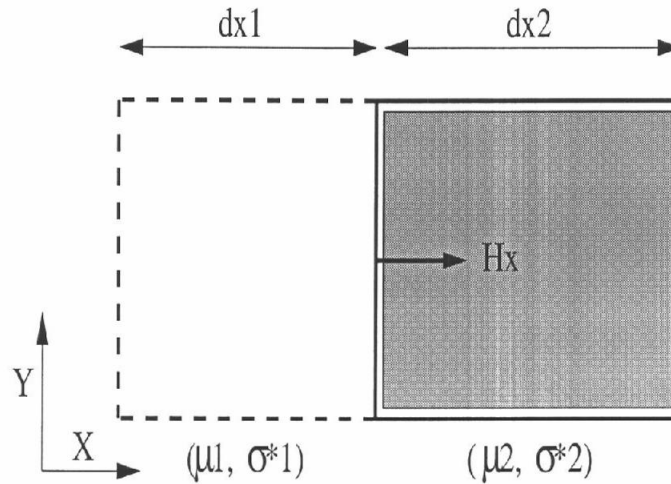


Figure 2.6. Effective conductivity constant

2.5.3 EXCITATION SOURCE

In order to simulate a voltage source excitation, it is necessary to impose the electric field between the conductor and ground plane. This may be accomplished by enforcing the electric field, E_y , on the front wall of the mesh. The remaining electric field components on the source plane must then be specified or calculated. The choice of the time function for the source was described in [19], [20]. The requirements are: (1) The frequency spectrum of the excitation signal must extend over the entire frequency range of interest. (2) The time function must usually be a pulse, i.e., localized in time and space so that the source may be switched off. (3) To minimize the effects of numerical dispersion, the highest frequencies present in the pulse should correspond to approximately 20 points per wavelength. Following Sheen [20], excitation waveforms such as an impulse and pulses of rectangular and triangular shapes meet the first two requirements, but do not satisfy the third requirement. Sinusoidal time functions do not allow the source to be switched off. A choice of time function that meet all three requirements is the Gaussian pulse. It is desirable as excitation waveform because

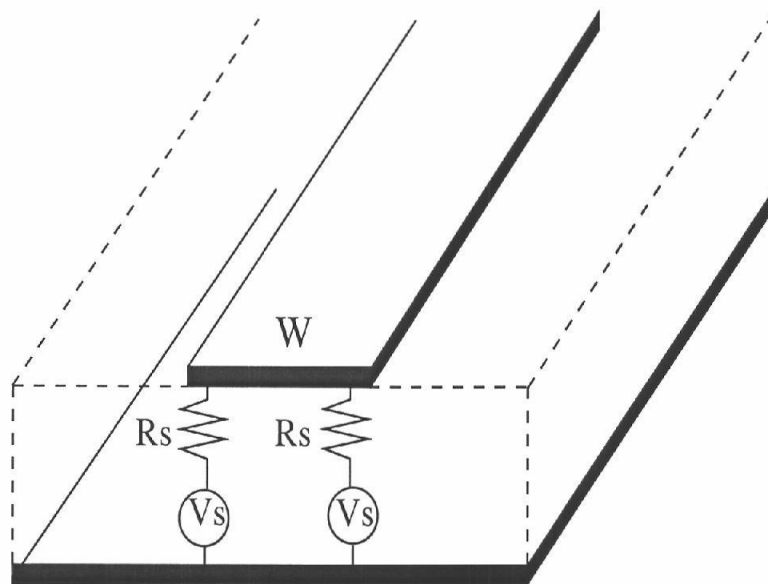


Figure 2.7. Resistive voltage source

its frequency spectrum is also Gaussian and therefore provides frequency domain information from DC to the desired cutoff frequency by adjusting the width of the pulse. A Gaussian pulse is defined by

$$g(t) = \exp\left(\frac{-(t - t_0)^2}{T^2}\right) \quad (2.51)$$

where t_0 and T are time delay and pulse width, respectively. The choice of excitation source depends on the type of problem being simulated, however, the source is generally imposed by forcing specified field components in the computational domain to be known functions of time and/or space. Specifically, the vertical electric field components between the ground plane and a microstrip line are set to be a specified function of time, e.g. Gaussian, to simulate a time-dependent voltage

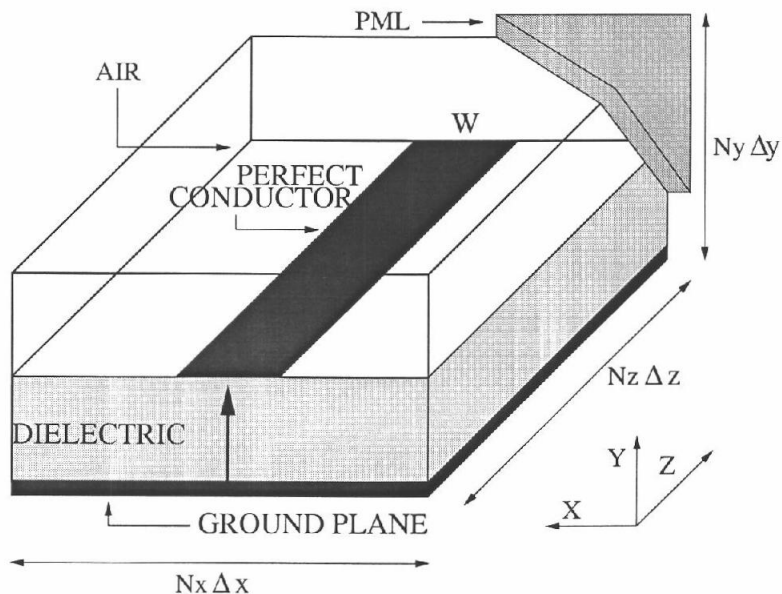


Figure 2.8. Uniform single microstrip line structure including PML absorbing boundary cells.

source, as shown in Figure 2.7. Alternatively, the magnetic fields circulating the microstrip line could be enforced to simulate a current source.

2.6 UNIFORM SINGLE MICROSTRIP LINE AS A SIMPLE EXAMPLE

In this section, a typical uniform single microstrip structure shown in Figure 2.8 is considered, and the basic modeling approach is described. More complicated microstrip structures are considered in the following chapters. The single microstrip is analyzed using the FDTD method to calculate its characteristic impedance, effective dielectric constant and propagation constant, and to extract the distributed inductance and capacitance as a function of frequency.

2.6.1 MODELING OF A SINGLE MICROSTRIP STRUCTURE

The entire computational domain, which includes a single substrate layer and a uniform single microstrip as shown in Figure 2.8, is discretized into a number of cells of size Δx , Δy , and Δz in x , y , and z directions, respectively. The dielectric substrate of the microstrip is assumed to be $\epsilon_r=9.8$, the conductor width is $W = 600 \mu\text{m}$, and the substrate thickness is $H = 635 \mu\text{m}$. The metal strip and ground plane are assumed to be perfectly conducting and infinitely thin. They are defined in the FDTD algorithm by setting the tangential component of the electric field to zero. The conductor line is simulated on an $N_x \Delta x$ by $N_y \Delta y$ by $N_z \Delta z$ computational domain with $\Delta x = 66.67 \mu\text{m}$, $\Delta y = 90.71 \mu\text{m}$ and $\Delta z = 100 \mu\text{m}$. This corresponds to a conductor width of $W = 9\Delta x$ and a substrate height of $H = 7\Delta y$.

The total width N_x and total height N_y of the simulation structure are chosen to be large enough to not disturb the field distribution near the strip. The conductor length N_z is taken to be long enough to avoid the reflection from the far end of the conductor strip during the time of simulation. In all, the entire computational domain including the PML boundary of 6 cells is divided into 65 by 33 by 140 grid cells. The equation for calculating the total number of time steps (N) is given as

$$N = \frac{T_t}{\Delta t} \quad (2.52)$$

with

$$T_t = \frac{d}{V_g} \quad (2.53)$$

and

$$V_g = \frac{c}{\sqrt{\epsilon_r}} \quad (2.54)$$

where T_t is the total time of the signal to reach the far end of the structure and V_g is the velocity of the wave propagating in the z -axis.

A time step of $\Delta t = 0.142$ ps is used to satisfy the numerical stability condition (2.19), and the total number of time steps is 1200. The input is excited with a Gaussian pulse with pulse width $T = 15.15$ ps and time shift $t_o = 45.45$ ps, which corresponds to three times of the pulse width. Figure 2.9 shows the Gaussian input pulse and its frequency spectrum.

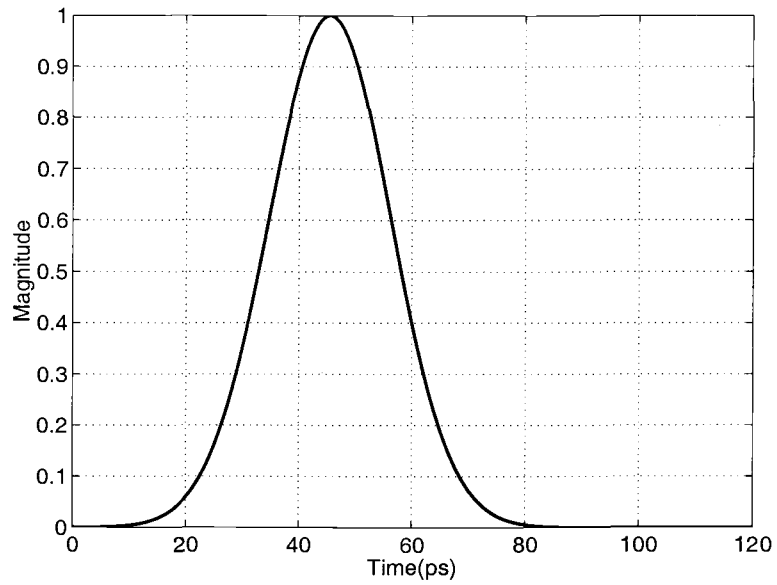
2.6.2 PROPAGATION CHARACTERISTICS

From the computed time-dependent electric and magnetic fields, the voltages and currents on the conductor line are determined. Voltage and current are defined as

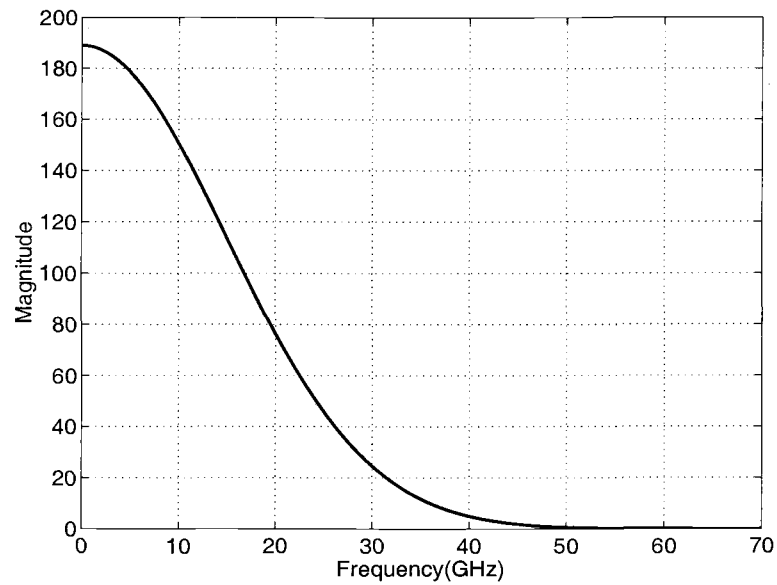
$$I = \oint_C \vec{H} \cdot d\vec{l} \quad (2.55)$$

$$V = - \int_0^d \vec{E} \cdot d\vec{l} \quad (2.56)$$

where C is the transverse contour of the conductor and d is the distance between the conductor and the ground plane, as shown in Figure 2.10. According to the basic FDTD algorithm, currents and voltages are recorded with a difference of one half time step on the conductor line. Figure 2.11(a) shows the integration paths on the grid cells of the conductor strip for voltage and current recorded at different time steps. To represent voltages and currents at the same time step, the currents computed at the half-time step before and after the voltage time step are averaged, as indicated in Figure 2.11(b).



(a)



(b)

Figure 2.9. Gaussian input source and its spectrum for the single microstrip example.

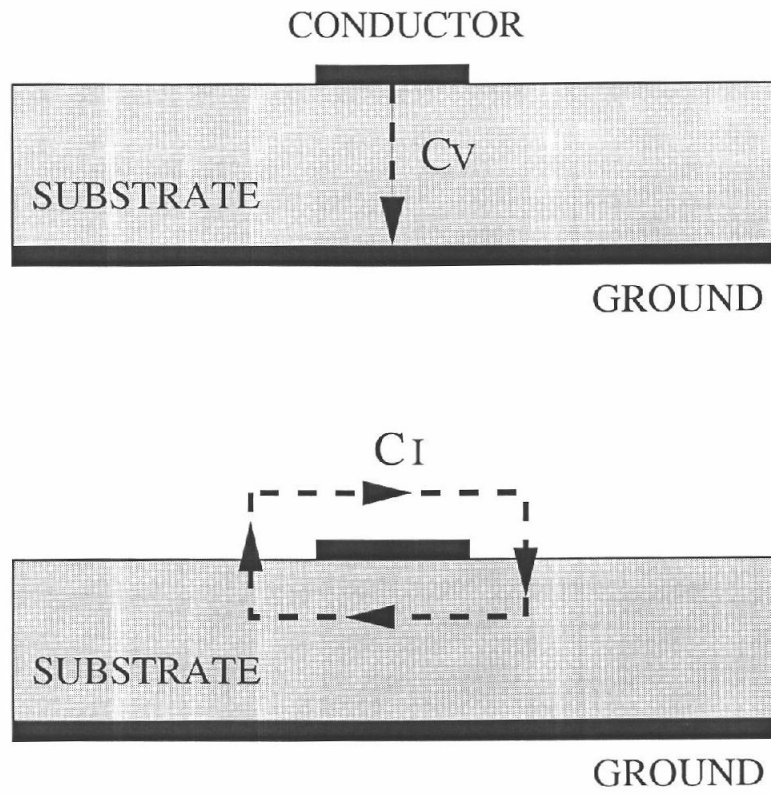


Figure 2.10. Voltage and current contours for a microstrip line.

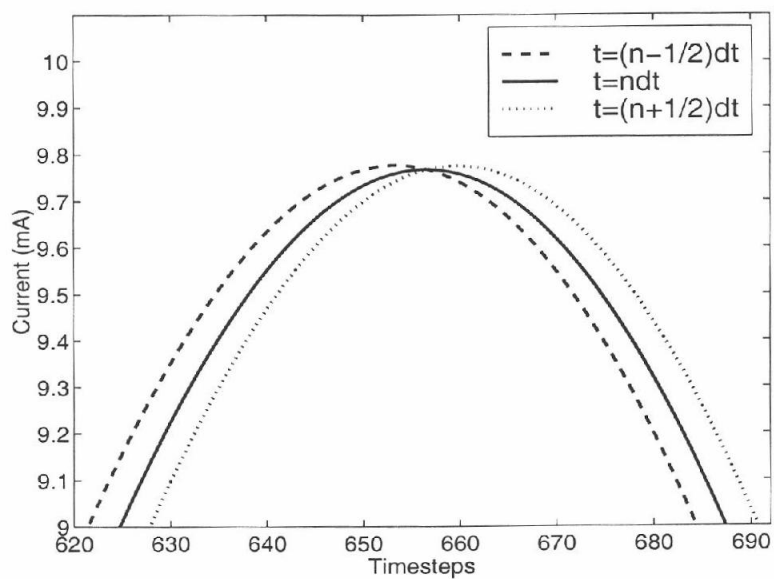
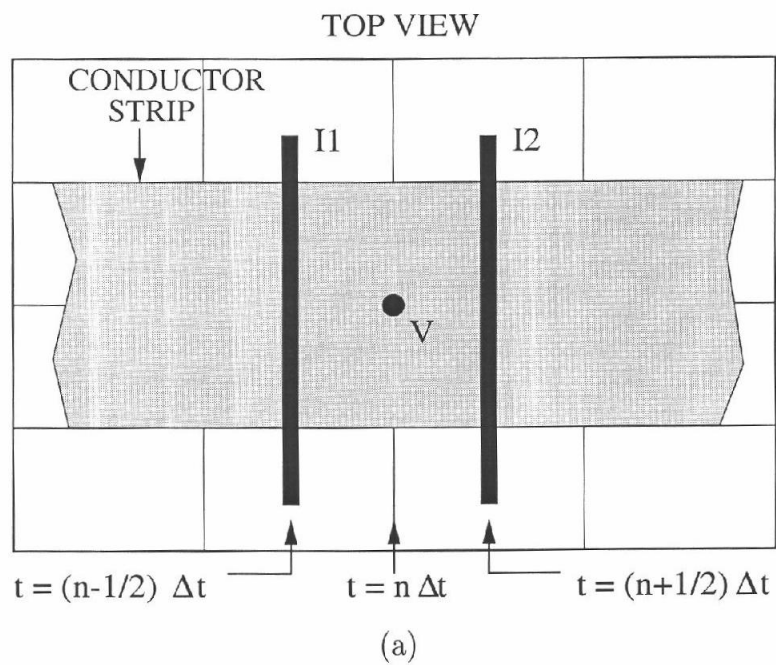


Figure 2.11. (a) Different recording positions for voltage and current and (b) the average of the two currents.

For a Gaussian input pulse at the near end of the structure, the waveform of the input signal propagates along the conductor line, as shown in Figure 2.12. The time variations of the voltage and current waveform at different positions are shown in Figure 2.13. The voltage and current waveforms are recorded at distances $50\Delta z$, $60\Delta z$, $70\Delta z$, $80\Delta z$, and $90\Delta z$ from the input, respectively.

The dispersive property of the microstrip line can be observed from the distortion of the pulse as it propagates along the microstrip line. The dispersion characteristics of a transmission line can be described by the effective dielectric constant $\epsilon_{eff}(\omega)$ as a function of frequency. $\epsilon_{eff}(\omega)$ can be computed from the transient time solutions of voltage or current along the line in the way explained as follows. Assume $V(z, t)$ and $V(z + L, t)$ are monitored voltages taken at z and $z + L$, respectively. They can be any two curves displayed in Figure 2.13. The Fourier transforms of $V(z, t)$ and $V(z + L, t)$ are denoted as $V(z, \omega)$ and $V(z + L, \omega)$ respectively. For a wave propagating in the positive z -direction, $V(z, \omega)$ and $V(z + L, \omega)$ are related by

$$V(z + L, \omega) = V(z, \omega) \exp(-\gamma(\omega)L) \quad (2.57)$$

where

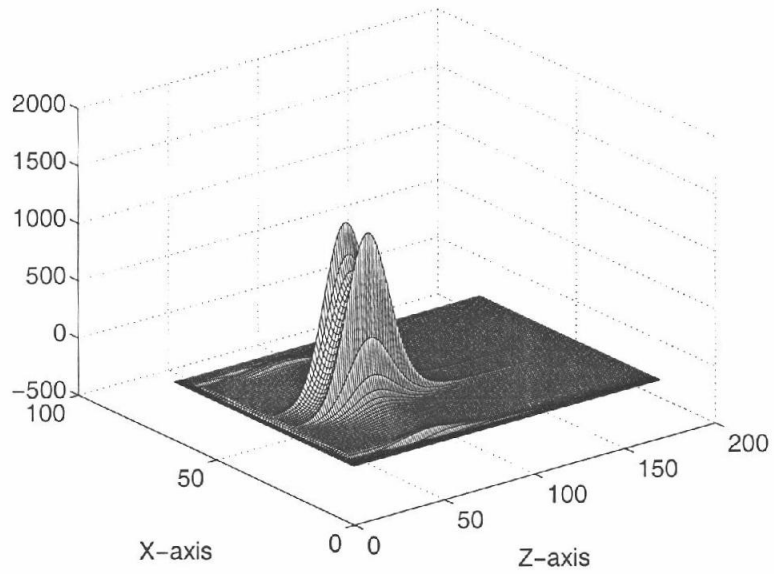
$$\gamma(\omega) = \alpha(\omega) + j\beta(\omega) \quad (2.58)$$

The effective dielectric constant $\epsilon_{eff}(\omega)$ is defined through $\beta(\omega)$ as

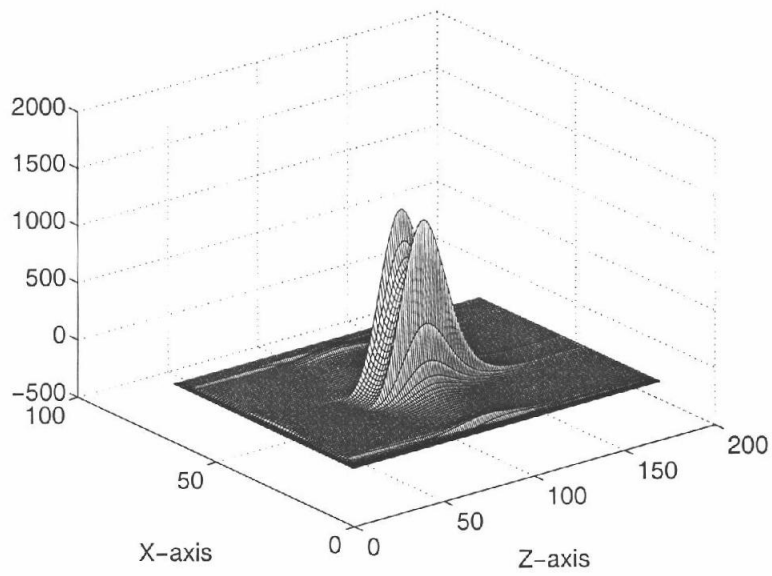
$$\beta(\omega) = \omega \sqrt{\mu\epsilon_0\epsilon_{eff}} \quad (2.59)$$

i.e.,

$$\begin{aligned} \epsilon_{eff} &= \frac{\beta^2}{\omega^2 \mu \epsilon_0} \\ &= \frac{1}{\omega^2 \mu \epsilon_0} \left\{ \frac{1}{L} \text{Im} \left[\ln \left(\frac{V(z, \omega)}{V(z + L, \omega)} \right) \right] \right\}^2 \end{aligned} \quad (2.60)$$

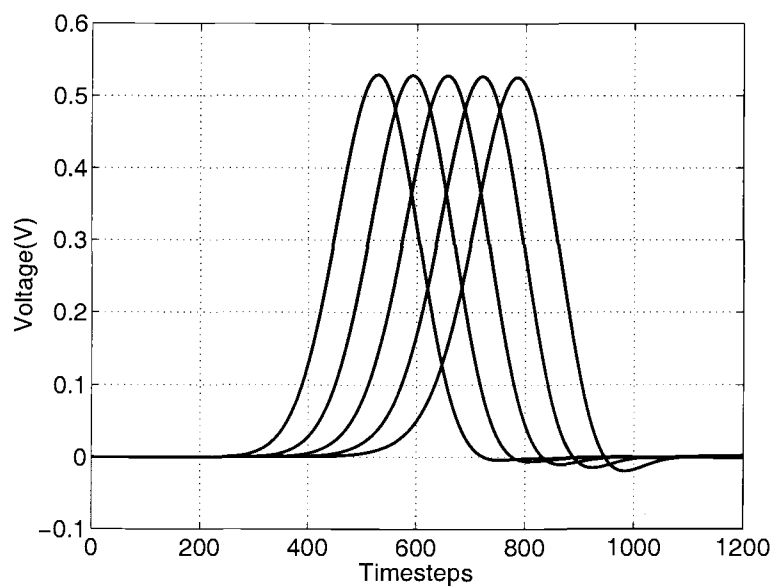


(a)

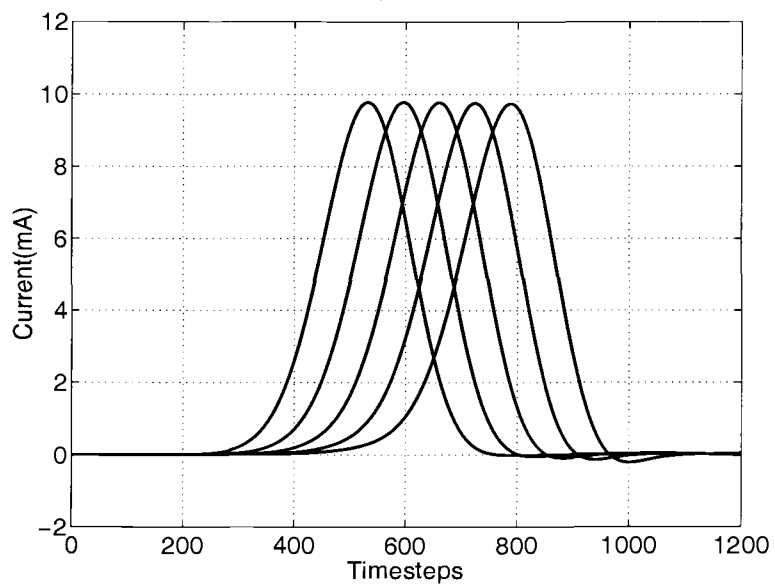


(b)

Figure 2.12. Propagation waveform of single microstrip along the Z-direction at 600 and 800 timesteps, respectively.



(a)



(b)

Figure 2.13. Voltage and current waveforms at different positions: $50\Delta z$, $60\Delta z$, $70\Delta z$, $80\Delta z$, and $90\Delta z$ along the Z-direction.

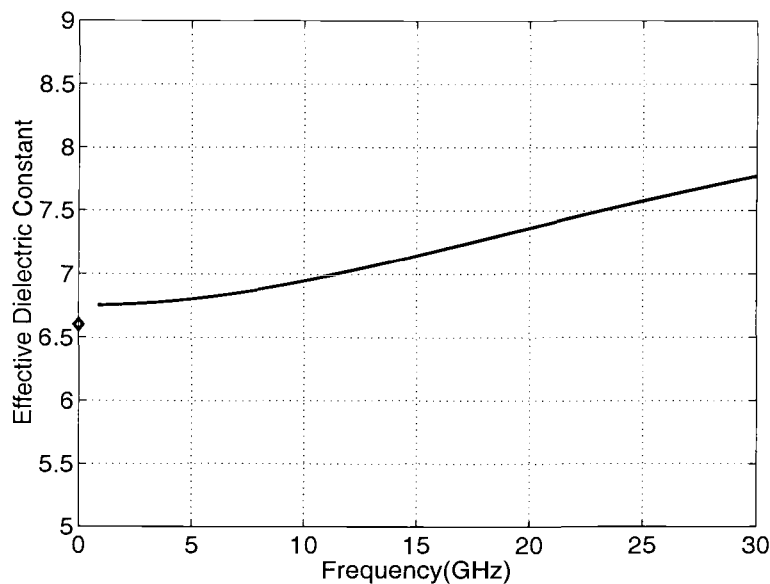


Figure 2.14. Effective dielectric constant as a function of frequency (Solid: FDTD, Diamond: Static value).

The effective dielectric constant $\epsilon_{eff}(\omega)$ of the microstrip line, obtained with the FDTD method is plotted in Figure 2.14. As can be seen from Figure 2.14, the wave propagation velocity varies with frequency.

Another characteristic quantity of the microstrip line is the characteristic impedance $Z_o(\omega)$. The characteristic impedance $Z_o(\omega)$ can be defined as the ratio of $V(\omega)/I(\omega)$. $V(\omega)$ is the Fourier transform of the transient voltage $V(t)$, which is defined as the line integral of the electric field from the ground plane to the conductor strip and $I(\omega)$ is the Fourier transform of the transient current $I(t)$, defined as the loop integral of the magnetic field around the conductor strip, both as illustrated in Figure 2.10. Figure 2.15 shows the characteristic impedance of the microstrip line as obtained by the FDTD method as well as the static value.

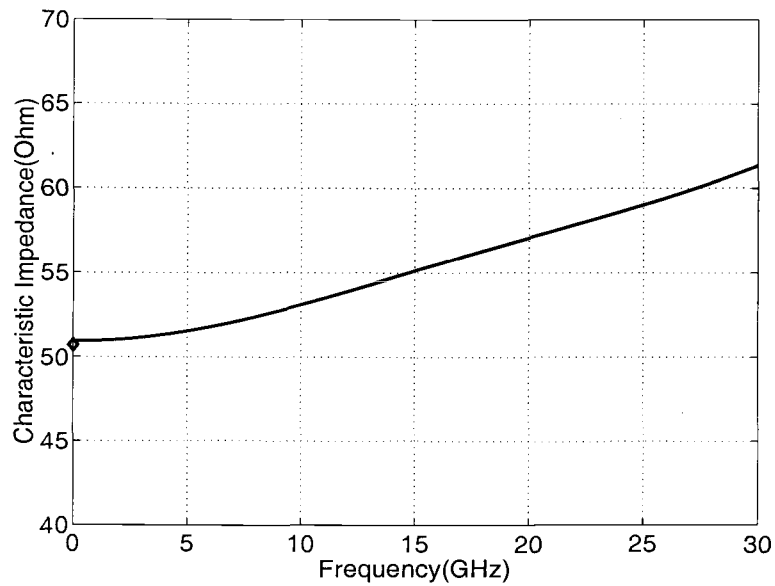


Figure 2.15. Characteristic impedance as a function of frequency (Solid: FDTD, Diamond: Static value).

The FDTD results at low frequencies agree well with the static value.

2.6.3 EQUIVALENT CIRCUIT MODEL

The equivalent circuit model for a uniform single microstrip structure is shown in Figure 2.16. The distributed line parameters R, L, G, C can be obtained from the propagation constant and the characteristic impedance as

$$\gamma \cdot Z_o = R + j\omega L \quad (2.61)$$

and

$$\frac{\gamma}{Z_o} = G + j\omega C. \quad (2.62)$$

For a lossless transmission line, the distributed series resistance $R(\omega)$ and

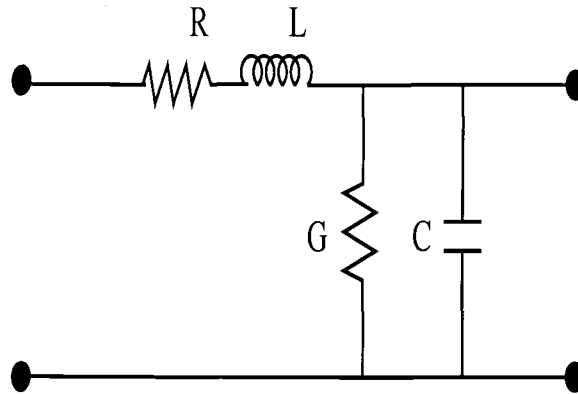


Figure 2.16. Equivalent circuit model for short section of a uniform single microstrip line.

shunt conductance $G(\omega)$ are both zero. Therefore, the frequency-dependent equivalent circuit parameters $L(\omega)$ and $C(\omega)$ are determined as

$$L(\omega) = \frac{\gamma(\omega)Z_o(\omega)}{j\omega} \quad (2.63)$$

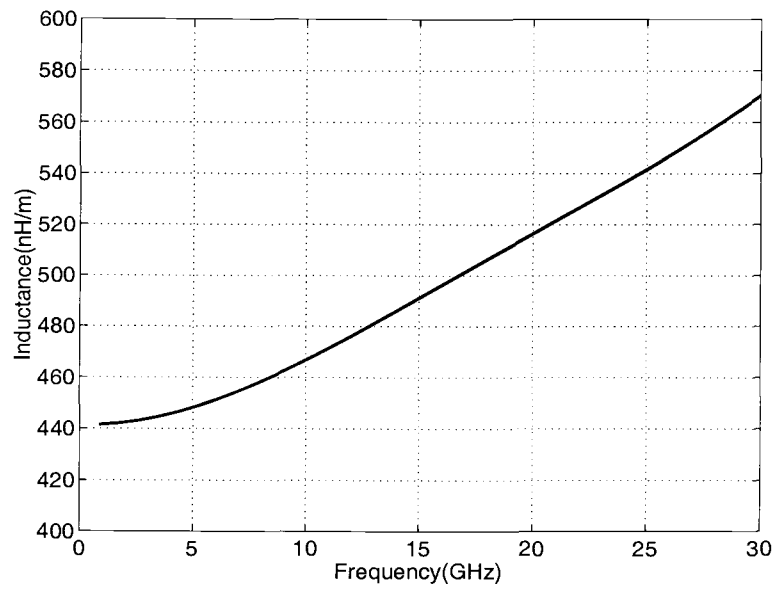
and

$$C(\omega) = \frac{\gamma(\omega)}{j\omega Z_o(\omega)}. \quad (2.64)$$

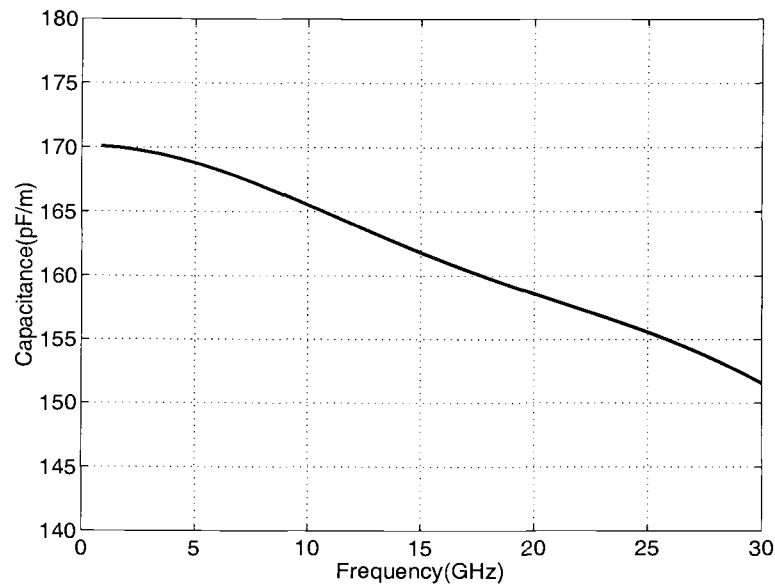
Figure 2.17 shows the distributed transmission line parameters $L(\omega)$ and $C(\omega)$ for a uniform single microstrip.

2.7 CONCLUDING REMARKS

In this chapter, a brief overview of the Finite Difference Time Domain (FDTD) method has been presented and implementation issues have been discussed.



(a)



(b)

Figure 2.17. Inductance and capacitance per unit length for a single microstrip as a function of frequency.

These include the numerical stability, absorbing boundary conditions, the treatment of perfect conductors, conditions on the excitation source, and implementation of the FDTD. As a simple example, a typical uniform single microstrip was analyzed using the FDTD method. It was shown that the characteristic impedance $Z_o(\omega)$, effective dielectric constant $\epsilon_{eff}(\omega)$, and propagation constant $\gamma(\omega)$ of the microstrip can be determined from the time-varying electromagnetic fields. The distributed line parameters such as $L(\omega)$ and $C(\omega)$ can then be determined from the propagation constant and the characteristic impedance. Results for the line parameters of a single uniform microstrip at the low frequency show good agreement with the corresponding static values. As an advantage, the FDTD method provides the broadband characterization of a transmission line structures with one simulation, and directly shows the time evolution of the pulse propagation on the line. In the following chapters, the FDTD method is applied to characterize different uniform and non-uniform coupled microstrip structures.

Chapter 3

CHARACTERIZATION OF MULTIPLE COUPLED LINE STRUCTURES

3.1 INTRODUCTION

Accurate characterization of multiconductor coupled lines using electromagnetic modeling and simulation tools plays an important role in the design of high speed transmission line structures in multilayer media. Uniformly multiple coupled line systems, including the symmetric three-line structures are widely used in filters, directional couplers and impedance matching networks at microwave frequencies [4], [5], [6], [42], [43], [44]. Over the last few decades, much work on the modeling and characterization of multiple coupled lines has been reported (e.g. [45],[46],[47],[48],[49], [50],[51],[52],[53],[54],[55],[56], [57],[58],[59],[60]).

The parameters characterizing coupled line multi-port networks (impedance, admittance, scattering parameters, etc.) can be used in the analysis and design of these circuits. A host of frequency and time domain computational techniques have been developed to characterize multiconductor structures. Time domain techniques can be used directly for time domain simulation, as a virtual TDR to derive distributed models, and to find broadband frequency-dependent properties of multiconductor structures [59], [61], [41]. Even though the extraction procedure for multiple coupled line parameters from time domain computations is well understood in principle, explicit CAD-oriented techniques have not been reported.

In the past years, a general characterization procedure suggested for these structures consists of obtaining the frequency-dependent distributed inductance

and capacitance matrices directly or by extracting the modal parameters by exciting n multiconductor coupled transmission lines [6]. In all of these characterization procedures, the assumption that measurement of voltages and currents at the input ends of the lines provides all normal mode parameters, and thus the corresponding distributed inductance and capacitance matrices, is valid only for multiconductor coupled lines in homogeneous media or symmetrical coupled line structures in inhomogeneous media [61].

An alternate approach for solving such structures is similar to [41] where two different structures are simulated with and without dielectric layer leading to the capacitance and inductance matrices. This alternate approach, however, increases the simulation time by a factor of two, and, in addition, cannot be used for the characterization of complex structures such as coupled microstrip bends. Many methods for modeling multiconductor interconnection lines have been based on quasi-TEM assumption, and the frequency dependence of the distributed circuit parameters has been neglected. A frequency-dependent modeling approach based upon full-wave analysis is necessary. In this chapter, a new methodology for extracting the frequency-dependent propagation constant and characteristic impedance of multiconductor interconnection lines from FDTD simulation is presented.

3.2 EQUIVALENT CIRCUIT MODEL FOR NORMAL MODE APPROACH

The equivalent circuit model can be readily derived from the admittance (impedance) matrix by characterizing the $2n$ -port network shown in Figure 3.1. The procedure for deriving the expression for the admittance or impedance matrix of a general $2n$ -port is well known and is based on the solution of the coupled transmission line equations given in (3.1) and (3.2).

$$\frac{\partial[V]}{\partial z} = -[Z(\omega)][I] \quad (3.1)$$

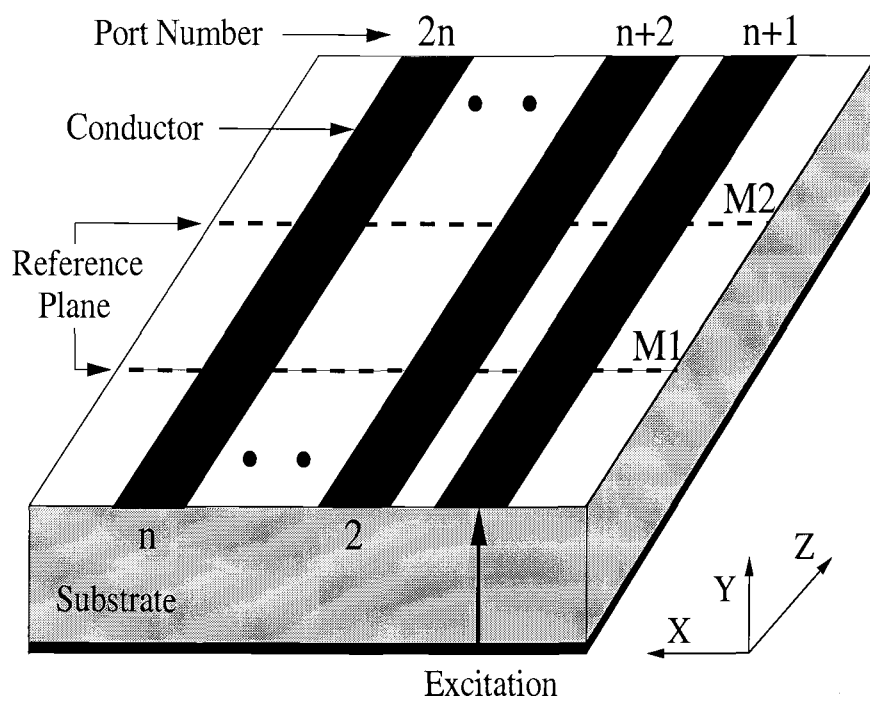


Figure 3.1. General multiconductor coupled lines

$$\frac{\partial[I]}{\partial z} = -[Y(\omega)][V] \quad (3.2)$$

where vectors $[V]$ and $[I]$ represent voltages and currents on the lines and $[Z(\omega)]$ and $[Y(\omega)]$ represent $2n \times 2n$ impedance and admittance matrices, respectively. $[Z(\omega)]$ and $[Y(\omega)]$ are related to the per-unit-length line constant matrices $[R]$, $[L]$, $[G]$, $[C]$ matrices as

$$[Z(\omega)] = [R] + j\omega[L], \quad [Y(\omega)] = [G] + j\omega[C] \quad (3.3)$$

In general, the elements of the $[R]$, $[L]$, $[G]$ and $[C]$ matrices are frequency dependent. The coupled transmission line equations (3.1) and (3.2) are decoupled with the help of the voltage and corresponding current eigenvector matrices $[M_V]$ and $[M_I]$ ($[M_I] = [M_V]^{-T}$), respectively, leading to the characterization of the general n lines $2n$ -port by its admittance matrix. Following Chin [62], the admittance matrix is given by

$$[Y] = \begin{bmatrix} [Y_A] & [Y_B] \\ [Y_B] & [Y_A] \end{bmatrix} \quad (3.4)$$

with

$$[Y_A] = [Y_{LM}] * [M_V][\coth(\gamma_i d)]_{diag}[M_I]^T$$

$$[Y_B] = -[Y_{LM}] * [M_V][\operatorname{csch}(\gamma_i d)]_{diag}[M_I]^T$$

and

$$[Y_{LM}]_{n \times n} = \begin{bmatrix} Y_{LM11} & Y_{LM12} & \cdot & Y_{LM1n} \\ \cdot & \cdot & \cdot & \cdot \\ \cdot & \cdot & \cdot & \cdot \\ Y_{LMn1} & \cdot & \cdot & Y_{LMnn} \end{bmatrix} \quad (3.5)$$

Here γ_i is the i th normal mode propagation constant representing the i th eigenvalue, and d is the length of the uniformly coupled multiconductor system. $[Y_{LM}]$ is the line mode admittance matrix whose element Y_{LMkm} represents the characteristic admittance of the k th line for the m th mode. The operator $'*$ ' was defined in [62] for $[C] = [A] * [B]$ as the product of corresponding elements of matrices $[A]$ and $[B]$.

A flow chart for determining the admittance matrix for a general $2n$ -port n coupled line structure is shown in Figure 3.2.

From equations (3.4) and (3.5), a matrix $[P]$ which includes $[Y_{LM}]$, $[M_V]$, and $[(\gamma_i d)]_{diag}$ can be defined as

$$\begin{aligned} [P] &= [Y_A]^T [Y_B]^{-T} = \\ &= [M_V]^{-T} [\coth(\gamma_i d)]_{diag}^T [\operatorname{csch}(\gamma_i d)]_{diag}^{-T} [M_V]^T. \end{aligned} \quad (3.6)$$

This can be simplified to

$$[P] = [M_V]^{-T} [\cosh(\gamma_i d)]_{diag}^T [M_V]^T. \quad (3.7)$$

Equation (3.7) shows that the normal mode propagation constants γ_i ($i=1, \dots, n$) can be directly obtained from the eigenvalues of matrix $[P]$. Likewise, $[M_V]$ is directly found from the eigenvectors of $[P]$. In the case of an asymmetric multiple coupled line structure, the conventional even and odd mode technique can not be applied due to asymmetry, and, hence, the normal mode parameter approach is used as an alternative. For an asymmetric coupled line, the line mode admittance matrix $[Y_{LM}]$ and the voltage and corresponding current eigenvector matrices $[M_V]$ and $[M_I]$ given by equation (3.5) reduce to a 2 by 2 matrix with the voltage ratio R_c and R_π for the c and π modes, respectively. The line mode admittance matrix and the two eigenvectors can be written as

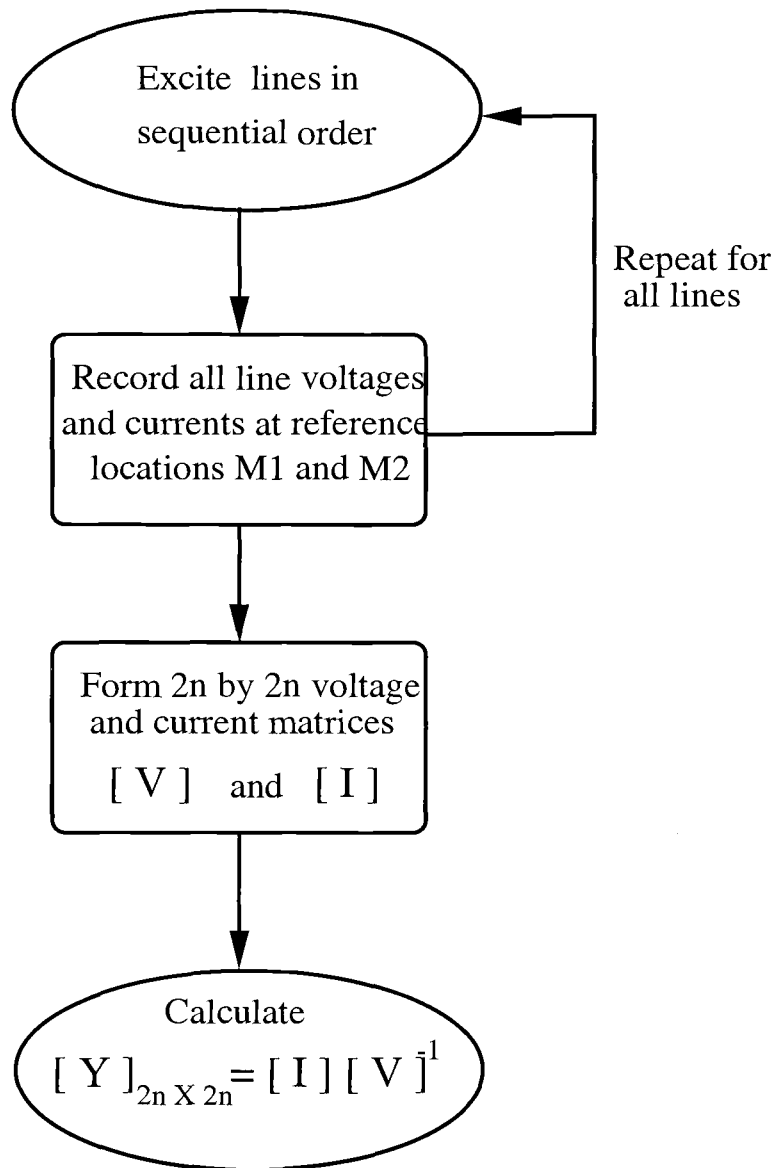


Figure 3.2. Flow chart for determine admittance matrix for a general $2n$ -port n multiple coupled line structure.

$$[Y_{LM}]_{2 \times 2} = \begin{bmatrix} Y_{c1} & Y_{\pi 1} \\ Y_{c2} & Y_{\pi 2} \end{bmatrix} \quad (3.8)$$

$$[M_V] = \begin{bmatrix} 1 & 1 \\ R_c & R_\pi \end{bmatrix} \quad (3.9)$$

and

$$[M_I] = ([M_V]^{-1})^T \quad (3.10)$$

Furthermore, for the general three coupled line case, the line mode admittance matrix $[Y_{LM}]$ and the voltage eigenvector $[M_V]$ reduce to 3 by 3 matrices for the normal modes a, b and c, respectively [62], which can be expressed as

$$[M_V] = \begin{bmatrix} 1 & 1 & 1 \\ R_{a2} & R_{b2} & R_{c2} \\ R_{a3} & R_{b3} & R_{c3} \end{bmatrix} \quad (3.11)$$

and

$$[Y_{LM}]_{3 \times 3} = \begin{bmatrix} Y_{a1} & Y_{b1} & Y_{c1} \\ Y_{a2} & Y_{b2} & Y_{c2} \\ Y_{a3} & Y_{b3} & Y_{c3} \end{bmatrix} \quad (3.12)$$

For the case of symmetric three coupled lines $Y_{a1} = Y_{a3}$, $Y_{b1} = Y_{b3}$ and $Y_{c1} = Y_{c3}$. Details of the normal mode parameters used for multiple coupled transmission lines in the present work can be found in Appendix A.

In general, the [R], [L], [G], and [C] matrices for multiconductor systems are calculated from the computed values for the propagation constants, line mode impedances, and the normalized current eigenvector matrix elements [6], [61], [59]. For the lossless case the expressions for the [L] and [C] matrices reduce to

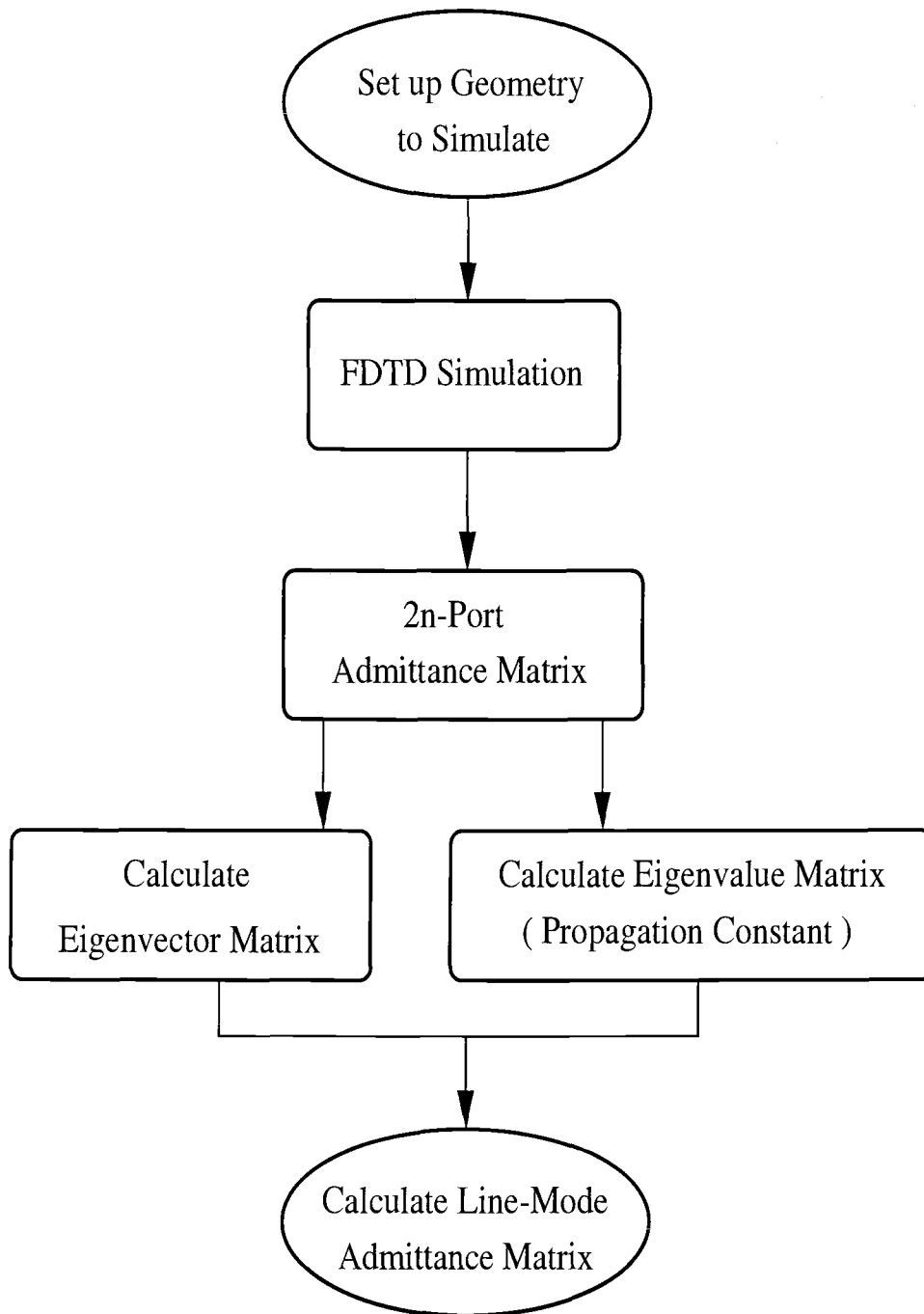


Figure 3.3. Procedure for determining the normal mode parameters of a $2n$ -port multiple coupled line structure.

$$[L(\omega)] = \frac{1}{\omega}([M_I] * [Z_{LM}][\beta_m]_{diag}[M_I]^{-1}) \quad (3.13)$$

$$[C(\omega)] = \frac{1}{\omega}([M_V] * [Y_{LM}][\beta_m]_{diag}[M_V]^{-1}) \quad (3.14)$$

3.3 ANALYSIS OF SYMMETRIC COUPLED LINES

Symmetric coupled lines can be analyzed in terms of the even- and odd-mode approach because the c -(common mode) and π -mode(anti-common) of a symmetric coupled line structure obtained from the normal mode approach are identical to the even- and odd-mode parameters. By definition, the even mode corresponds to the case where the lines have equal voltages and equal currents. The odd mode results when the voltages and currents are equal in magnitude but 180 degrees out of phase. For the structure of n multiple conductor interconnection lines shown in Figure 3.1, n orthogonal excitations are needed. The conductor which is excited is called active line, the other conductors are called sense lines.

As a simple example, a symmetric coupled microstrip line structure of width- s , $W = 0.6\text{mm}$, separation between the two conductors, $S = 0.3\text{mm}$, substrate thickness, $H = 0.635\text{mm}$, and dielectric constant, $\epsilon_r=9.8$ is considered. The metal strips and the ground plane are assumed to be perfectly conducting and infinitely thin, and are defined by setting the tangential component of the electric field to zero. The conductor lines are simulated on an $N_x\Delta x$ by $N_y\Delta y$ by $N_z\Delta z$ computational domain with $\Delta x=60\mu\text{m}$, $\Delta y=90.71\mu\text{m}$ and $\Delta z=100\mu\text{m}$. This corresponds to a conductor width of $W=10\Delta x$ and substrate height of $H=7\Delta y$. The width, N_x , and height, N_y , of the simulation box are chosen to be large enough to not disturb the field distributions near the strips. In all, the entire computational

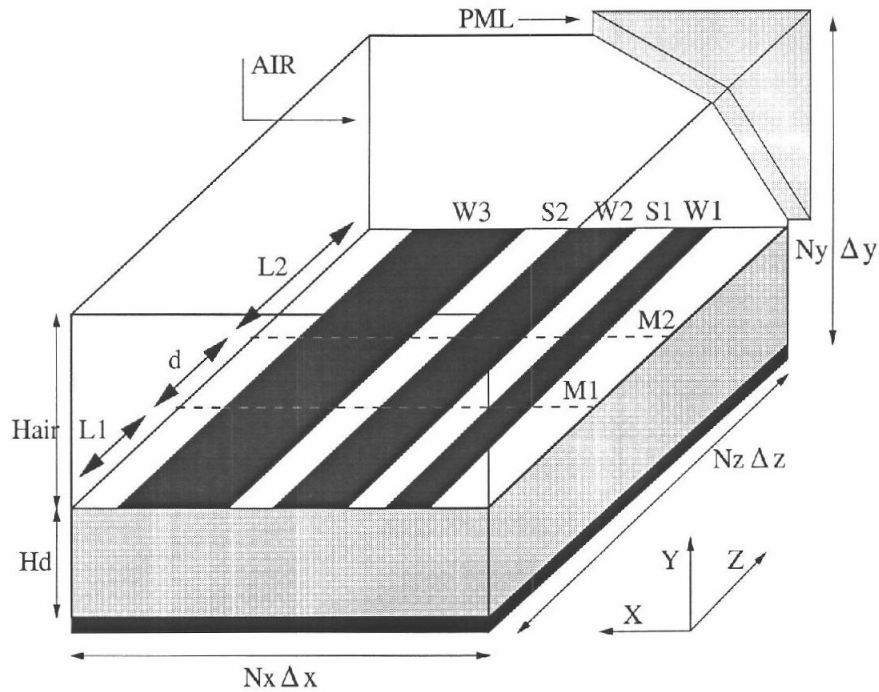


Figure 3.4. Entire computational domain for multiple coupled line structure including PML absorbing boundary cells.

domain including the 6 cells of the PML boundary for each side wall is divided into 81 by 33 by 230 grid cells and shown in figure 3.4.

A time step of $\Delta t = 0.134$ ps is used and the total number of time steps is 1500. The input is excited with a Gaussian pulse with $T = 14.3$ ps and $t_o = 43$ ps. To apply the normal mode parameter approach, each port is excited and then voltages and currents are recorded at the positions M1 and M2 as shown in Figure 3.4. The actual length of conductor is $L1 + d + L2$ with $L1 = 6$ mm, $d = 6$ mm, and $L2 = 12$ mm. Quantitative frequency-domain information contained in the time-domain data is extracted via the Fast Fourier Transform (FFT).

Figures 3.5 and 3.6 show the propagation waveform for a symmetric coupled line structure for orthogonal excitation of the normal mode approach and the even- and odd-mode approach, respectively.

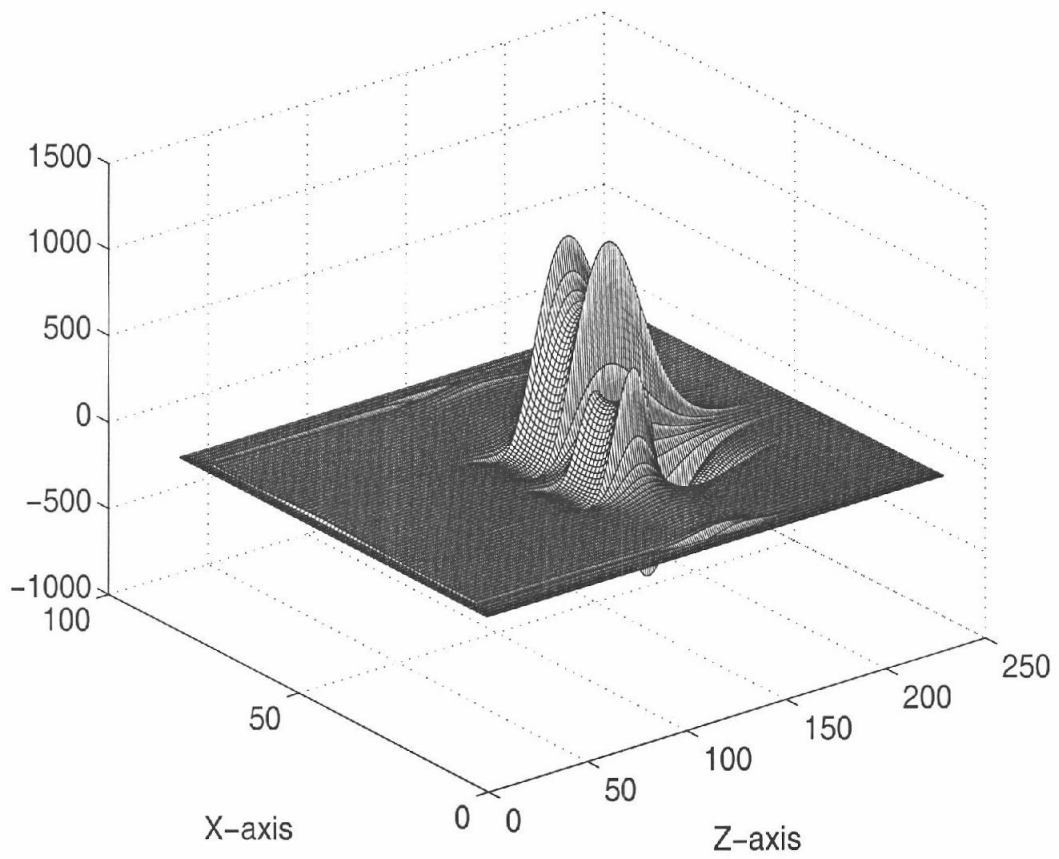


Figure 3.5. Propagation waveform along the Z-direction at 1200 time steps for symmetric coupled lines.

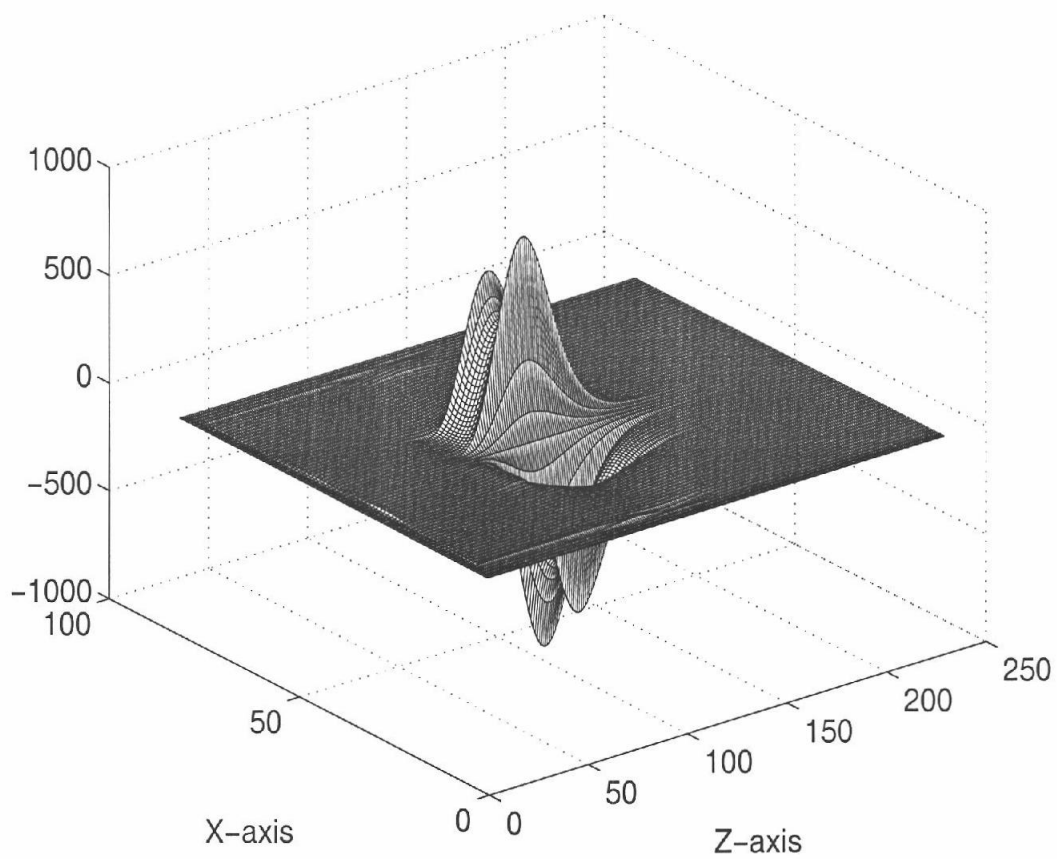


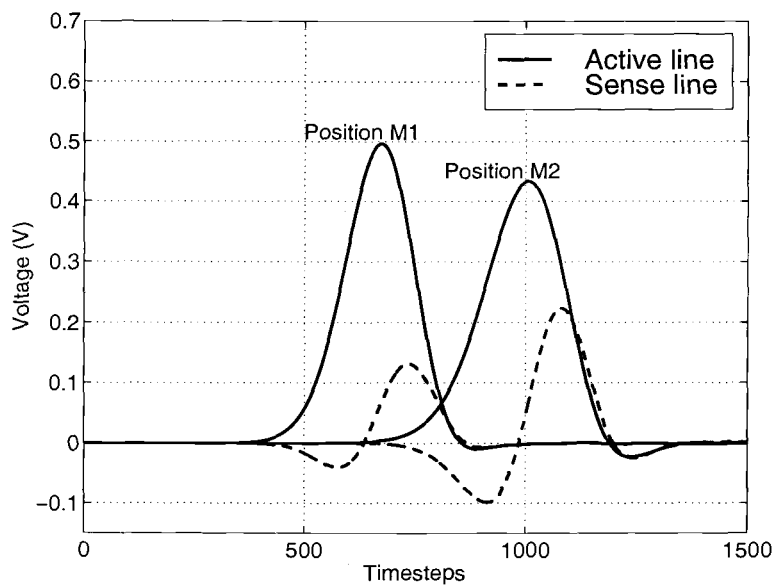
Figure 3.6. Propagation waveform along the Z-direction at 900 time steps for the odd-mode excitation of symmetric coupled lines.

Figure 3.7 shows the transient voltages and currents recorded at $50\Delta z$ and $100\Delta z$ on the active and sense line of the symmetric coupled line structure. Figure 3.8 shows the variation of the characteristic impedance and effective dielectric constant for the symmetric coupled line structure using the proposed normal mode approach and the conventional even- and odd-mode approach. Equivalent circuit parameters such as distributed inductance $L(\omega)$ and capacitance $C(\omega)$ for the symmetric coupled line structure using the normal mode approach and the even/odd-mode approach are shown in Figure 3.9. The results show very good agreement over the entire broadband frequency range.

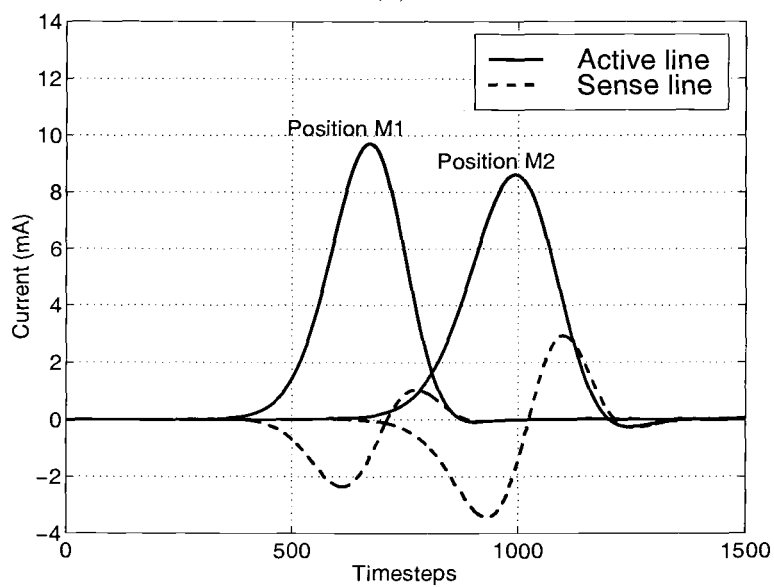
3.4 ANALYSIS OF ASYMMETRIC COUPLED LINES

Many types of coupled distributed parameter circuits have been used in various applications including couplers, filters, impedance transformer, and slow-wave structures. It is convenient to describe a coupled pair of lines in terms of normal modes of excitation which have been called co- or c-mode (denoted by a subscript c) and anti- or π -mode (denoted by a subscript π). These normal mode parameters are derived in terms of the equivalent series- and shunt-distributed parameters such as impedances and admittances of the lines.

An asymmetric coupled line structure can be characterized in terms of c and π modes using the normal mode parameter approach. The dimensions of the test structure are chosen to be $W1 = 0.6\text{mm}$, $S = 0.3\text{mm}$ and $W2 = 1.2\text{mm}$ with the same dielectric substrate specifications as for the case of symmetric coupled lines. For the purpose of FDTD simulation, the computational domain is considered to be 90 by 40 by 206 grid cells with time step $\Delta t = 0.176$ ps. Figure 3.10 shows the propagation waveform recorded at 800 timesteps and Figure 3.11 shows voltages and currents recorded for the active and sense line at positions M1 and M2, respectively. From the voltage and current recorded on the active and sense line, the line mode admittance matrix $[Y_{LM}]$ and the voltage and corresponding

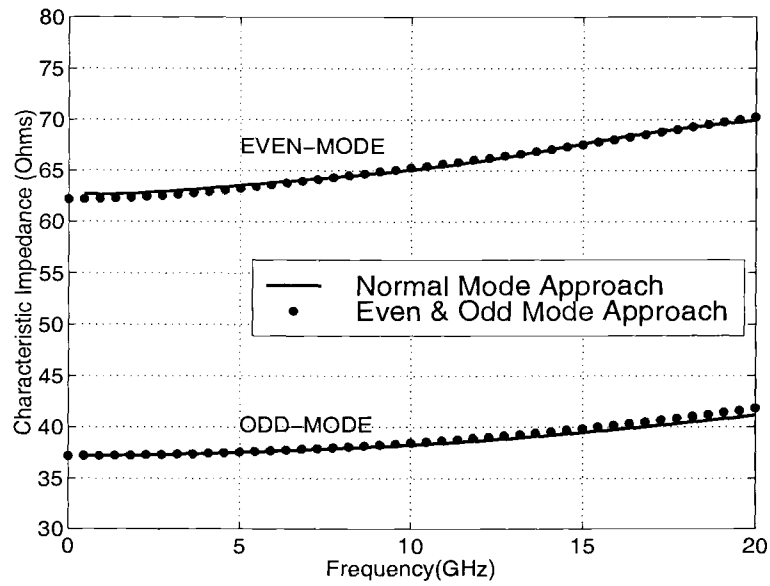


(a)

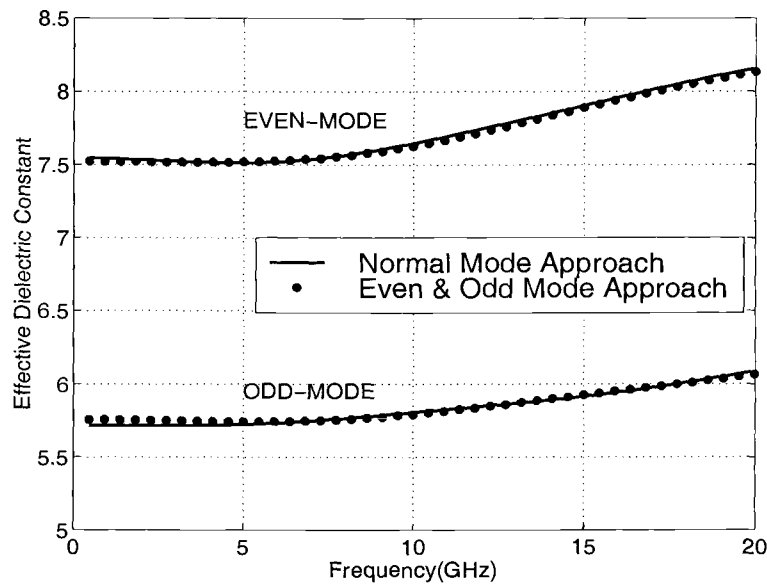


(b)

Figure 3.7. The transient time (a) voltage and (b) current recorded on the active and sense line for symmetric coupled lines.

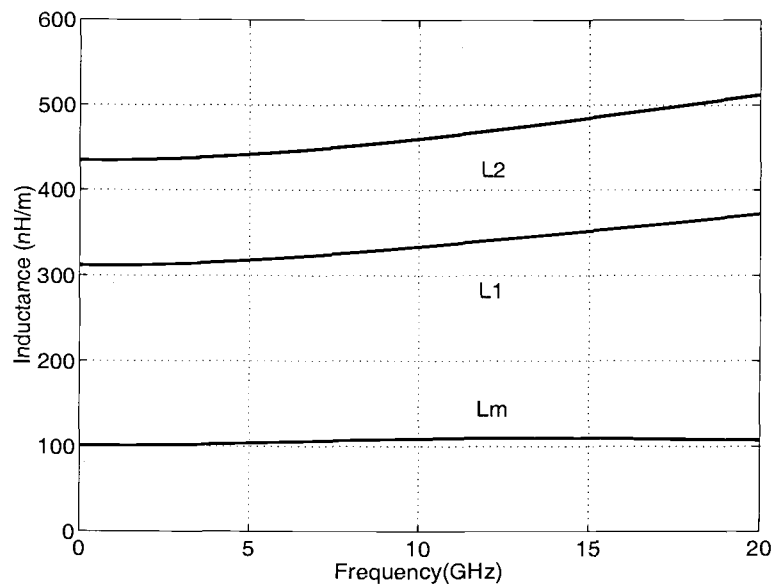


(a)

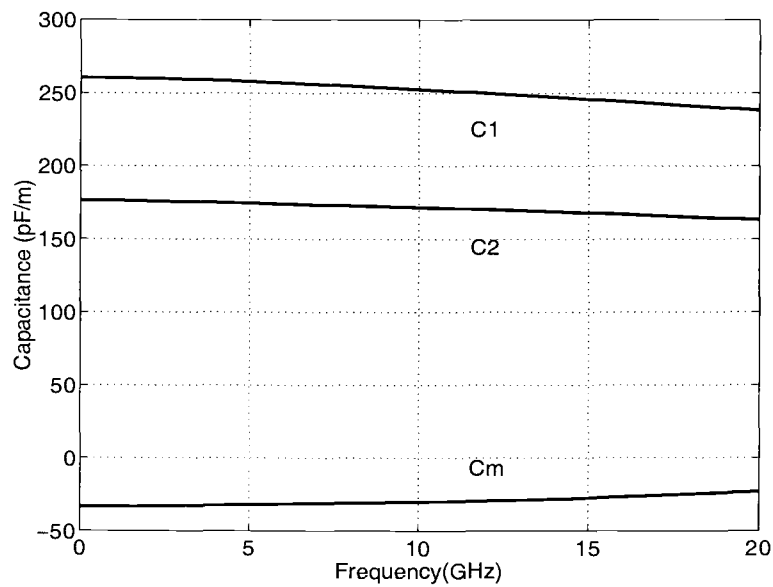


(b)

Figure 3.8. Comparison with two approaches (a) Characteristic impedance and (b) effective dielectric constant as functions of frequency for a symmetric coupled line structure.



(a)



(b)

Figure 3.9. (a) Inductance and (b) capacitance as functions of frequency for symmetric coupled lines.

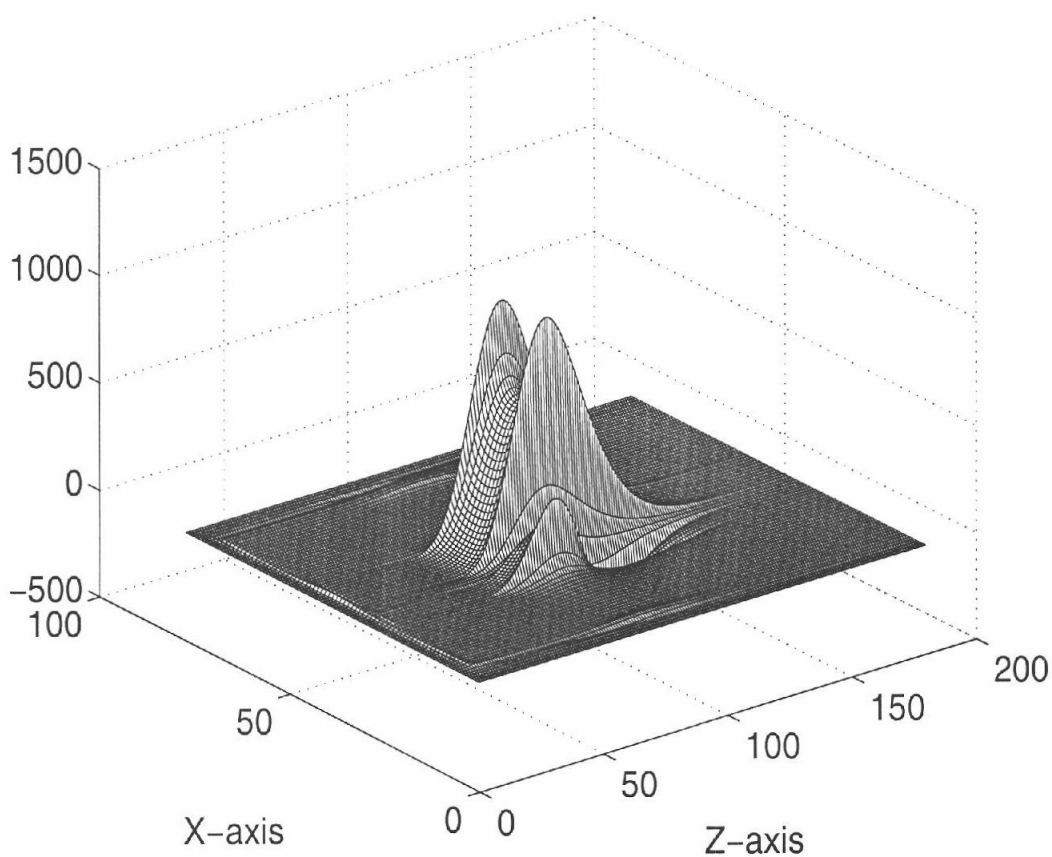
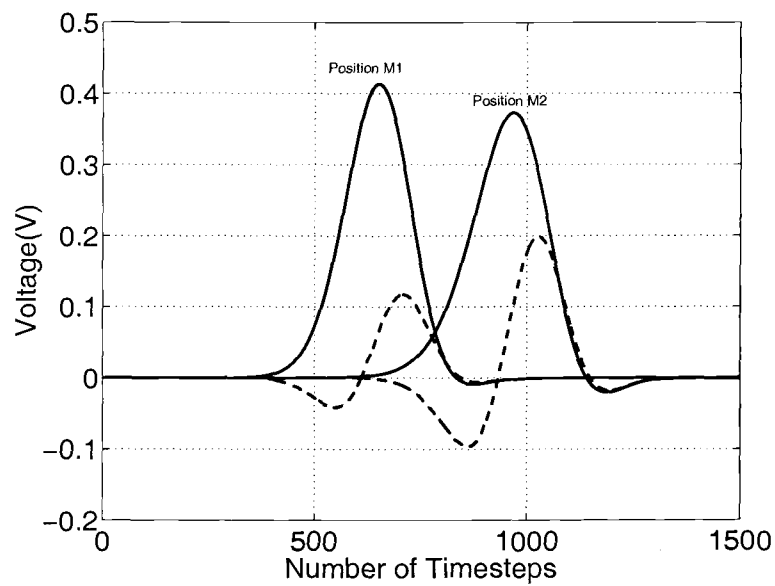


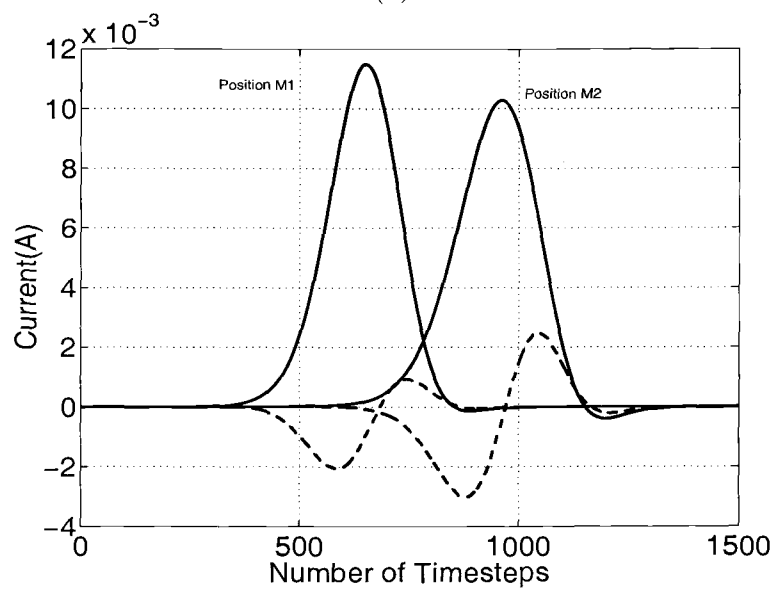
Figure 3.10. Propagation waveform along Z-axis at 800 time steps for an asymmetric coupled line structure.

current eigenvector matrices, $[M_V]$ and $[M_I]$, are derived following the procedure described in section 3.2.

Figures 3.12, 3.13 and 3.14 show the variation of line mode impedance, effective dielectric constant and the line mode voltage ratio for the asymmetric coupled line as functions of frequency, respectively. Comparisons with a full-wave Spectral Domain method [6] are also included. The frequency-dependent self- and mutual-inductance $L(\omega)$ and self- and mutual-capacitance $C(\omega)$ are shown in Figure 3.15.



(a)



(b)

Figure 3.11. The transient time (a) voltage and (b) current recorded on the active and sense line for an asymmetric coupled line structure.

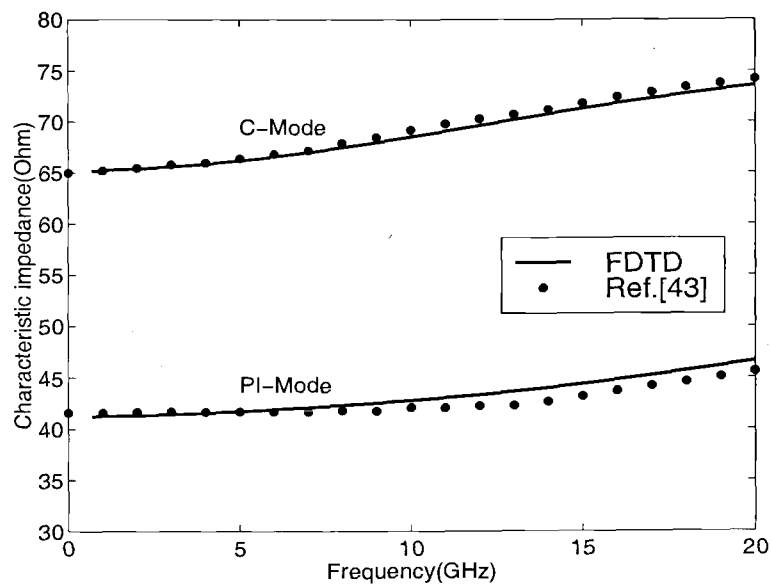


Figure 3.12. Comparison between FDTD and a full-wave spectral domain method of the characteristic impedance for an asymmetric coupled line structure.

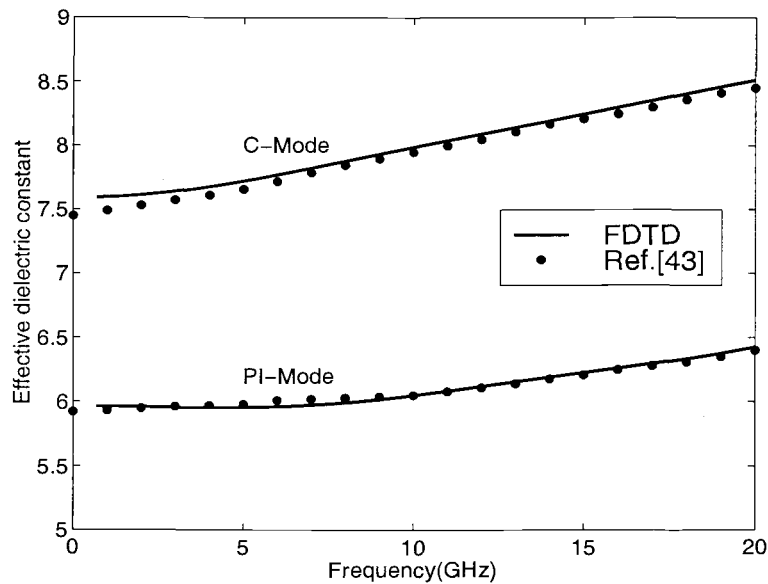


Figure 3.13. Comparison between FDTD and a full-wave spectral domain method of effective dielectric constant for an asymmetric coupled line structure.

3.5 ANALYSIS OF ASYMMETRIC THREE COUPLED LINES

The third example is an asymmetric three coupled interconnection line structure. The dimensions of the structure are $W1 = 0.3\text{mm}$, $S1 = 0.2\text{mm}$, $W2 = 0.6\text{mm}$, $S2 = 0.4\text{mm}$ and $W3 = 1.2\text{mm}$ with dielectric substrate specifications the same as for the case of symmetric coupled line. The entire structure is divided into 98 by 40 by 206 grid cells for calculation with $\Delta t = 0.176$ ps. Figure 3.16 shows the voltage waveform on the three conductors after 600 and 900 iteration time steps with the excitation of line 3 along the Z -axis. The transient voltages and currents recorded at $50\Delta z$ and $100\Delta z$ on the active line, the first sense line, and the second sense line of the asymmetric three coupled line structure are shown in Figure 3.17. Figures 3.18, 3.19 and 3.20 show the variation of line mode characteristic impedances, effective dielectric constants and voltage ratios as functions of frequency. The frequency-dependent self- and mutual inductance

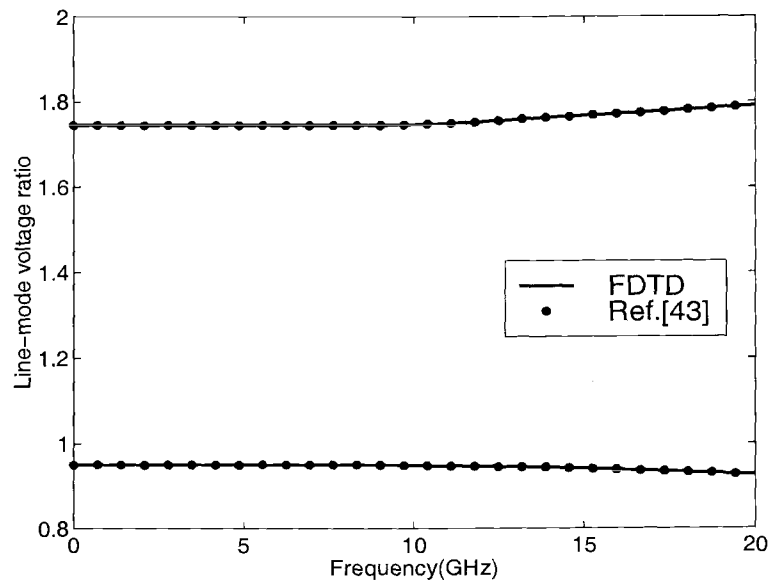
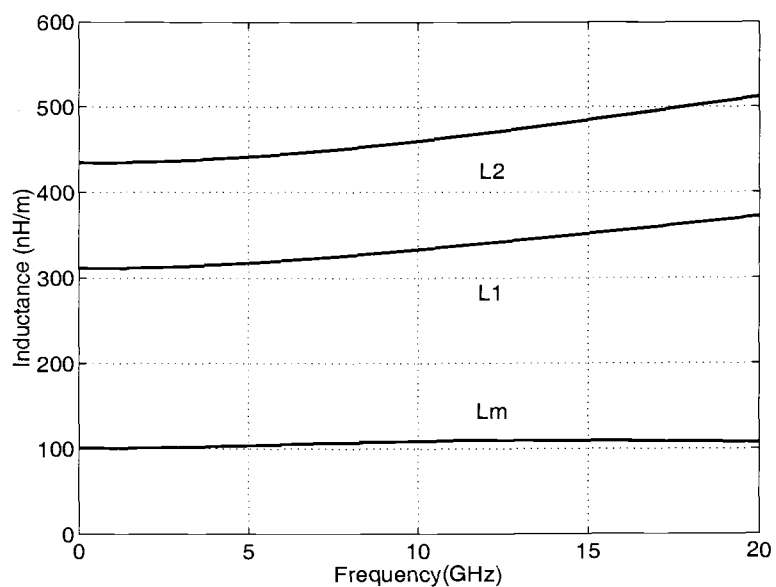


Figure 3.14. Comparison between FDTD and a full-wave spectral domain method of line-mode voltage ratio for an asymmetric coupled line structure.

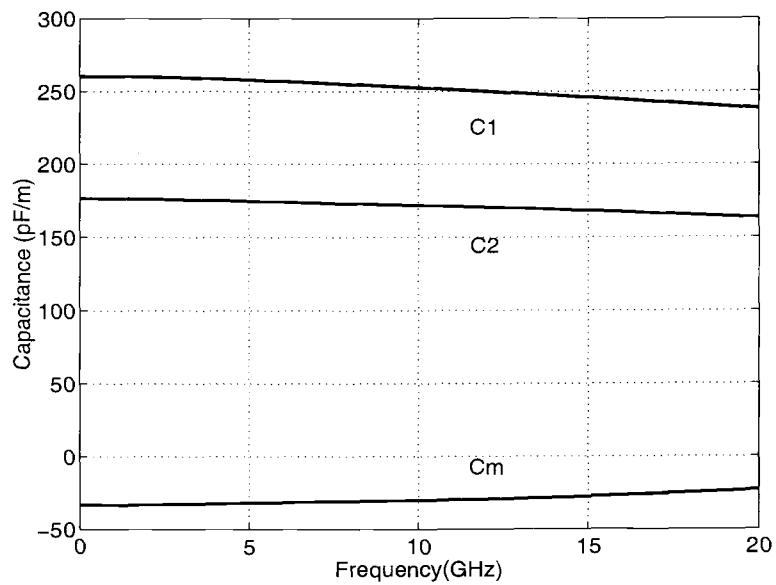
$L(\omega)$ and self and mutual capacitance $C(\omega)$ for asymmetric three coupled line structure are shown in Figure 3.21.

3.6 CONCLUDING REMARKS

In this chapter, the normal mode parameter approach for multiple coupled transmission lines has been formulated. The full-wave Finite Difference Time Domain (FDTD) method for computation of the frequency-dependent characteristics of general asymmetric coupled lines in a multilayer environment has been presented. The results show good agreement for effective dielectric constant and characteristic impedance for multiple coupled lines between the normal mode approach using FDTD and a full-wave spectral domain approach. The results for all the frequency-dependent propagation characteristics should be very useful in the analysis and design of multiple coupled line structures such as couplers and



(a)



(b)

Figure 3.15. (a) Inductance and (b) capacitance as functions of frequency for an asymmetric coupled line structure.

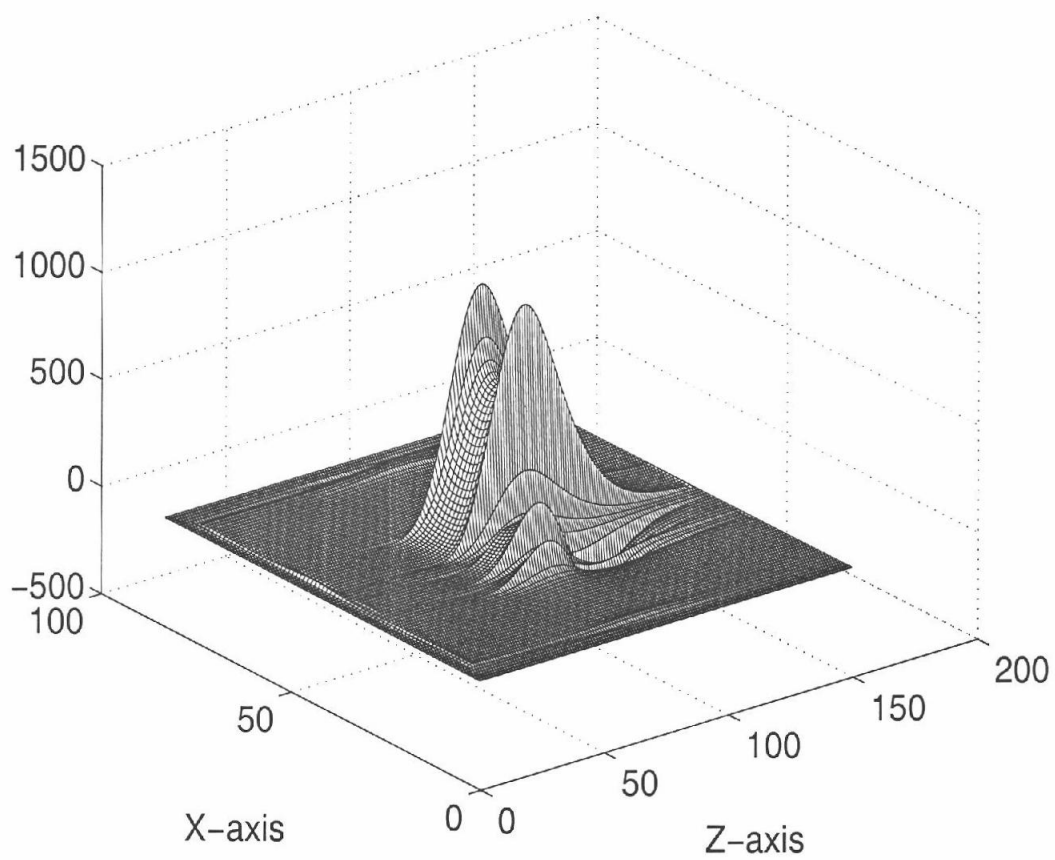
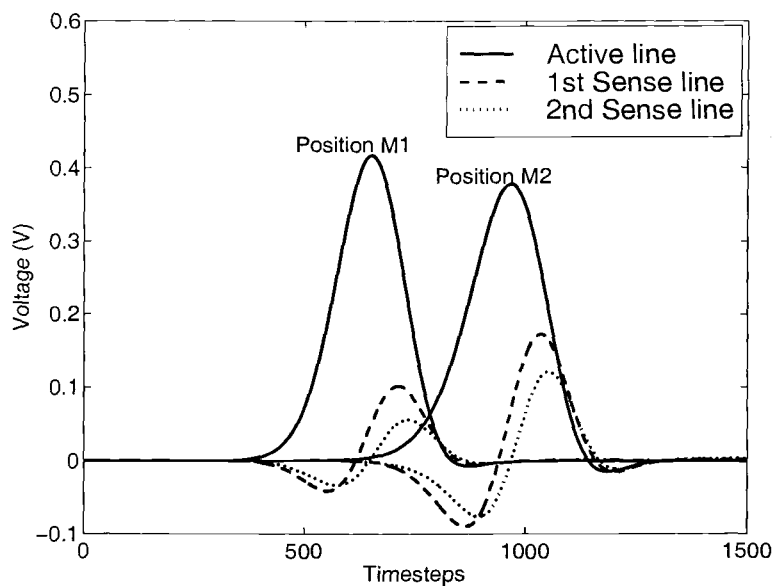
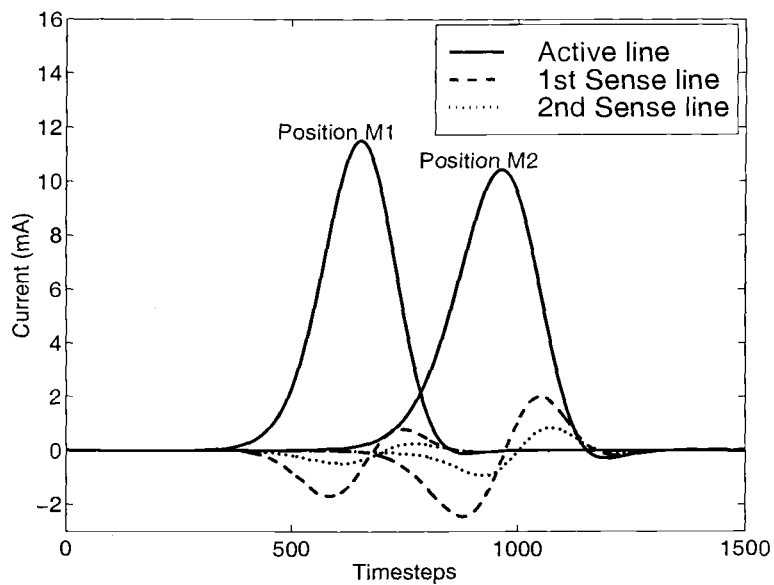


Figure 3.16. Propagation waveform along Z-direction at 900 time steps for an asymmetric three coupled line structure.



(a)



(b)

Figure 3.17. The transient (a) voltage and (b) current recorded on active line and two sense lines for a three coupled line structure.

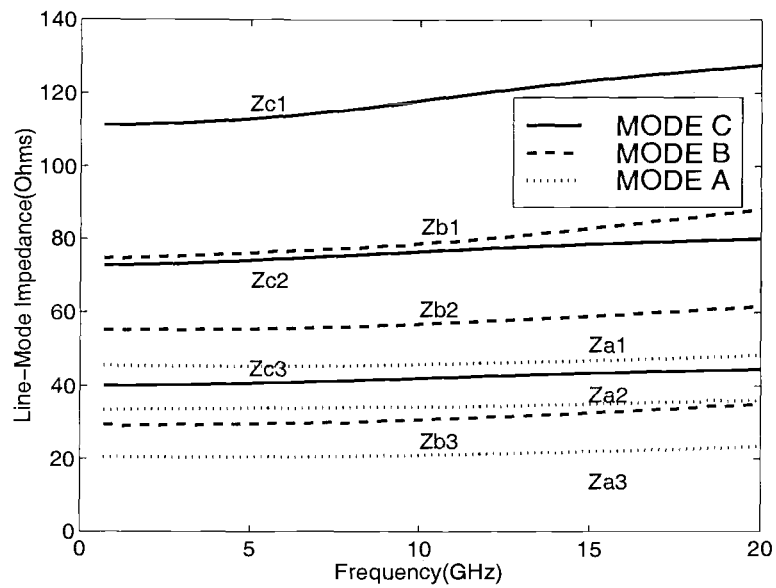


Figure 3.18. Line mode characteristic impedance for a three coupled line structure.

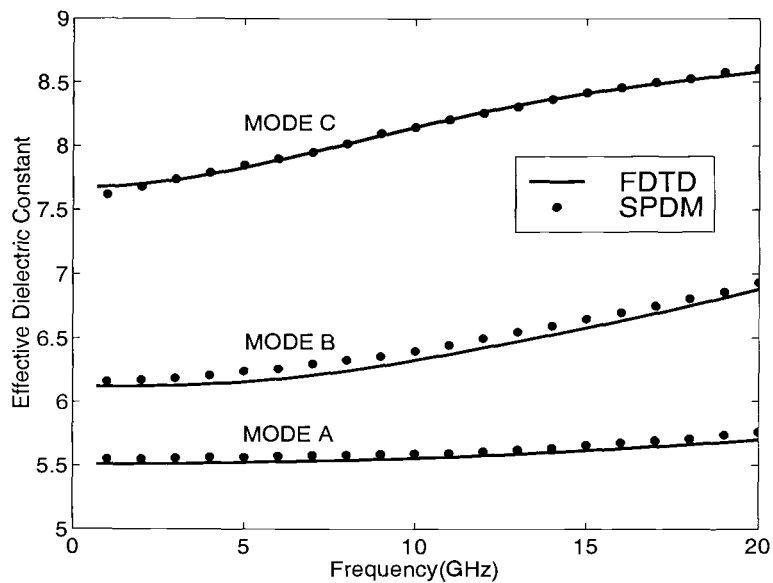


Figure 3.19. Line mode effective dielectric constant for an asymmetric three coupled line structure (SPDM = full-wave spectral domain method).

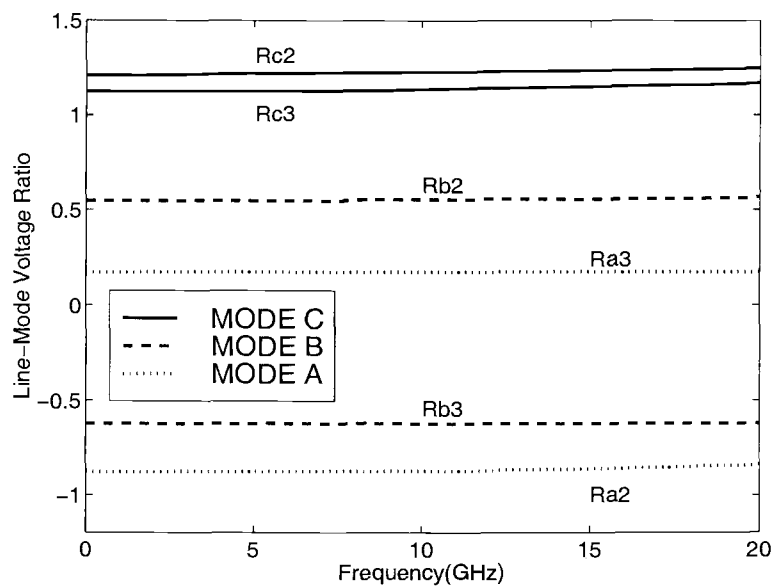
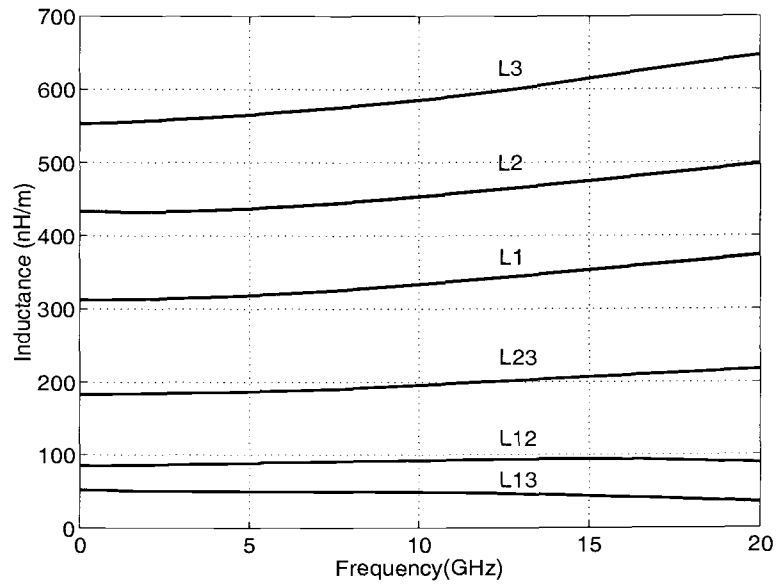
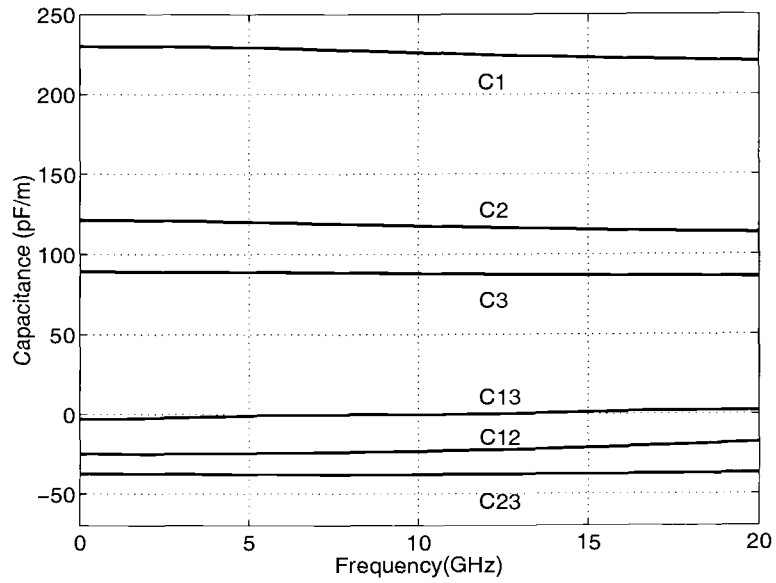


Figure 3.20. Line mode voltage ratio for a three coupled line structure.

filters.



(a)



(b)

Figure 3.21. (a) Inductance and (b) capacitance as functions of frequency for a three coupled line structure.

Chapter 4

TRANSMISSION LINES ON LOSSY SILICON SUBSTRATE

4.1 INTRODUCTION

Silicon-based technology is increasingly used for RF and microwave integrated circuits because of the distinct advantages of low cost and well developed fabrication techniques. Interconnects in silicon-based ICs can be classified as Metal-Insulator-Semiconductor(MIS) transmission lines, which consist of metal lines on semiconducting substrates, isolated by a thin SiO₂ oxide layer. The semiconducting substrate is characterized by its dielectric constant and conductivity.

In previous work Guckel et al. investigated the transmission properties of such structures including the analysis based on a parallel-plate waveguide approach of MIS microstrip lines [63]. In the early 1970s, Hasegawa [64] analyzed theoretically the transmission properties of microstrip lines using a parallel-plate waveguide model with a perfectly conducting line of infinite width for the MIS structure and compared them with experimental results. These works introduced the existence of three fundamental propagation modes caused by the finite resistivity of the semiconducting substrates. These modes are classified as slow-wave mode, dielectric quasi-TEM mode, and skin-effect mode. The mode that dominates depends mainly on the line geometry, the substrate resistivity, and the signal frequency.

More recently efficient and versatile methods for the characterization of low-loss MIS structures have evolved [65], [66]. In 1984, Seki and Hasegawa analyzed the crosstalk and interconnection delay in the interconnection system of high-speed LSI/VLSI circuits [67], [68], and G. Ghione studied a lossy quasi-TEM

model for multiconductor bus lines on semi-insulating GaAs substrates and analyzed crosstalk, propagation signal delay and pulse distortion in high-speed circuits [69]. J. Gilb presented the pulse distortion and coupling of multilayer symmetric and asymmetric coupled microstrip lines using a full-wave spectral domain technique [70], [71], [72]. A lot of researchers investigated the slow-wave coplanar waveguide MIS structure for MMICs [73],[74],[75],[76],[77],[78],[79], [80],[81],[82].

Microstrip structures realized on a Si-SiO₂ substrate are known to be quite sensitive to the conductive properties of Si because of the particular field configuration. Goel reported a crosstalk analysis for a multi-layer multi-conductor system in the same dielectric [83]. Multi-layer multi-conductor configurations form a part of most of the high-speed circuits. Tripathi et al. reported analytical and numerical techniques for the pulse propagation characteristics such as delay, distortion, and crosstalk in multilevel interconnections associated with high-speed digital ICs including VLSI chips [84]. Chan et al. presented the propagation characteristics of waves along a periodic array of parallel signal lines in a multi-layered structure in the presence of a periodically perforated ground plane and the characterization of the discontinuities made of two orthogonally crossed strip lines on a suspended substrate [85]. Several researchers characterized the discontinuity formed by two orthogonally crossed strip lines [86],[87], [88].

In this chapter, single and symmetric coupled MIS transmission line structures on Si-SiO₂ substrates as shown in Figure 4.1 are analyzed using the FDTD method. Then, a new substrate shielding structure consisting of grounded cross-bars is examined, and microstrip characteristics for single and symmetric coupled lines over the cross-bar shielding structure are presented. The substrate-shielded microstrip structure is essentially a two-layered microstrip line with a series of cross-bar conductors at the interface between Si and SiO₂ layer. The cross-bar conductors are perpendicular to the main transmission line strip conductor and are assumed to be at ground potential. A full-wave analysis of the cross-bar

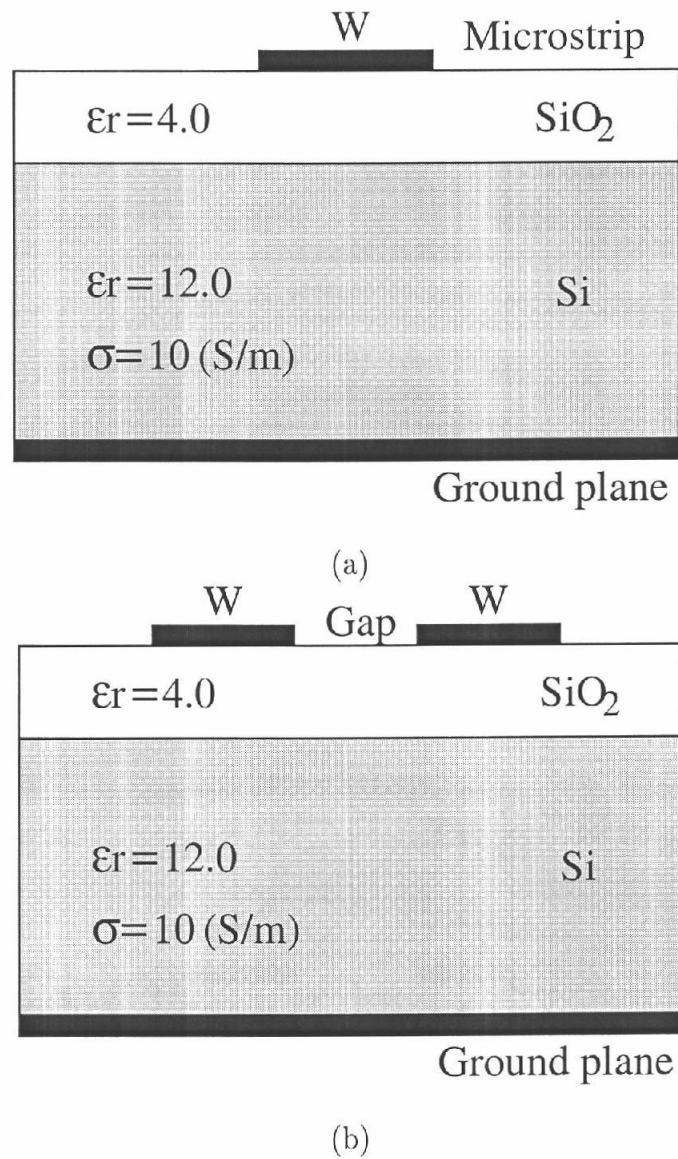


Figure 4.1. (a) Single microstrip and (b) symmetric coupled microstrip MIS structure.

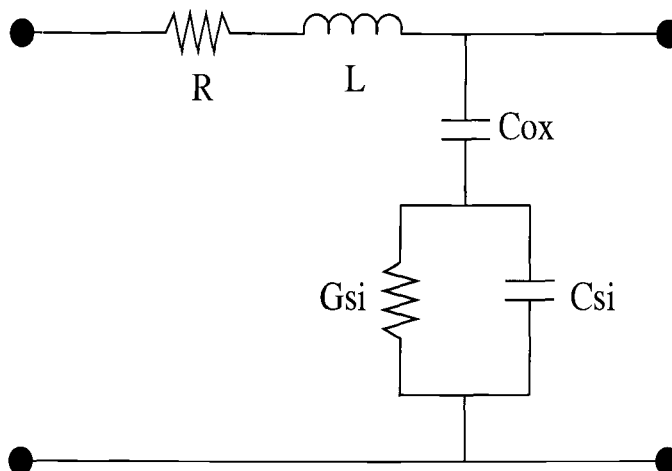


Figure 4.2. The distributed equivalent circuit for a single microstrip MIS structure.

structure is carried out using FDTD. Equivalent circuit parameters are extracted for substrate-shielded microstrip structures from FDTD simulations, and a comparison is made with the two-layered microstrip structure without substrate shield.

4.2 SINGLE MICROSTRIP MIS STRUCTURE

A single microstrip MIS structure is shown in Figure 4.1(a). It is assumed that the oxide layer is lossless and the silicon layer is lossy. The conductor loss is assumed to be zero. The characteristic impedance $Z_o(\omega)$ and the propagation constant $\gamma(\omega)$ of the signal line are obtained from the ratio of the Fourier-transformed voltage and current and the ratio of the voltages taken at two different locations. Once $\gamma(\omega)$ and $Z_o(\omega)$ are obtained, the distributed transmission line parameters for a single line $R(\omega)$, $L(\omega)$, $G(\omega)$, and $C(\omega)$ can be calculated in a similar manner as for a lossless transmission line, using the procedure described in Chapter 2. The equations for obtaining the distributed series impedance and shunt admittance

are

$$\gamma(\omega) \cdot Z_o(\omega) \equiv R(\omega) + j\omega L(\omega) \quad (4.1)$$

$$\frac{\gamma(\omega)}{Z_o(\omega)} \equiv G(\omega) + j\omega C(\omega) \quad (4.2)$$

The equivalent circuit for a small length of the structure is Figure 4.2 which consists of series resistance $R(\omega)$ inductance $L(\omega)$, shunt capacitances $C_{ox}(\omega)$ for the oxide layer and capacitance $C_{si}(\omega)$ and conductance $G_{si}(\omega)$ for the silicon layer. It is assumed that the capacitance and the conductance for the silicon layer are related as

$$\frac{C_{si}}{G_{si}} = \frac{\epsilon_{si}}{\sigma_{si}} \quad (4.3)$$

where ϵ_{si} and σ_{si} are the dielectric constant and conductivity of Si layer, respectively. As mentioned above, the overall admittance $Y(\omega)$ is given by

$$Y(\omega) = G(\omega) + j\omega C(\omega) \quad (4.4)$$

Using equations (4.3) and (4.4), the equivalent circuit parameters $C_{ox}(\omega)$, $G_{si}(\omega)$, and $C_{si}(\omega)$ for the oxide and silicon layer can be calculated as

$$G_{si}(\omega) = \frac{\sigma^2}{\text{Re}(Z(\omega))(\sigma^2 + \omega^2\epsilon^2)} \quad (4.5)$$

$$C_{si}(\omega) = \frac{\sigma\epsilon}{\text{Re}(Z(\omega))(\sigma^2 + \omega^2\epsilon^2)} \quad (4.6)$$

$$C_{ox}(\omega) = \frac{G_{si}^2 + \omega^2 C_{si}^2}{\omega \text{Im}(Z(\omega))(G_{si}^2 + \omega^2 C_{si}^2) + \omega^2 C_{si}} \quad (4.7)$$

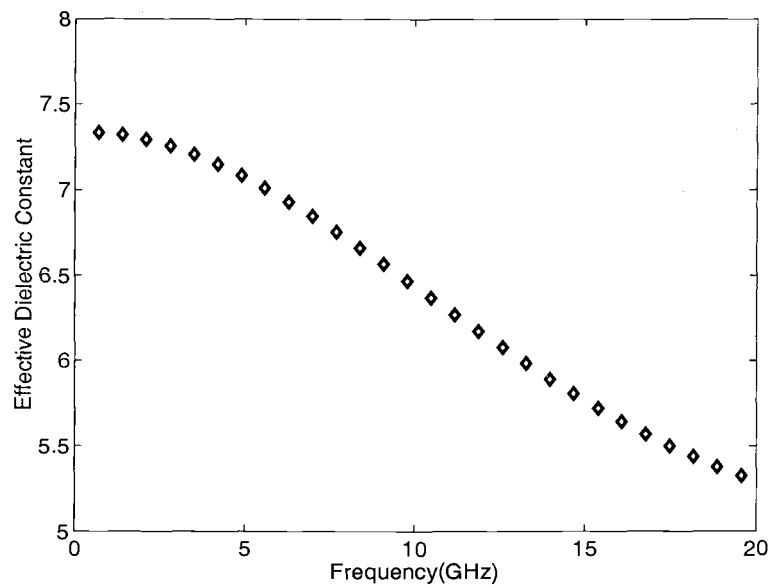
where $Z(\omega) = 1/Y(\omega)$.

As an example, a single microstrip MIS structure is simulated using FDTD. The metal strips and the ground plane are assumed to be perfectly conducting and infinitely thin, and are defined by setting the tangential component of the electric field to zero. The conductor line is simulated on an $N_x \Delta x$ by $N_y \Delta y$ by $N_z \Delta z$ computational domain with $\Delta x = 10 \mu\text{m}$, $\Delta y = 12.5 \mu\text{m}$ and $\Delta z = 20 \mu\text{m}$. This corresponds to a conductor width $W = 5 \Delta x$ of the signal line and substrate heights $H1 = 16 \Delta y$ and $H2 = 2 \Delta y$. The width, N_x , and height, N_y , of the simulation box are chosen to be large enough to not disturb the field distributions near the strips. In all, the entire computational domain including the PML boundary of 8 cells is divided into 58 by 50 by 280 grid cells.

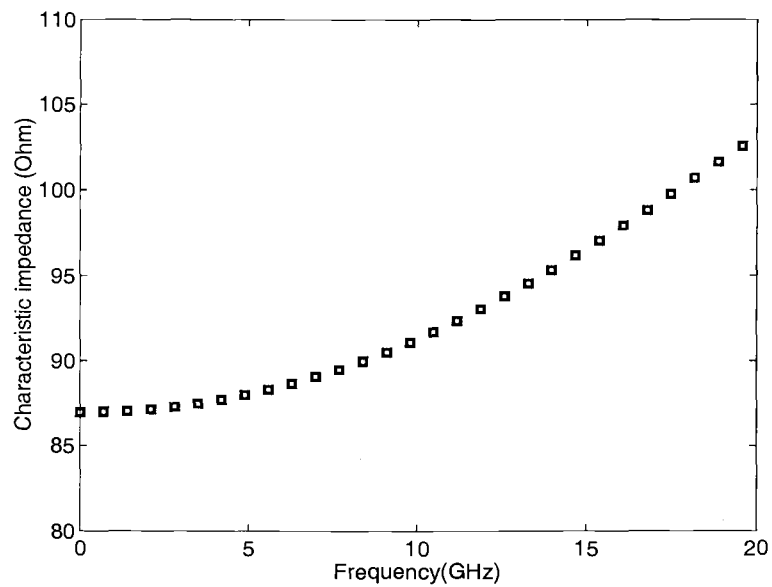
A time step of $\Delta t = 0.0218$ ps is used and the total number of time steps is 2500. The input is excited with a Gaussian pulse with $T = 2.33$ ps and $t_o = 6.98$ ps. Figures 4.3 to 4.7 show the results for a single line structure for the conductivity $\sigma = 10$ (siemens/m) of the silicon layer. Figure 4.3 shows the frequency-dependent effective dielectric constant $\epsilon_{eff}(\omega)$ and characteristic impedance $Z_o(\omega)$. The distributed inductance, conductance and capacitance as well as the attenuation constant are shown in Figures 4.4 and 4.5, respectively. The extracted equivalent circuit parameters, C_{ox} , G_{si} and C_{si} for both oxide and silicon layer are given in Figures 4.6 and 4.7.

4.3 SYMMETRIC COUPLED LINE MIS STRUCTURE

The symmetric coupled microstrip line is very useful for the design of various directional couplers. The symmetric coupled line MIS structure and its lumped equivalent circuit are shown in figure 4.1(b). Basically, there are two fundamen-

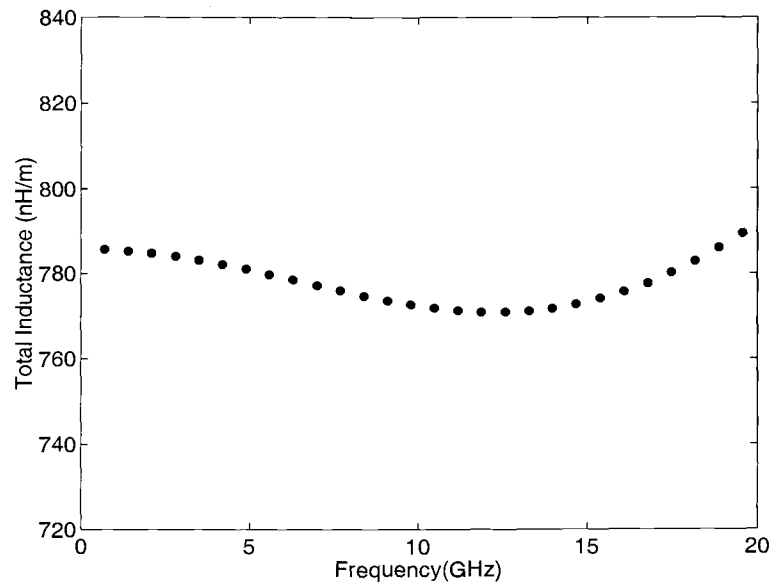


(a)

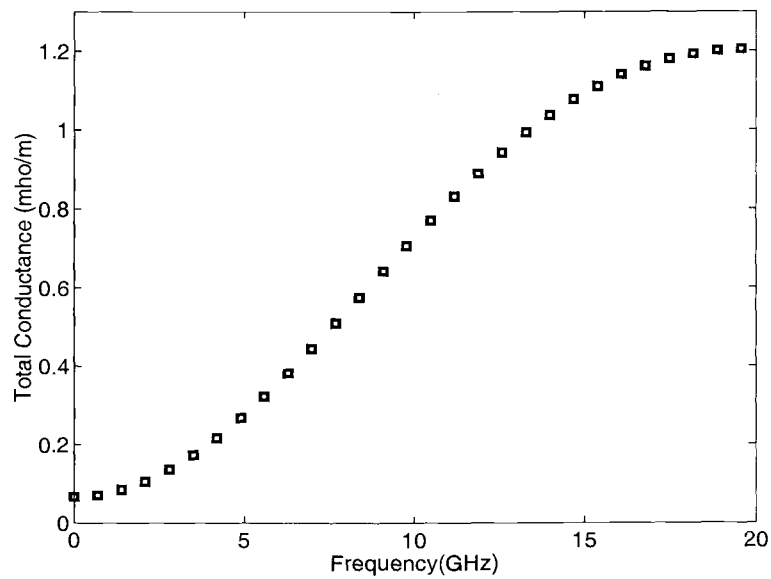


(b)

Figure 4.3. (a) Effective dielectric constant and (b) characteristic impedance for a single MIS line for the substrate conductivity of $\sigma = 10(S/m)$.

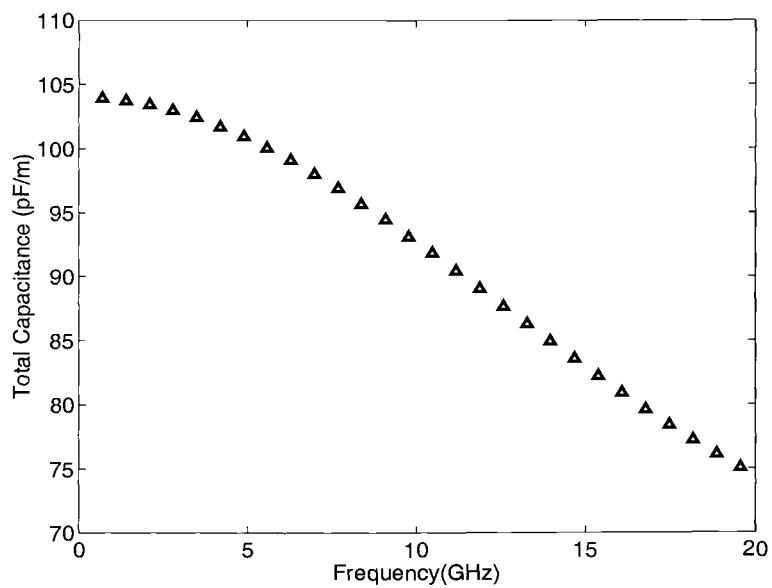


(a)

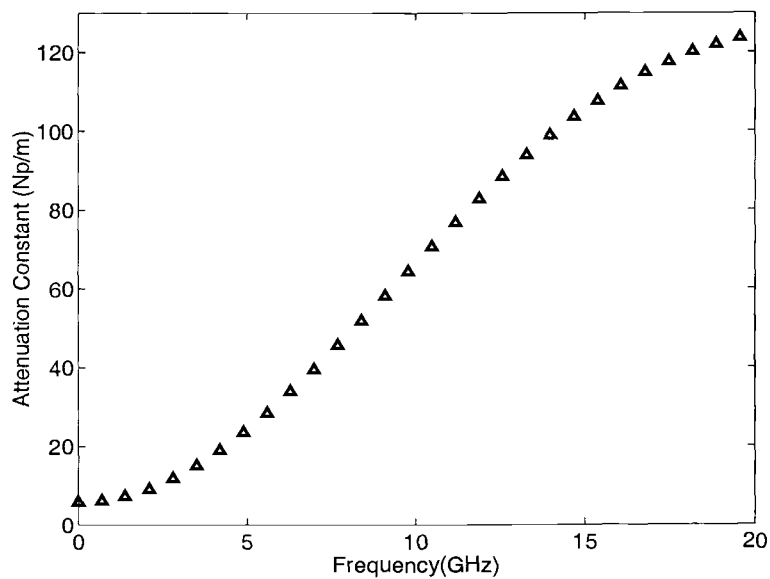


(b)

Figure 4.4. (a) Total inductance and (b) conductance for a single MIS line for the substrate conductivity of $\sigma = 10(S/m)$.

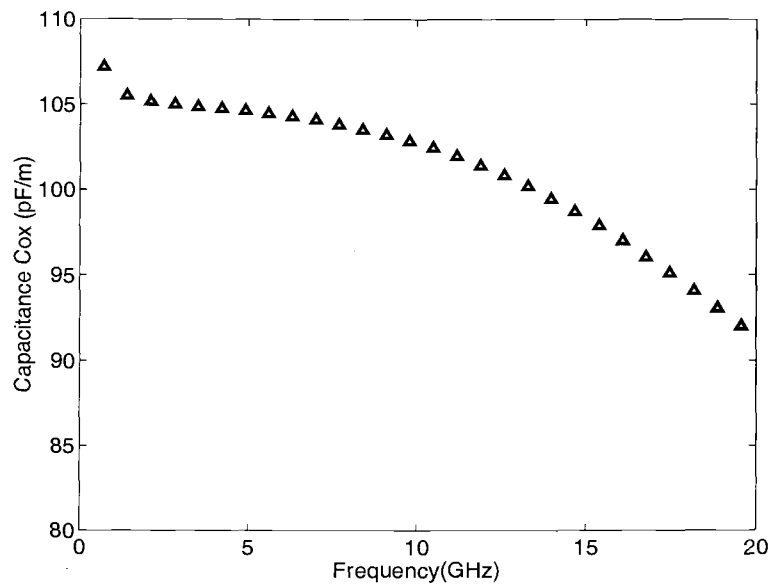


(a)

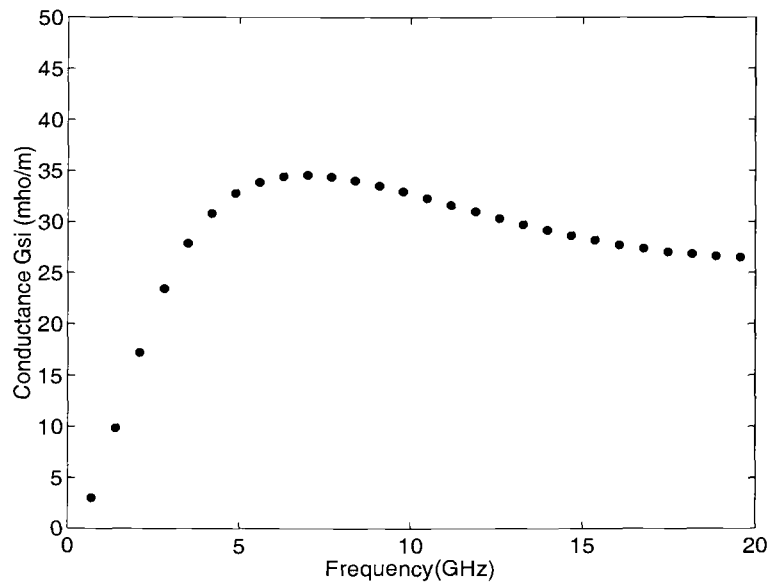


(b)

Figure 4.5. (a) Total capacitance and (b) attenuation constant for a single MIS line structure for the substrate conductivity of $\sigma = 10(S/m)$.



(a)



(b)

Figure 4.6. (a) Capacitance C_{ox} and (b) conductance G_{si} for a single MIS line for the substrate conductivity of $\sigma = 10(S/m)$.

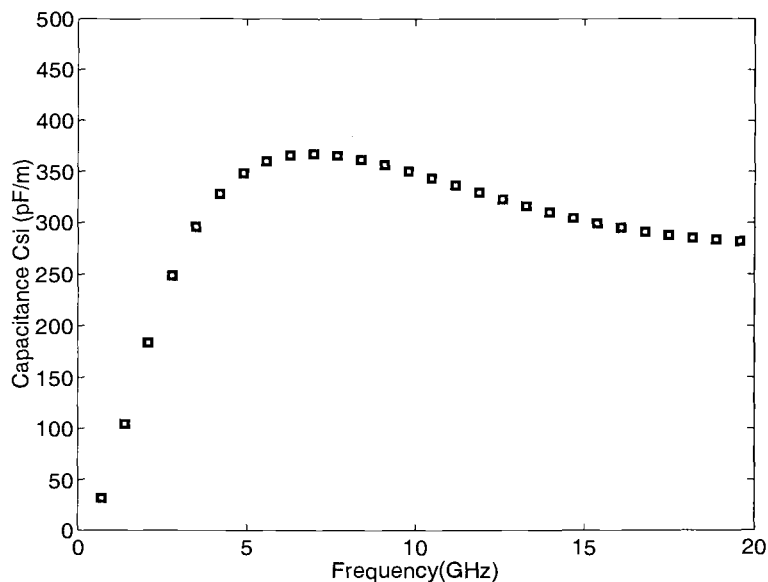


Figure 4.7. Capacitance C_{si} for a single MIS line for the substrate conductivity of $\sigma = 10(S/m)$.

tal quasi-TEM modes of propagation. The even mode is the mode corresponding to both microstrip conductors being at the same potential V and having equal currents. The odd mode corresponds to the microstrip conductors being at opposite potentials, $-V$ and V , with respect to the ground plane. For the odd mode the currents on the two conductors are also equal in amplitude but of opposite direction.

The important parameters describing the quasi-TEM mode properties of the coupled microstrip line are the even- and odd-mode effective dielectric constants, and the even- and odd-mode characteristic impedances. The line parameters such as effective dielectric constants, ϵ_{effe} and ϵ_{effo} , characteristic impedances, $Z_e(\omega)$ and $Z_o(\omega)$ and propagation constants, $\gamma_e(\omega)$ and $\gamma_o(\omega)$ are calculated using the even- and odd-mode approach for symmetric coupled line.

Theoretically, the effective dielectric constant for the odd mode is smaller

than that for the even mode because a larger percentage of the electric field energy is located in the air region. The capacitance between closely spaced parallel signal conductors at opposite potentials is large, so that the characteristic impedance of the odd mode is smaller than that for the even mode. The attenuation constant for symmetric coupled microstrip lines is comparable to that for the microstrip line. For closely spaced conductors the increased concentration of the current near the two inner edges for the odd mode, along with the smaller characteristic impedance, increases the attenuation constant of this mode relative to that for the even mode. For the odd mode the attenuation caused by dielectric loss will be less than that for the even mode since the electric field energy is more evenly distributed between the air region and the substrate region for this mode.

Following equations (4.1) and (4.2), the even- and odd-mode parameters $L_e(\omega)$, $G_e(\omega)$ and $C_e(\omega)$ and $L_o(\omega)$, $G_o(\omega)$ and $C_o(\omega)$ for the symmetric coupled MIS structure can easily be calculated.

As an example of a symmetric coupled line MIS structure, the conductor lines are simulated on an $N_x\Delta x$ by $N_y\Delta y$ by $N_z\Delta z$ computational domain with $\Delta x=10\mu\text{m}$, $\Delta y = 12.5\mu\text{m}$ and $\Delta z=20\mu\text{m}$. This corresponds to a conductor width of the signal lines of $W1 = W2 = 5\Delta x$, a gap between the two signal lines of $S = 5\Delta x$, and substrate heights of $H1 = 16\Delta y$ and $H2 = 2\Delta y$. The width, N_x , and height, N_y , of the simulation box are chosen to be large enough to not disturb the field distributions near the strips. The entire computational domain including the PML boundary of 8 cells is divided into 78 by 50 by 280 grid cells with the conductivity of silicon layer of $\sigma = 10(\text{siemens/m})$. The time step Δt , the input source, the pulse width and time delay are exactly the same as for the single line case.

Figures 4.8 to 4.10 show the results of the symmetric coupled line MIS structure for $\sigma = 10$ (siemens/m) of the silicon layer. Figure 4.8 shows the frequency-dependent effective dielectric constant $\epsilon_{eff}(\omega)$ and characteristic impedance $Z_o(\omega)$

for the even- and odd-mode. The total inductance, conductance, capacitance and attenuation constant are shown in Figures 4.9 and 4.10, respectively. It can be seen that as expected, the even mode attenuation is significantly higher than that for the odd mode due to the stronger field concentration in the substrate for the even mode. It can be seen that, in general, the even mode exhibits stronger frequency dependence.

4.4 SINGLE MIS LINE WITH SUBSTRATE SHIELDING

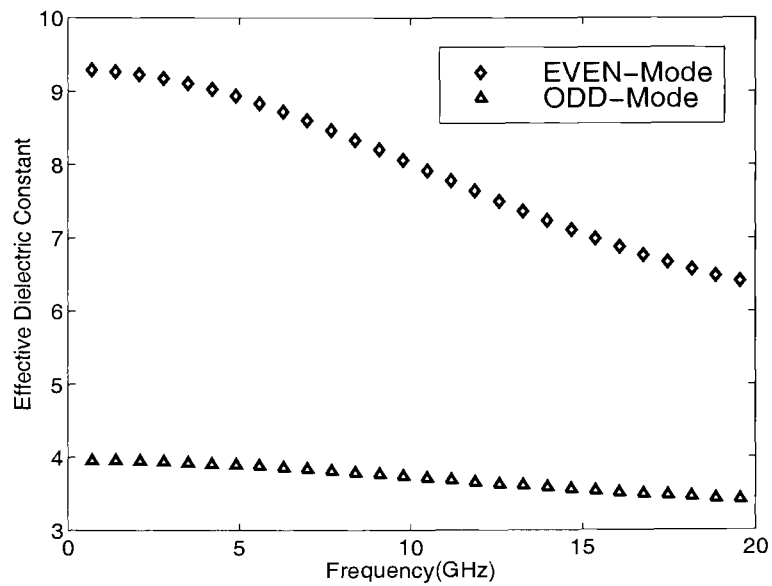
A single line MIS structure with an embedded grounded cross bar structure for substrate shielding is shown in Figure 4.11. The width and spacing of the cross bars are considered to be much smaller than the wavelength so that uniform signal propagation can be assumed along the line.

As in the case without substrate shielding, the characteristic impedance $Z_o(\omega)$ and the propagation constant $\gamma(\omega)$ of the signal line are obtained from the ratio of Fourier-transformed voltage and current and the ratio of the voltages taken at two different locations, respectively.

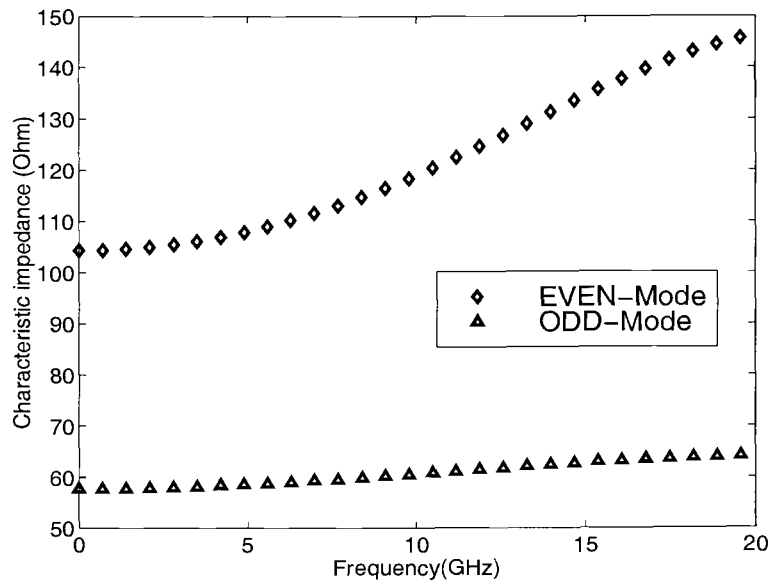
In the FDTD method, the entire computational domain is discretized into a number of cells of size Δx , Δy and Δz in x , y and z directions, respectively. Figure 4.12 shows the total computational domain of the proposed cross bar structure including the Perfectly Matched Layer (PML) absorbing boundary condition.

During the FDTD simulation, the potential is set to be zero for the grid cells containing the cross bar conductors so that all cross bars behave like perfect grounded conductors. The input port of the signal line is excited with a Gaussian pulse and the voltages and currents are recorded at two different locations. The characteristic impedance of the structure is obtained from the ratio of Fourier-transformed voltage and current.

The metal strips and the ground plane are assumed to be perfectly conducting and infinitely thin, and are defined by setting the tangential component of the

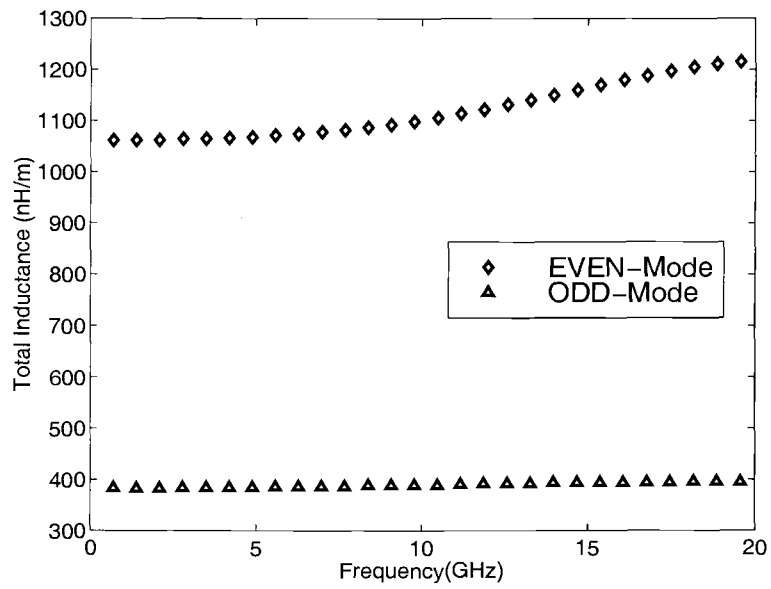


(a)

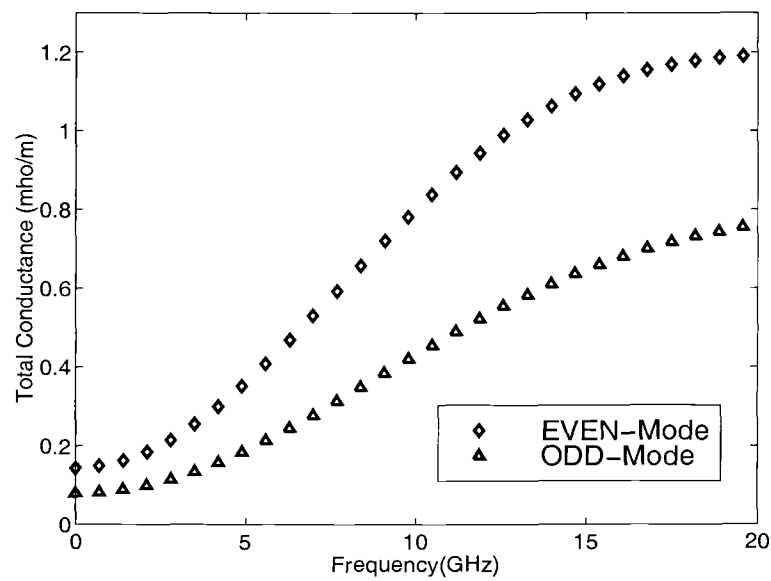


(b)

Figure 4.8. (a) Effective dielectric constant and (b) characteristic impedance for the symmetric coupled MIS structure.

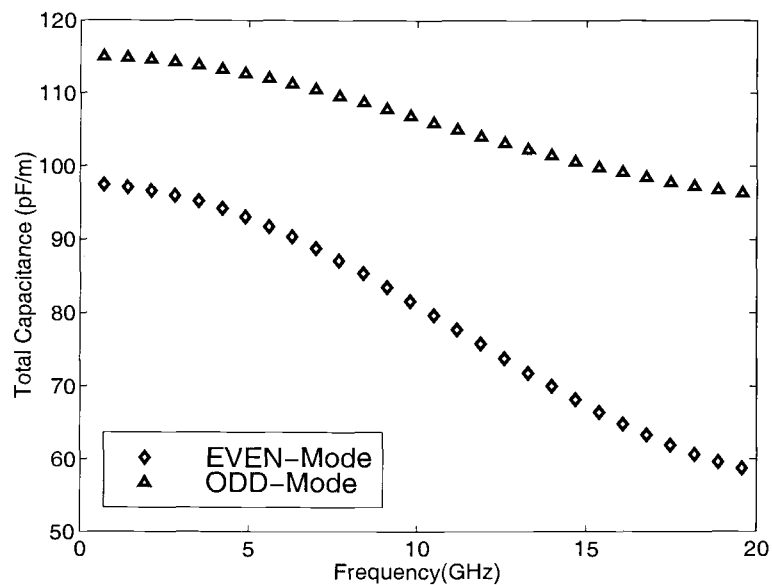


(a)

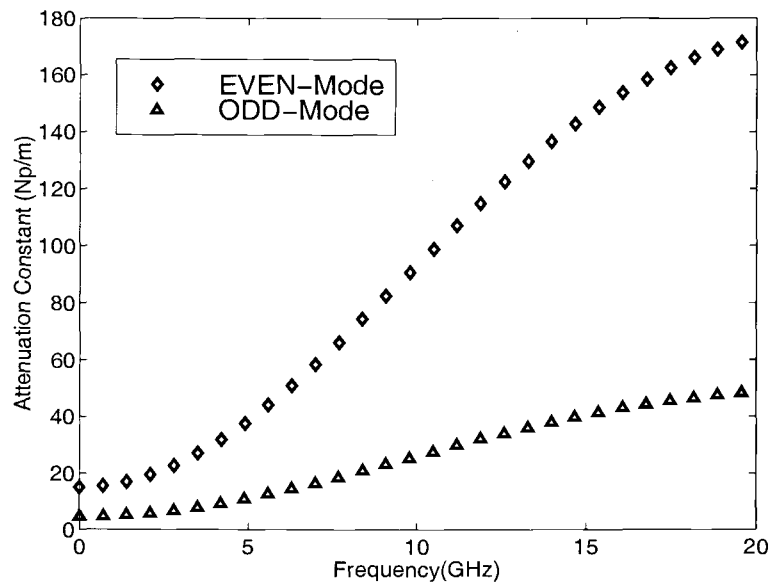


(b)

Figure 4.9. (a) Total inductance and (b) conductance for the symmetric coupled MIS structure.



(a)



(b)

Figure 4.10. (a) Total capacitance and (b) attenuation constant for the symmetric coupled MIS structure.

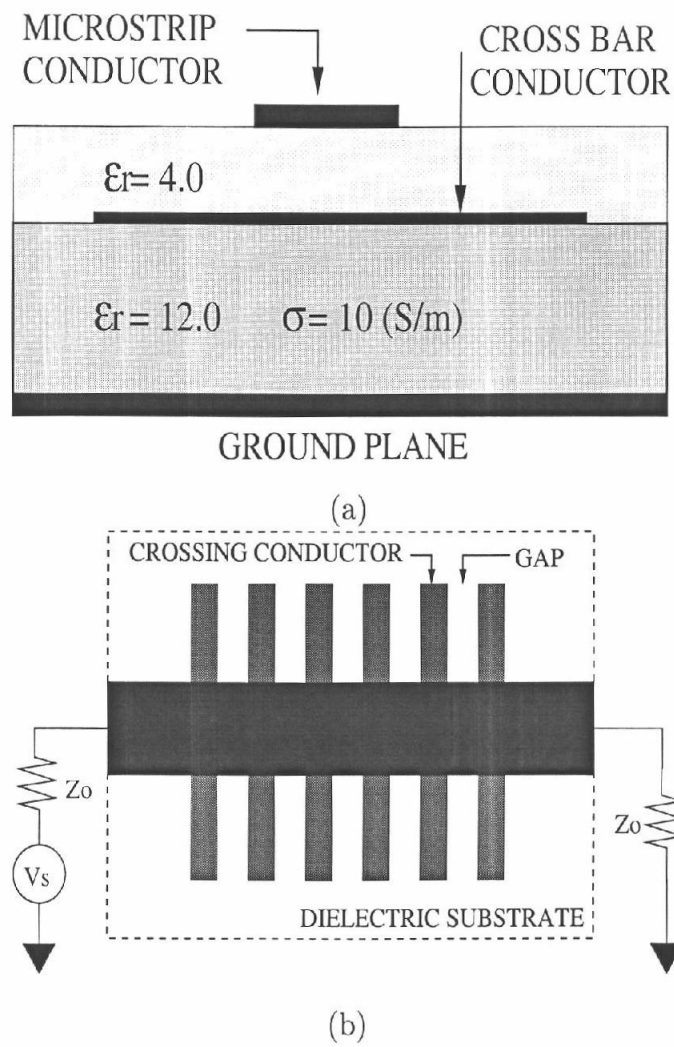


Figure 4.11. (a) Side view and (b) top view of single microstrip MIS structure with embedded grounded cross bars for substrate shielding.

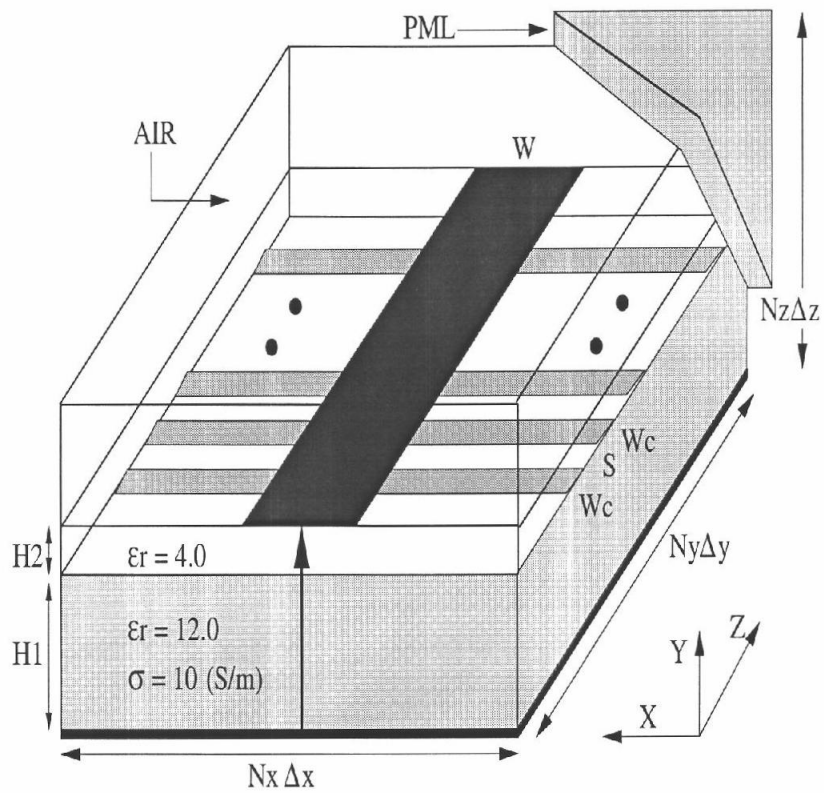


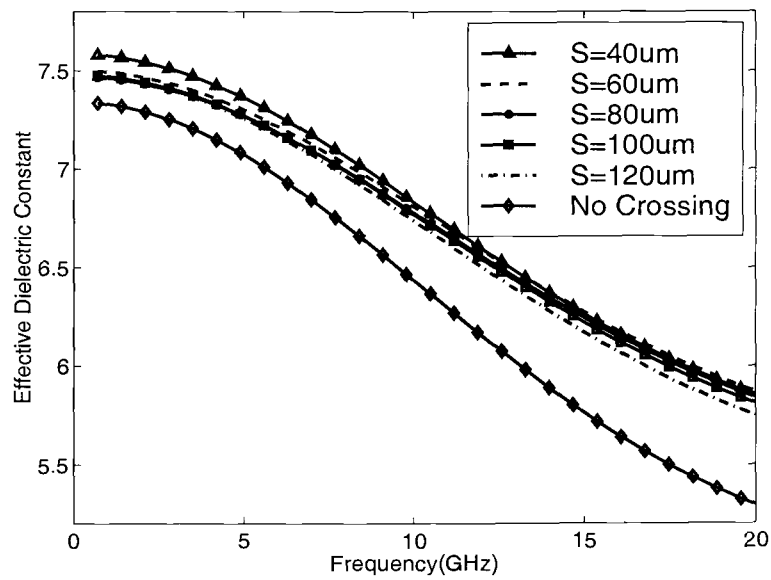
Figure 4.12. Computational domain for FDTD simulation of a single MIS line with a cross bar substrate shielding structure.

electric field to zero. The conductor lines are simulated on an $N_x\Delta x$ by $N_y\Delta y$ by $N_z\Delta z$ computational domain with $\Delta x = 10\mu\text{m}$, $\Delta y = 12.5\mu\text{m}$ and $\Delta z = 20\mu\text{m}$. This corresponds to conductor width $W = 5\Delta x$ of the signal line, a cross bar conductor width of $W_c = 2\Delta z$, a gap size between the cross bars of $S = 2\Delta z$, $3\Delta z$, $4\Delta z$, $5\Delta z$, and $6\Delta z$ respectively, and substrate heights $H1 = 16\Delta y$ and $H2 = 2\Delta y$. The width, N_x , and height, N_y , of the simulation box are chosen to be large enough to not disturb the field distributions near the strips. The entire computational domain including the PML boundary of 8 cells is divided into 58 by 50 by 280 grid cells.

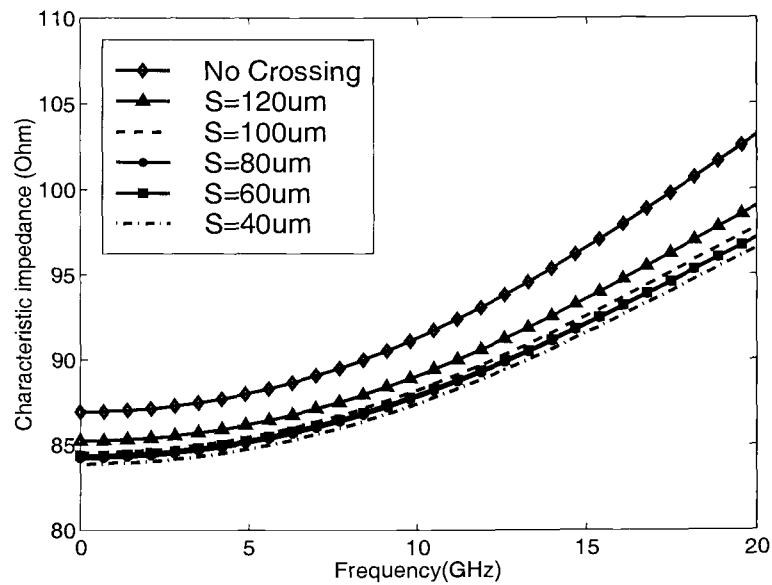
A time step of $\Delta t = 0.0218$ ps is used and the total number of time steps is 2500. The input is excited with a Gaussian pulse with $T = 2.33$ ps and $t_o = 6.98$ ps. Figures 4.13 to 4.16 show the results of the MIS line with the cross bar structure for different spacing of the cross bar conductors for substrate conductivity $\sigma = 10$ (siemens/m).

Figure 4.13 shows the frequency-dependent effective dielectric constant $\epsilon_{eff}(\omega)$ and characteristic impedance $Z_o(\omega)$ for various gap sizes between the cross bars as well as without cross bars. It can be seen that the effective dielectric constant and characteristic impedance are changed only slightly by the presence of the cross bar structure. The overall inductance, conductance, capacitance and attenuation constant are shown in Figures 4.14 and 4.15, respectively. It is observed that the overall conductance $G(\omega)$ is reduced with the introduction of the cross bar conductors, and the smallest conductance is achieved for the smallest gap size ($S = 40\mu\text{m}$).

Figure 4.16(a) shows the quality factor $Q = \beta/2\alpha$ as a function of frequency and Figure 4.16(b) gives a variation in Q as a function of normalized spacing (cross bar width/spacing) for different frequencies. It is observed that the quality factor Q improves for decreasing cross bar spacing and that the improvement is more pronounced at lower frequencies.

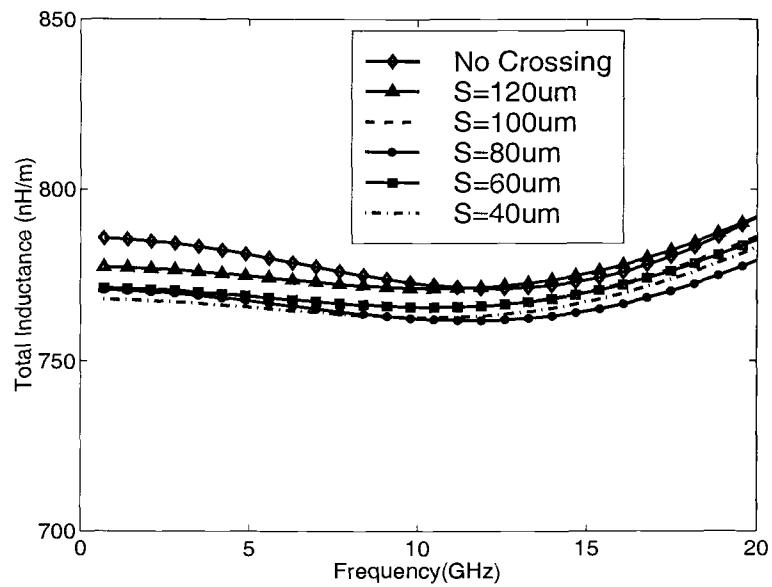


(a)

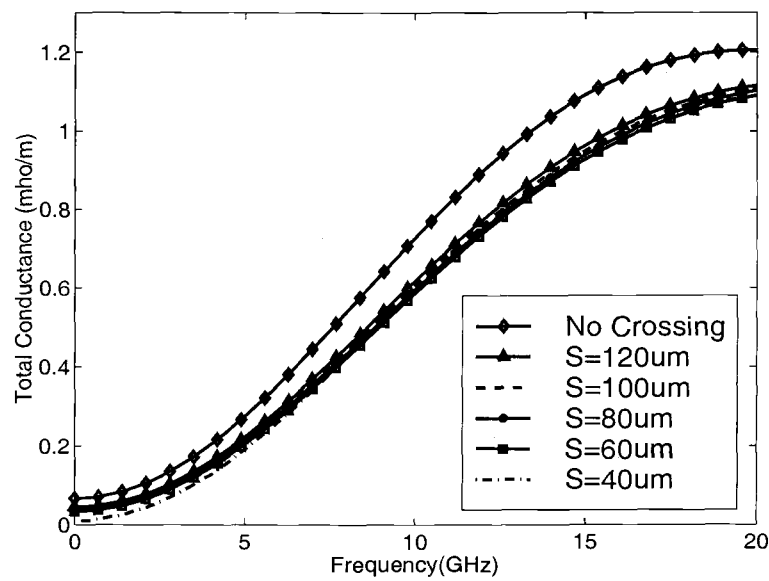


(b)

Figure 4.13. (a) Effective dielectric constant and (b) characteristic impedance for $\sigma = 10(\text{S/m})$.

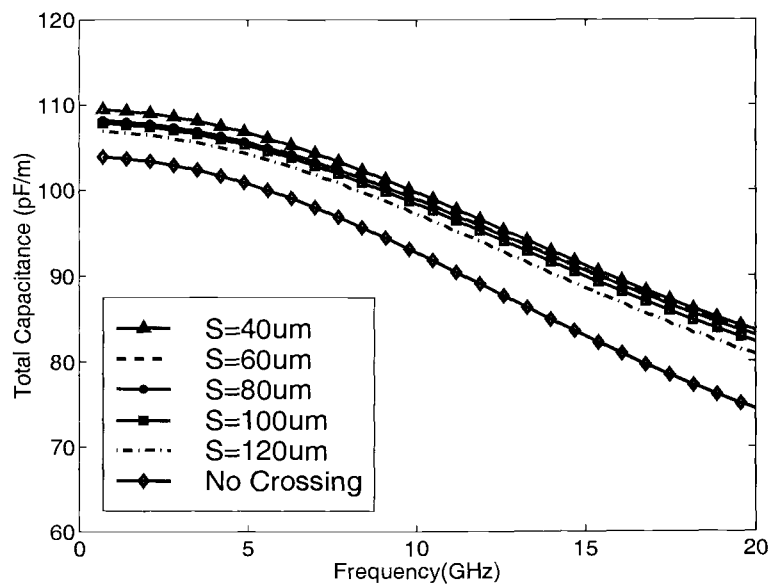


(a)

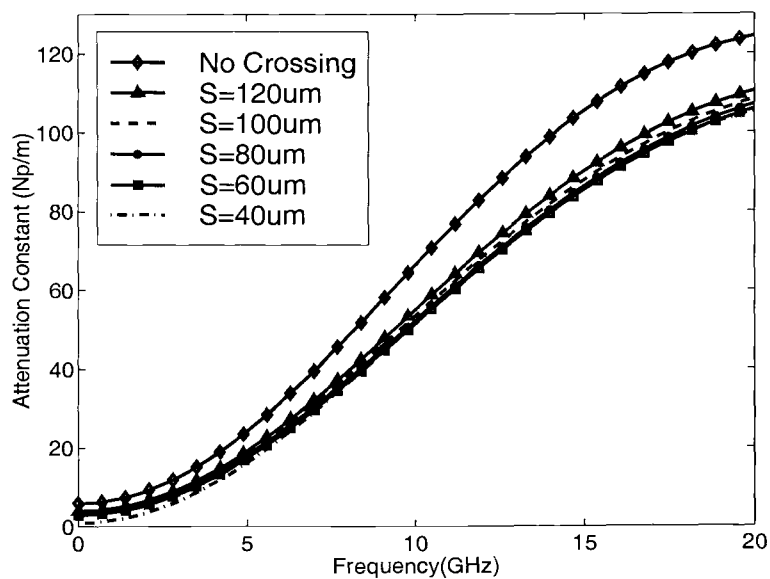


(b)

Figure 4.14. (a) Total inductance and (b) conductance for $\sigma = 10(\text{S/m})$.

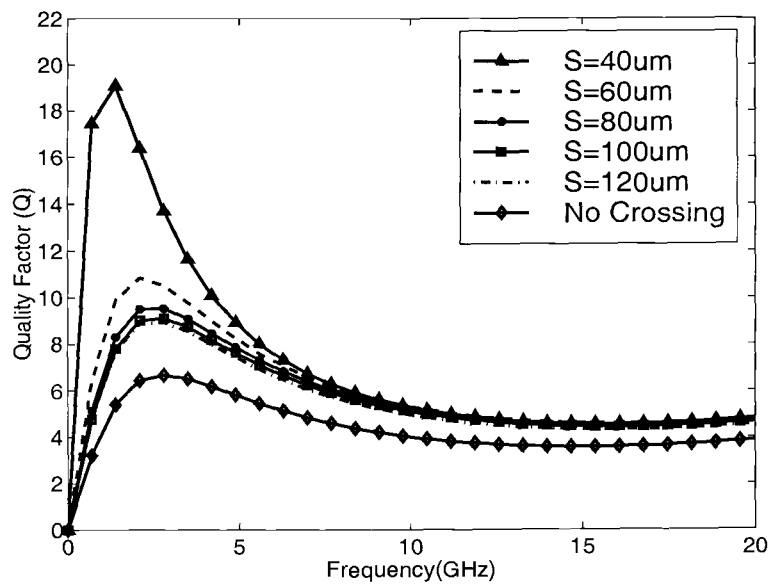


(a)

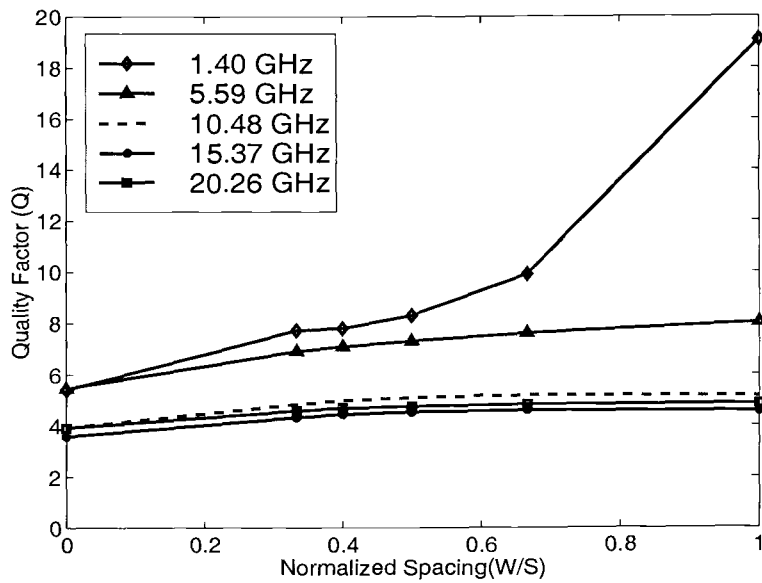


(b)

Figure 4.15. (a) Total capacitance and (b) attenuation constant for $\sigma = 10(\text{S/m})$.



(a)



(b)

Figure 4.16. (a) Quality factor(Q) as a function of frequency and (b) Quality factor(Q) with the normalized spacing for $\sigma = 10$ siemens/meter.

4.5 SYMMETRIC COUPLED MIS LINES WITH SUBSTRATE SHIELDING

Figure 4.17 shows a symmetric coupled line MIS structure with embedded grounded cross bars for substrate shielding. The conductor lines are simulated on an $N_x\Delta x$ by $N_y\Delta y$ by $N_z\Delta z$ computational domain with $\Delta x = 10\mu\text{m}$, $\Delta y = 12.5\mu\text{m}$ and $\Delta z = 20\mu\text{m}$. This corresponds to conductor widths $W1 = W2 = 5\Delta x$ for the signal lines, a gap size between the two signal lines of $S = 5\Delta x$, a cross bar conductor width of $W_c = \Delta z$, and spacings $S = 3\Delta z$ and $6\Delta z$ between the cross bars, respectively. The substrate heights are $H1 = 16\Delta y$ and $H2 = 2\Delta y$. The entire computational domain including the PML boundary of 8 cells is divided into 78 by 50 by 280 grid cells. In the FDTD simulation, the time step Δt , the input source, the pulse width and the time delay are taken the same as for the single line case.

Figures 4.18 to 4.20 show the results for the symmetric coupled lines with the embedded grounded cross bar structure for different spacings of the cross bar conductors and for substrate conductivity $\sigma = 10$ (siemens/m). Figure 4.18 shows the frequency-dependent effective dielectric constant $\epsilon_{eff}(\omega)$ and characteristic impedance $Z_o(\omega)$ for the even- and odd-modes. The overall inductance, conductance, capacitance and attenuation constant are shown in Figures 4.18 and 4.20, respectively. It can be seen that as in the single line case, the cross bar shielding structure significantly reduces the shunt conductance and attenuation without significantly affecting the characteristic impedance.

4.6 CONCLUDING REMARKS

In this chapter, the Finite Difference Time Domain (FDTD) method has been applied to compute the propagation constants and characteristic impedances of Si-based multilayer single and symmetric coupled line MIS structures. The results

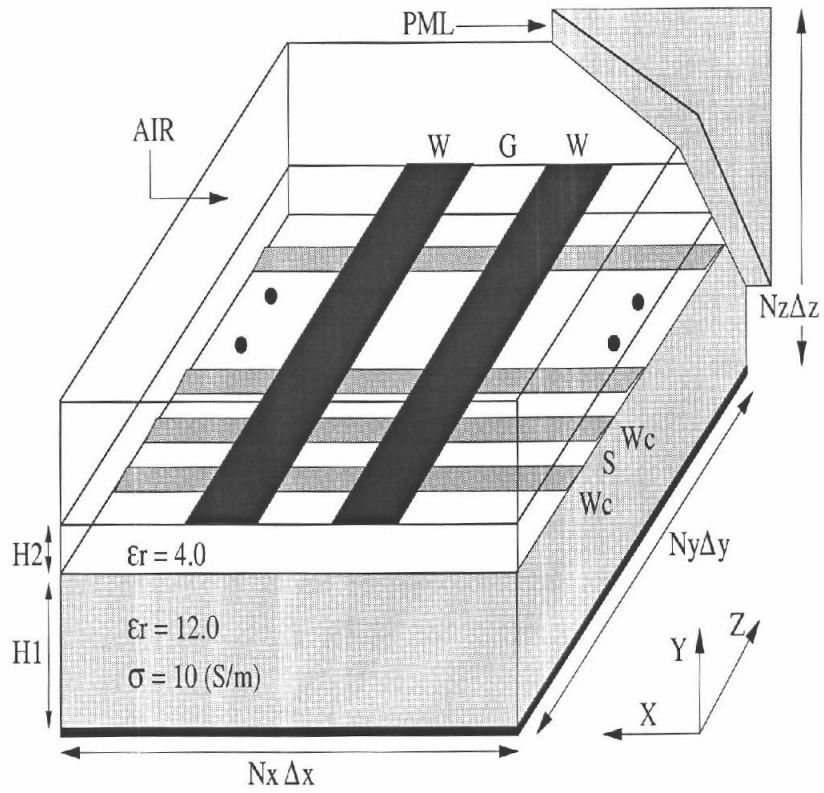
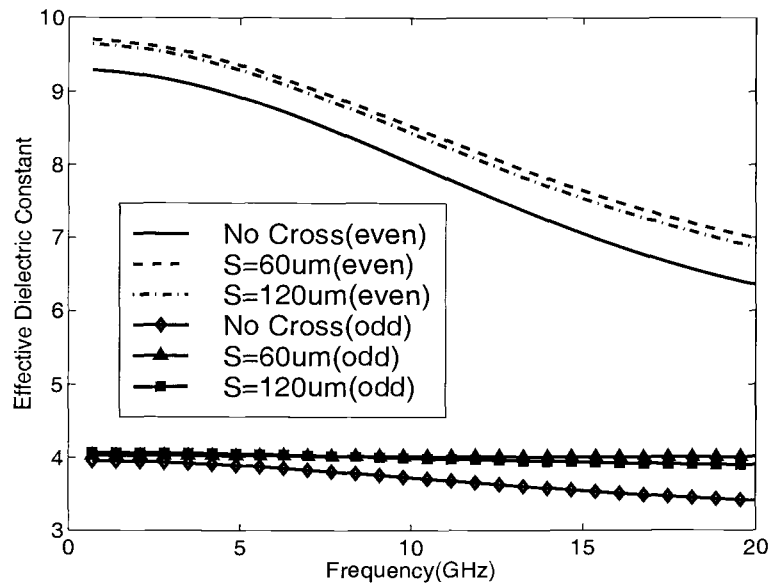
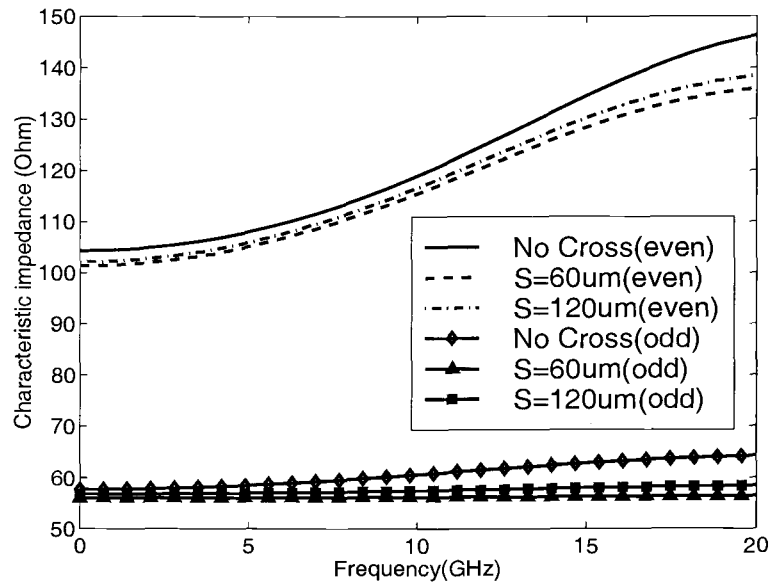


Figure 4.17. Computational domain in FDTD simulation of symmetric coupled lines with the cross bar shielding structure.

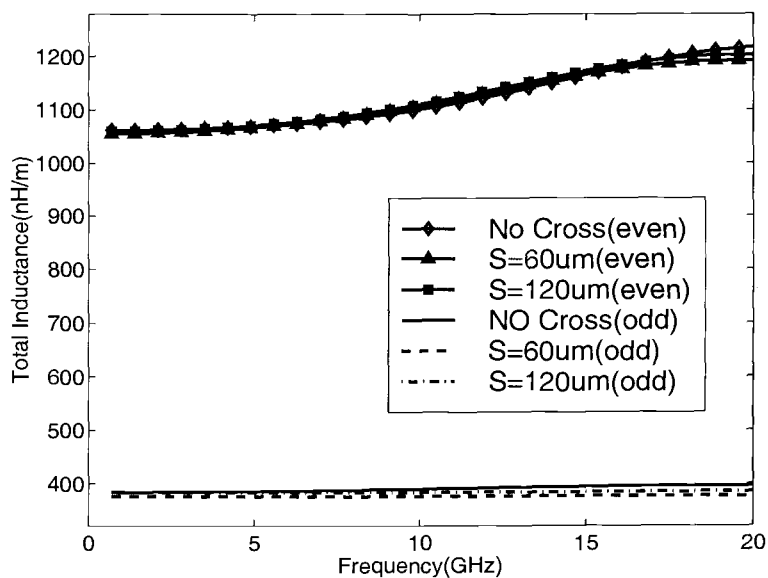


(a)

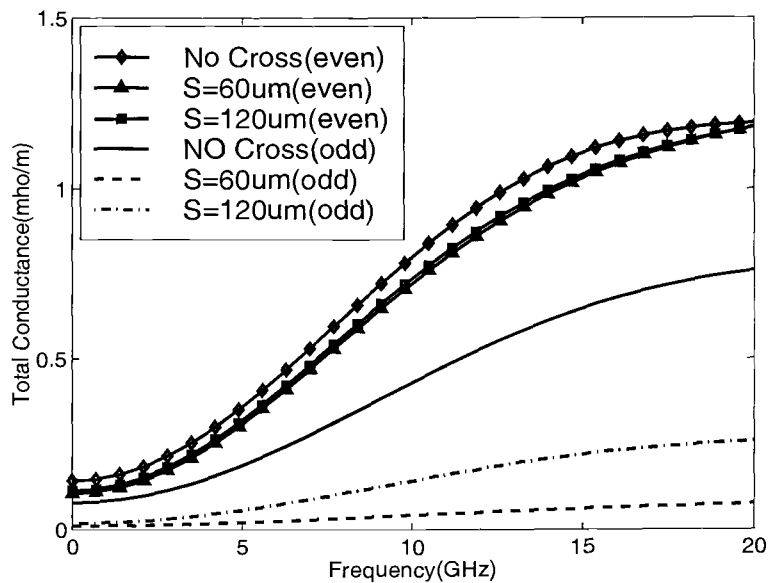


(b)

Figure 4.18. (a) Effective dielectric constant and (b) Characteristic impedance for symmetric coupled lines with $\sigma = 10(\text{S/m})$.

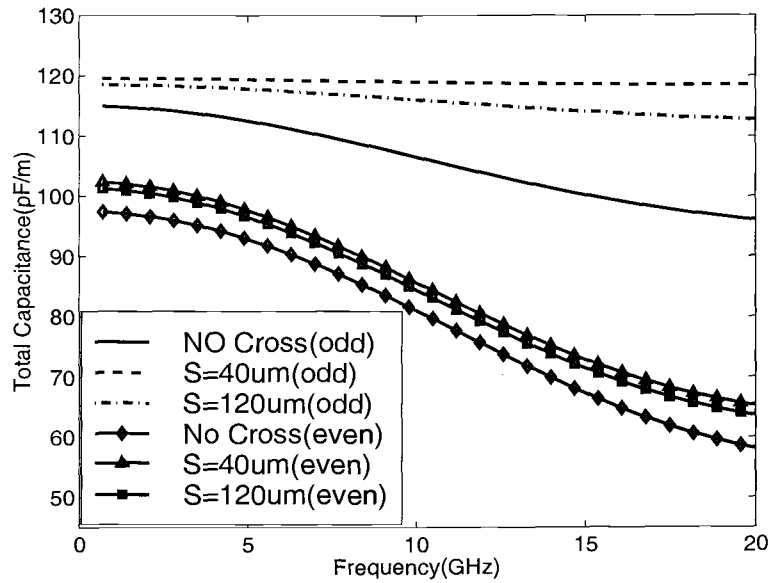


(a)

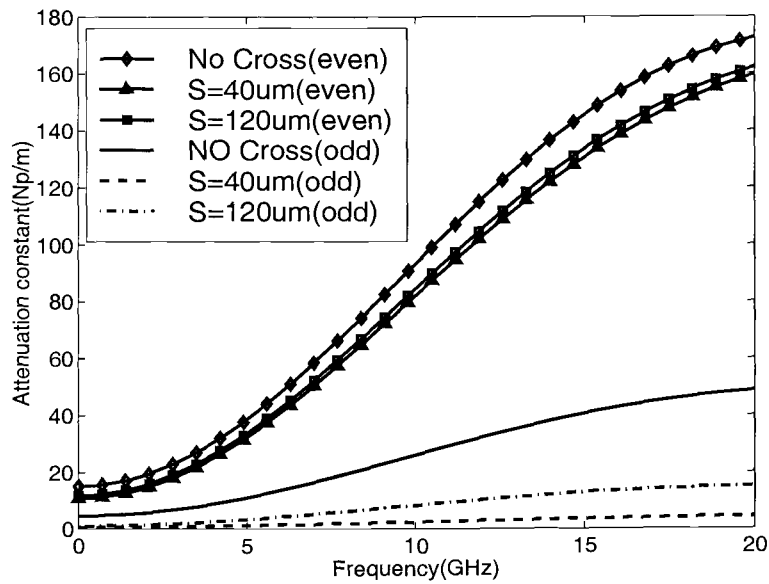


(b)

Figure 4.19. (a) Even- and odd-mode inductance and (b) conductance for a symmetric coupled line structure with substrate conductivity $\sigma=10(\text{S/m})$.



(a)



(b)

Figure 4.20. (a) Even- and odd-mode capacitance and (b) attenuation constant for symmetric coupled line structure with substrate conductivity $\sigma=10(\text{S/m})$.

show that the transmission line characteristics are strongly influenced by the lossy nature of the silicon substrate.

In order to reduce the substrate effects on the transmission line characteristics, a shielding structure consisting of grounded cross bar conductor lines has been examined. The extracted distributed transmission line parameters and corresponding equivalent circuit parameters as well as quality factor have been examined as a function of spacing of the crossbar lines. It was found that the quality factor of the transmission lines can be improved without significant change in the characteristic impedance and effective dielectric constant.

Chapter 5

MICROSTRIP DISCONTINUITIES

5.1 INTRODUCTION

Figure 5.1 shows typical microstrip discontinuities such as bends, step-in width, and T-junctions that are basic components of RF/microwave integrated circuits. Accurate frequency-dependent characterization of the reflection and transmission properties of these discontinuities is of great importance and is a continuing area of interest in microwave computer-aided design (CAD). Discontinuity problems in microstrip lines have been studied for many years, where discontinuities typically were analyzed using quasi-static or approximate full-wave techniques [89], [90], [91], [92], [93], [94], [95].

More recently, a number of full-wave techniques have been presented for the analysis of microstrip discontinuities including the open-end and gap [96], [97], and step-in-width [98]. In [96] and [97] finite element currents were used to model the open-end and gap discontinuities. In 1989, Jackson [99] presented the full-wave characteristics for different types of discontinuities such as single stub and bent stub using finite element expansion currents (rooftop functions) and sinusoidal precomputed expansion currents for input and output microstrip lines. All the above-mentioned investigations, however, were done in the frequency-domain, that is, a new simulation was performed for each frequency point. For broadband characterization of discontinuities, many frequency points and, hence, many simulations may be needed.

In 1988, Zhang and Mei have first used the FDTD technique to analyze several types of microstrip discontinuities including T-junction and cross-junction

[18]. Sheen et al. applied the FDTD technique to characterize microstrip low pass filters and branch line couplers [19]. The characterization of 90 degree bends with arbitrary miter and harmonical characterization of microstrip bends using FDTD was proposed by Moore [21] and Feix [22], respectively. As an alternative to computational techniques, the characterization of microstrip discontinuities from time-domain measurements was reported in [100], [101], [102].

In this chapter, the FDTD method is applied to determine the broadband characteristics for several types of single microstrip discontinuities such as open-end, asymmetric gap, step-in-width, as well as a symmetric cross-junction. The modeling approach is then extended to characterize coupled line discontinuities, such asymmetric coupled gaps and asymmetric coupled steps by using a new extraction procedure. Results for several discontinuity structures are presented.

5.2 NETWORK FORMULATION FOR DISCONTINUITIES

Discontinuities can be conveniently characterized in terms of the scattering parameters. For a general n -port network with different characteristic impedances, as illustrated in Figure 5.2, the scattering parameters are defined as

$$\begin{bmatrix} b_1 \\ b_2 \\ \cdot \\ \cdot \\ b_n \end{bmatrix} = \begin{bmatrix} S_{11} & S_{12} & \cdot & \cdot & S_{1n} \\ S_{21} & S_{22} & \cdot & \cdot & S_{2n} \\ \cdot & \cdot & \cdot & \cdot & \cdot \\ \cdot & \cdot & \cdot & \cdot & \cdot \\ S_{n1} & S_{n2} & \cdot & \cdot & S_{nn} \end{bmatrix} \begin{bmatrix} a_1 \\ a_2 \\ \cdot \\ \cdot \\ a_n \end{bmatrix} \quad (5.1)$$

where a_n and b_n are the normalized incident and reflected wave amplitudes at port n . The normalized wave amplitudes are related to voltages of the incident and reflected waves as

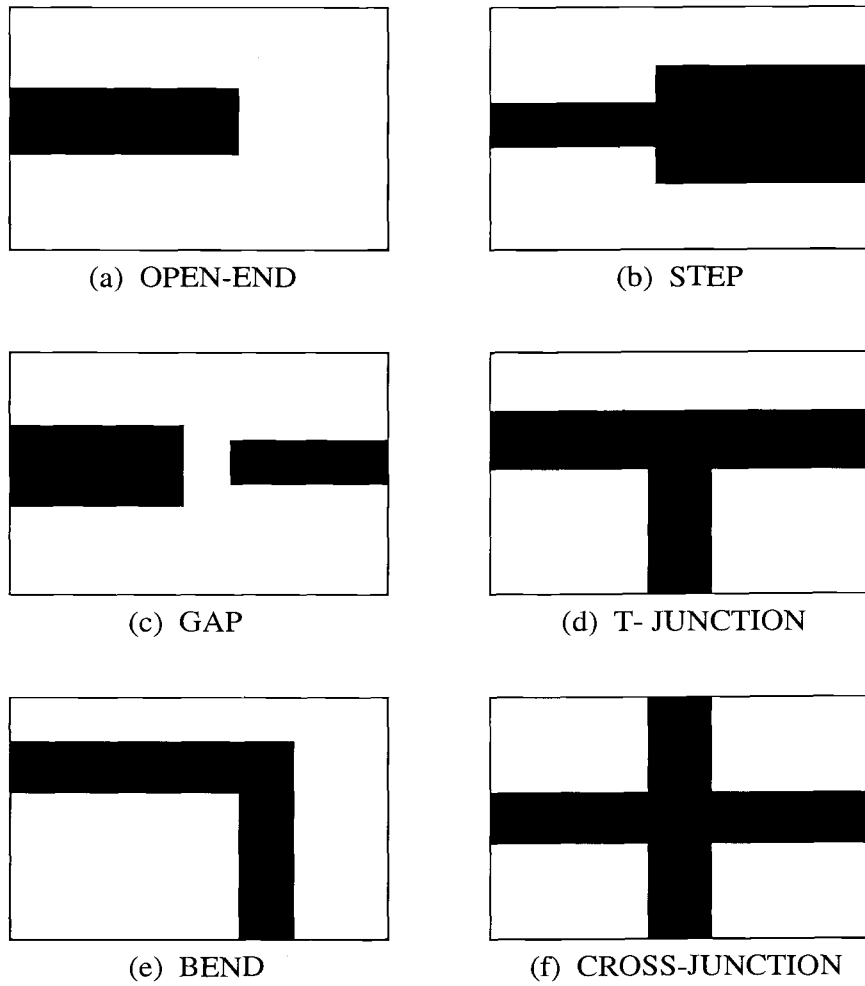


Figure 5.1. Various kinds of single microstrip discontinuities.

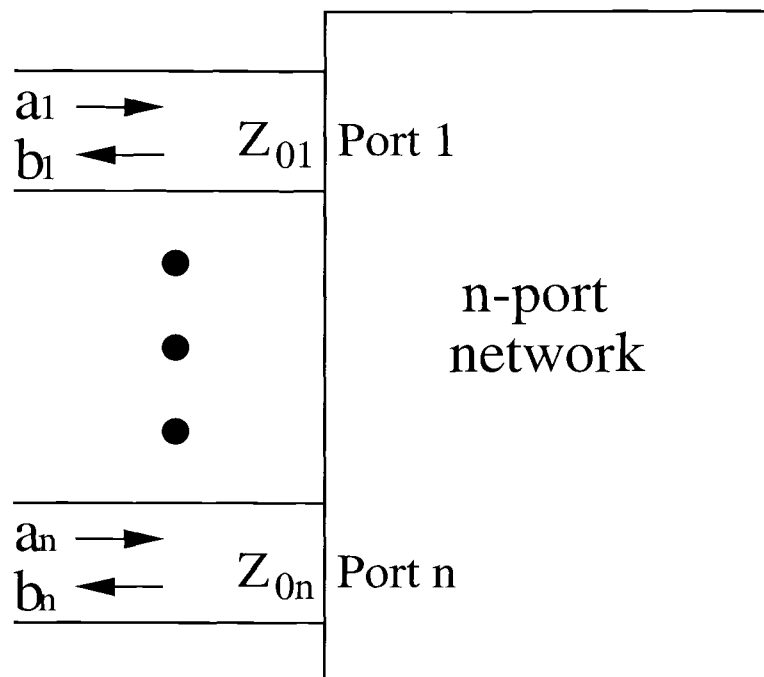


Figure 5.2. n-port network with different characteristic impedances.

$$\begin{bmatrix} a_1 \\ a_2 \\ \cdot \\ a_n \end{bmatrix} = \begin{bmatrix} \frac{1}{\sqrt{Z_{o1}}} & 0 & \cdot & 0 \\ 0 & \frac{1}{\sqrt{Z_{o2}}} & \cdot & 0 \\ \cdot & \cdot & \cdot & \cdot \\ 0 & 0 & \cdot & \frac{1}{\sqrt{Z_{on}}} \end{bmatrix} \begin{bmatrix} V_{i1} & 0 & \cdot & 0 \\ 0 & V_{i2} & \cdot & 0 \\ \cdot & \cdot & \cdot & \cdot \\ 0 & 0 & \cdot & V_{in} \end{bmatrix} \quad (5.2)$$

$$\begin{bmatrix} b_1 \\ b_2 \\ \cdot \\ b_n \end{bmatrix} = \begin{bmatrix} \frac{1}{\sqrt{Z_{o1}}} & 0 & \cdot & 0 \\ 0 & \frac{1}{\sqrt{Z_{o2}}} & \cdot & 0 \\ \cdot & \cdot & \cdot & \cdot \\ 0 & 0 & \cdot & \frac{1}{\sqrt{Z_{on}}} \end{bmatrix} \begin{bmatrix} V_{r1} & 0 & \cdot & 0 \\ 0 & V_{r2} & \cdot & 0 \\ \cdot & \cdot & \cdot & \cdot \\ 0 & 0 & \cdot & V_{rn} \end{bmatrix} \quad (5.3)$$

5.3 SINGLE LINE DISCONTINUITIES

5.3.1 MICROSTRIP OPEN-END DISCONTINUITY

The microstrip open-end discontinuity already has been analyzed using the FDTD method by Zhang and Mei [18]. Here Zhang's specification for the open-end structure is adopted to validate the FDTD method. A uniform line of the same width is used as reference to extract the voltage of the incident wave and then the voltage of the reflected wave for the discontinuity. The open-ended line and reference line shown in Figure 5.3 are discretized into a number of cells of size Δx , Δy , and Δz in x , y and z direction, respectively. The dielectric constant of the substrate is $\epsilon_r = 9.6$, the conductor width is $W = 600\mu\text{m}$ and the substrate height $H = 600\mu\text{m}$. The metal conductor and ground plane are assumed to be perfectly conducting and infinitely thin. The grid cell size is $\Delta x = \Delta y = \Delta z = 60\mu\text{m}$ and the time increment is $\Delta t = 0.104$ ps. The time delay and pulse width of the excitation source are $t_o = 33.28$ ps and $T = 11.09$ ps, respectively. The total number iteration time steps in the simulation is 1500.

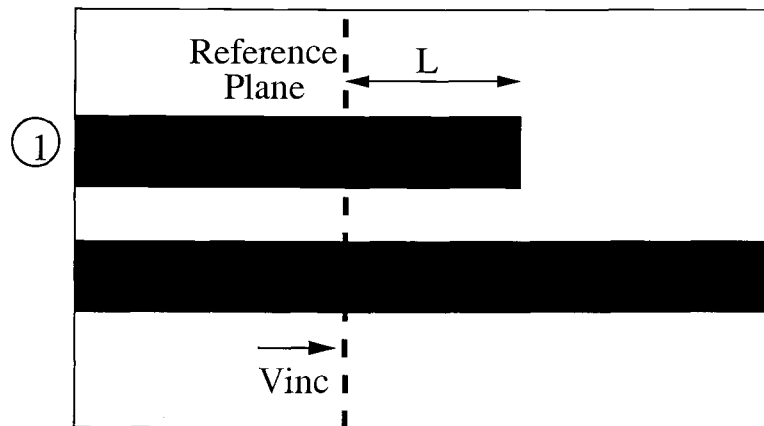
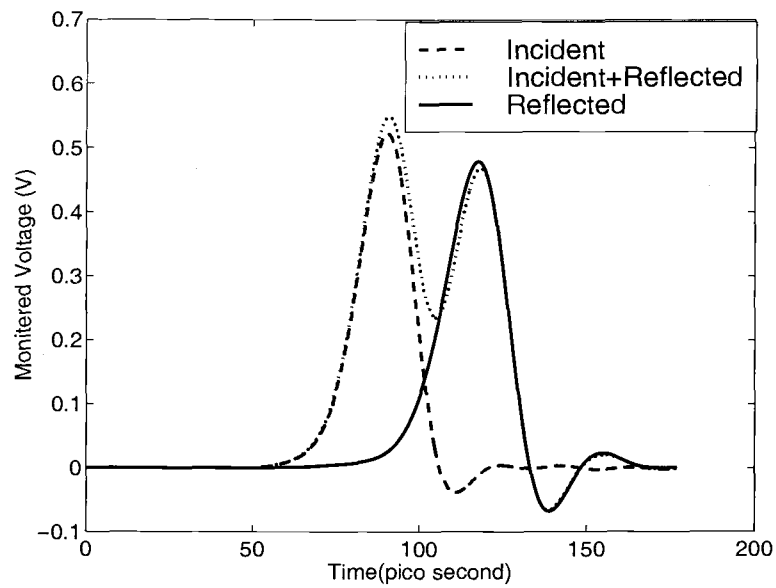


Figure 5.3. Single open-end structure with uniform reference line.

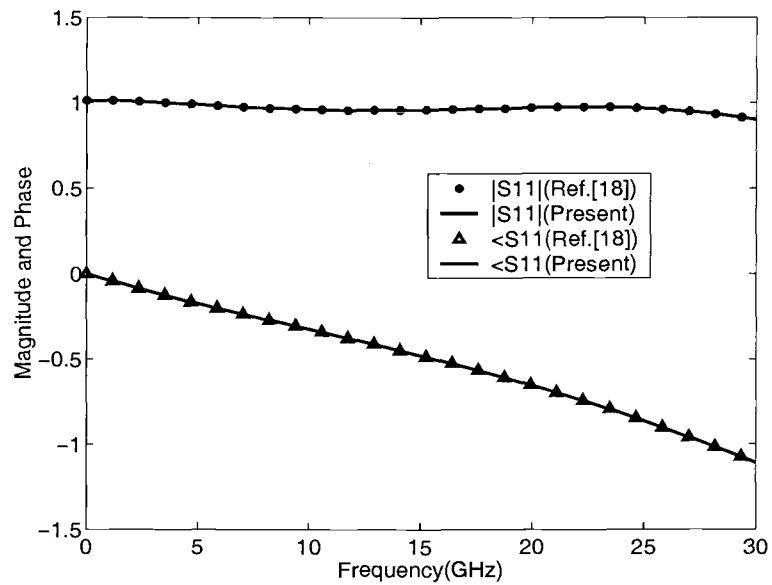
The microstrip open-end structure is a one-port network so that its scattering parameter has only one element, that is, S_{11} which is defined as

$$S_{11}(\omega) = \frac{V_r(\omega) \cdot \exp(\gamma(\omega)L)}{V_i(\omega) \cdot \exp(-\gamma(\omega)L)} \quad (5.4)$$

Here $V_r(\omega)$ is the Fourier-transformed reflection voltage at the reference plane and $V_i(\omega)$ is the Fourier-transformed incident voltage at the same reference location at distance L from the open end. The incident wave is obtained at the same reference location on an infinitely long line shown in Figure 5.3 and the reflected wave is obtained from the difference between the total monitored voltage wave and the incident wave at the same reference positions. Figure 5.4(a) shows the monitored incident and total voltage waveform, as well as the derived reflected waveform. The extracted scattering parameter $S_{11}(\omega)$ for the single open-end structure is shown in Figure 5.4(b) and compared to [18].



(a)



(b)

Figure 5.4. (a) Monitored voltage waveform and (b) scattering parameter for open-end structure.

5.3.2 MICROSTRIP STEP-IN-WIDTH

An abrupt change in microstrip line width, commonly named microstrip step-in-width, is a discontinuity frequently appearing in microwave integrated circuits such as low-pass filters, stepped impedance transformers and impedance matching networks [98]. A typical step discontinuity in a microstrip with widths $W1$ and $W2$, together with a uniform reference line, is shown in Figure 5.5(b). The specifications of the example structure are exactly the same as for the open-end structure except that the second width is $W2 = 300\mu\text{m}$.

Two orthogonal excitations are needed at port 1 and port 2, respectively, to calculate the two-port scattering parameters. The two-port scattering parameters of the step discontinuity (Figure 5.5(a)) is found from

$$\begin{bmatrix} a_1 \\ a_2 \end{bmatrix} = \begin{bmatrix} \frac{1}{\sqrt{Z_{o1}}} & 0 \\ 0 & \frac{1}{\sqrt{Z_{o2}}} \end{bmatrix} \cdot \begin{bmatrix} V_{i1} & 0 \\ 0 & V_{i2} \end{bmatrix} \quad (5.5)$$

$$\begin{bmatrix} b_1 \\ b_2 \end{bmatrix} = \begin{bmatrix} \frac{1}{\sqrt{Z_{o1}}} & 0 \\ 0 & \frac{1}{\sqrt{Z_{o2}}} \end{bmatrix} \cdot \begin{bmatrix} V_{r11} & V_{t12} \\ V_{t21} & V_{r22} \end{bmatrix} \quad (5.6)$$

$$S_{11}(\omega) = \frac{V_{r11}(\omega)}{V_{i1}(\omega)} \quad (5.7)$$

$$S_{21}(\omega) = \frac{\frac{V_{t21}(\omega)}{\sqrt{Z_{o2}(\omega)}}}{\frac{V_{i1}(\omega)}{\sqrt{Z_{o1}(\omega)}}} \quad (5.8)$$

$$S_{22}(\omega) = \frac{V_{r22}(\omega)}{V_{i2}(\omega)} \quad (5.9)$$

$$S_{12}(\omega) = S_{21}(\omega) \quad (5.10)$$

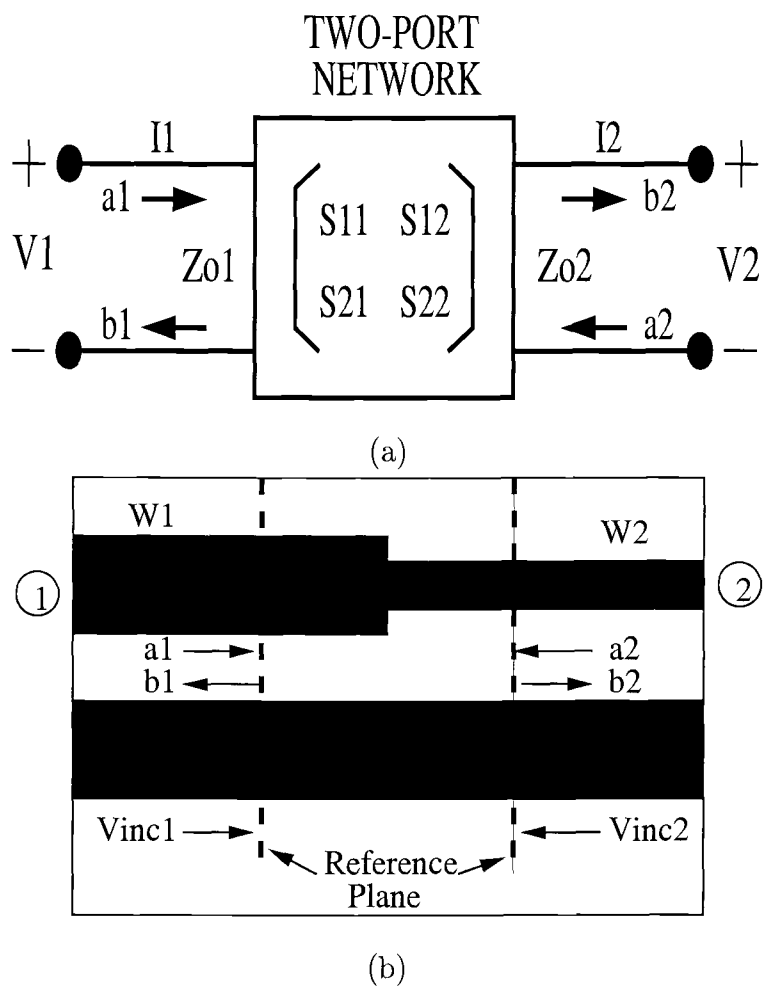


Figure 5.5. (a) Two-port network for scattering parameters and (b) single step-in-width structure.

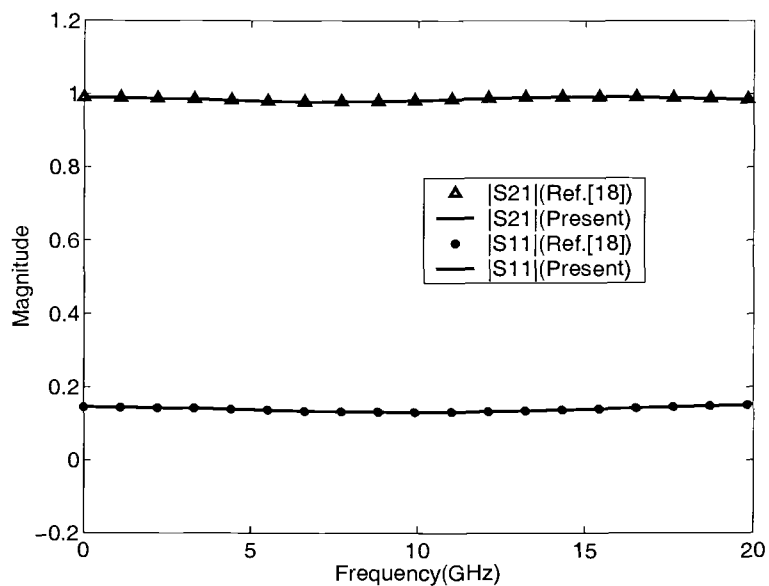
Here $Z_{o1}(\omega)$ and $Z_{o2}(\omega)$ are the characteristic impedances of the microstrip lines connected to port 1 and port 2, respectively. The voltages $V_{r11}(\omega)$ and $V_{r22}(\omega)$, $V_{i1}(\omega)$ and $V_{i2}(\omega)$, and $V_{t12}(\omega)$ and $V_{t21}(\omega)$ are the Fourier-transformed reflected, incident and transmitted voltages at ports 1 and 2, respectively. Here, V_{tjk} is the voltage of the wave transmitted to port j when port k is excited. Figure 5.6 shows the magnitude and phase of scattering parameters. Note that as expected $S_{21}(\omega) = S_{12}(\omega)$, and $S_{11}(\omega)$ and $S_{22}(\omega)$ are nearly identical in magnitude.

5.3.3 ASYMMETRIC MICROSTRIP GAP

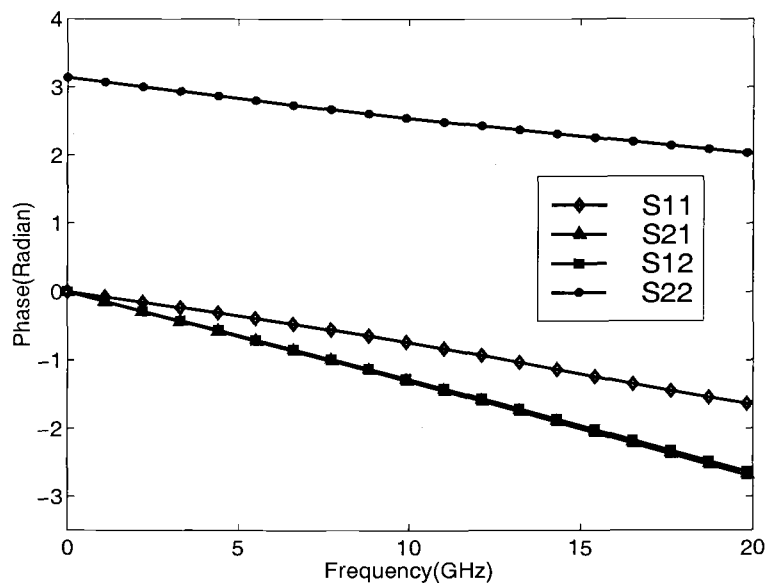
An asymmetric microstrip gap is shown in Figure 5.7. The structure specifications are conductor widths $W1 = 600\mu\text{m}$, $W2 = 300\mu\text{m}$, gap between the two conductors $G = 300\mu\text{m}$, substrate height $H = 600\mu\text{m}$, and dielectric constant $\epsilon_r = 9.6$. The computed scattering parameters are given in Figure 5.8.

5.3.4 MICROSTRIP CROSS-JUNCTION

In this section, the scattering parameters for four-port network shown in Figure 5.9 are found. A symmetric cross-junction structure is shown in Figure 5.10(a). For the FDTD simulation, the specifications of the structure are: dielectric constant of substrate $\epsilon_r = 9.8$, conductor width $W = 600\mu\text{m}$, and substrate height $H = 635\mu\text{m}$. Figures 5.10(b) and 5.11 show monitored voltages and the propagation waveform at 900 timesteps. The Gaussian pulse which travels into the cross-junction splits in four ways after reaching the cross-junction. It is seen from Figure 5.12(a) that at low frequencies, the scattering parameters correctly all have a magnitude of 0.5. This means that the power is equally divided between the four lines.



(a)



(b)

Figure 5.6. (a) Magnitude and (b) phase of scattering parameters for single step-in-width structure.

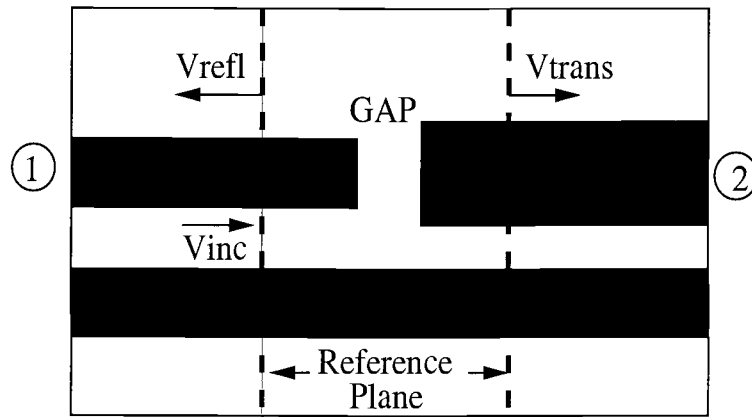


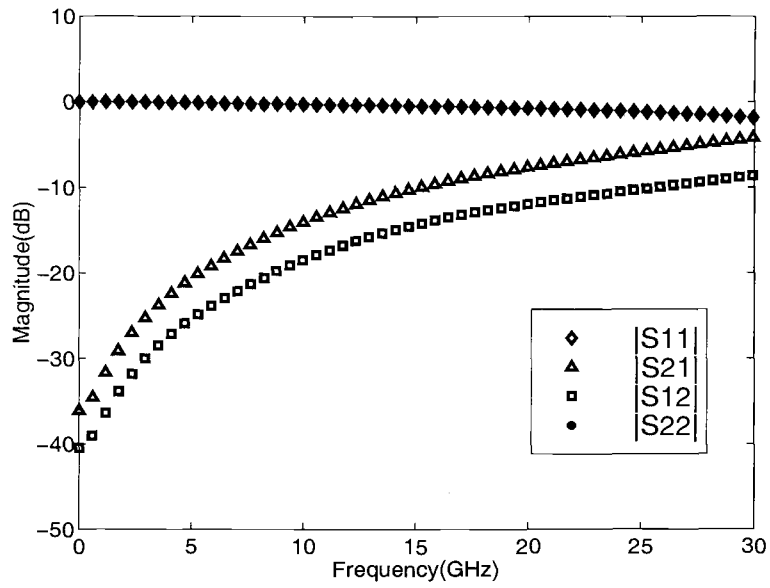
Figure 5.7. Asymmetric gap structure.

$$\begin{bmatrix} a1 \\ a2 \\ a3 \\ a4 \end{bmatrix} = \begin{bmatrix} \frac{1}{\sqrt{Z_{01}}} & 0 & 0 & 0 \\ 0 & \frac{1}{\sqrt{Z_{02}}} & 0 & 0 \\ 0 & 0 & \frac{1}{\sqrt{Z_{03}}} & 0 \\ 0 & 0 & 0 & \frac{1}{\sqrt{Z_{04}}} \end{bmatrix} \begin{bmatrix} V_{i1} & 0 & 0 & 0 \\ 0 & V_{i2} & 0 & 0 \\ 0 & 0 & V_{i3} & 0 \\ 0 & 0 & 0 & V_{i4} \end{bmatrix} \quad (5.11)$$

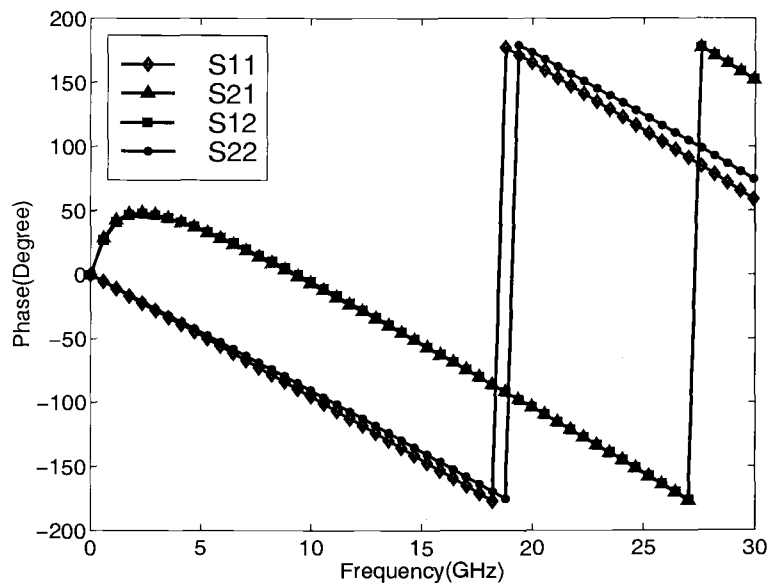
$$\begin{bmatrix} b1 \\ b2 \\ b3 \\ b4 \end{bmatrix} = \begin{bmatrix} \frac{1}{\sqrt{Z_{01}}} & 0 & 0 & 0 \\ 0 & \frac{1}{\sqrt{Z_{02}}} & 0 & 0 \\ 0 & 0 & \frac{1}{\sqrt{Z_{03}}} & 0 \\ 0 & 0 & 0 & \frac{1}{\sqrt{Z_{04}}} \end{bmatrix} \begin{bmatrix} V_{r11} & V_{t12} & \cdot & V_{t14} \\ V_{t21} & V_{r22} & \cdot & V_{t24} \\ V_{t31} & \cdot & V_{r33} & V_{t34} \\ V_{t41} & V_{t42} & \cdot & V_{r44} \end{bmatrix} \quad (5.12)$$

5.4 COUPLED LINE DISCONTINUITIES

To characterize coupled line discontinuities, the extraction procedure for single line discontinuities must be modified to account for all incident wave amplitudes. In the coupled line case, excitation of one line (port) leads to an additional



(a)



(b)

Figure 5.8. (a) Magnitude and (b) phase for the asymmetric gap structure.

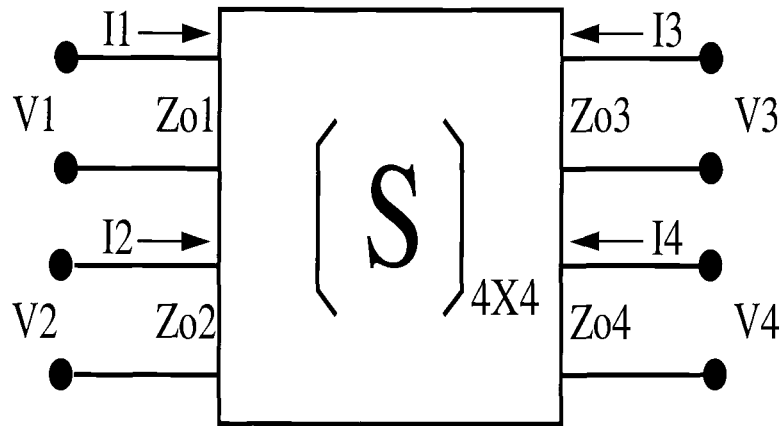


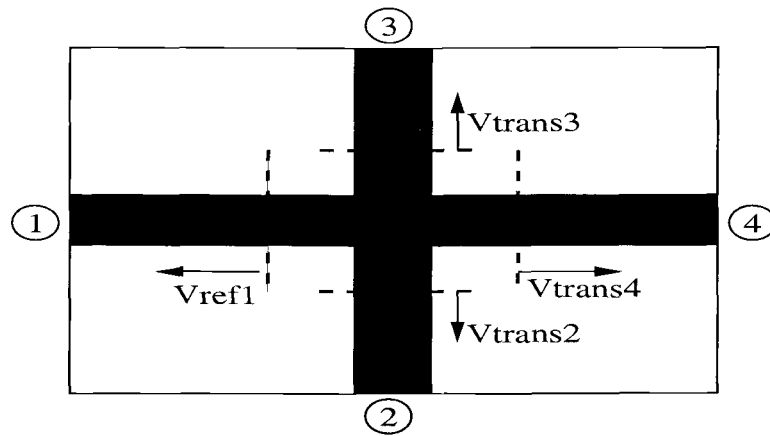
Figure 5.9. Four-port network for the scattering parameters.

excitation on the other line due to coupling. For coupled line structures, the modified normalized wave amplitudes are given by

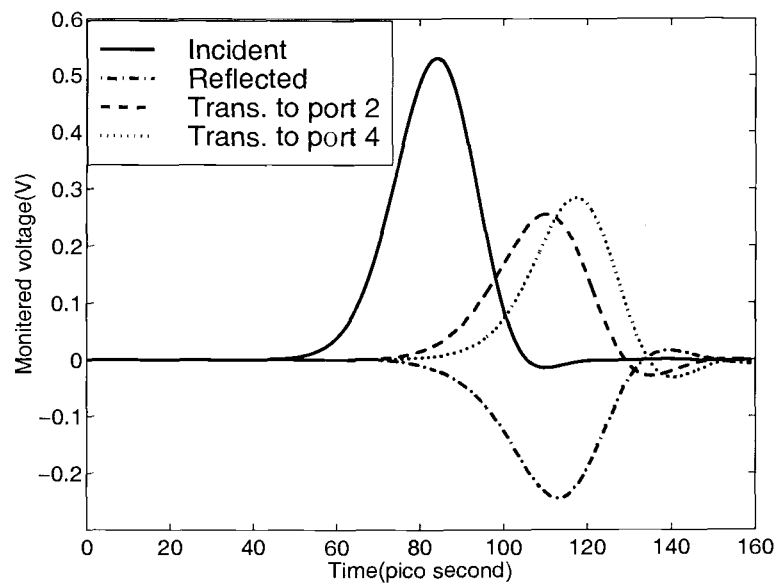
$$\begin{bmatrix} a1 \\ a2 \\ a3 \\ a4 \end{bmatrix} = \begin{bmatrix} \frac{1}{\sqrt{Z_{01}}} & 0 & 0 & 0 \\ 0 & \frac{1}{\sqrt{Z_{02}}} & 0 & 0 \\ 0 & 0 & \frac{1}{\sqrt{Z_{03}}} & 0 \\ 0 & 0 & 0 & \frac{1}{\sqrt{Z_{04}}} \end{bmatrix} \begin{bmatrix} V_{i11} & V_{i21} & 0 & 0 \\ V_{i12} & V_{i22} & 0 & 0 \\ 0 & 0 & V_{i33} & V_{i34} \\ 0 & 0 & V_{i43} & V_{i44} \end{bmatrix} \quad (5.13)$$

$$\begin{bmatrix} b1 \\ b2 \\ b3 \\ b4 \end{bmatrix} = \begin{bmatrix} \frac{1}{\sqrt{Z_{01}}} & 0 & 0 & 0 \\ 0 & \frac{1}{\sqrt{Z_{02}}} & 0 & 0 \\ 0 & 0 & \frac{1}{\sqrt{Z_{03}}} & 0 \\ 0 & 0 & 0 & \frac{1}{\sqrt{Z_{04}}} \end{bmatrix} \begin{bmatrix} V_{r11} & V_{r12} & V_{t13} & V_{t14} \\ V_{r21} & V_{r22} & V_{t23} & V_{t24} \\ V_{t31} & V_{t32} & V_{r33} & V_{r34} \\ V_{t41} & V_{t42} & V_{r43} & V_{r44} \end{bmatrix} \quad (5.14)$$

where V_{i21} and V_{i12} are the additional incident wave voltages on the coupled line for port 1 and port 2 excitation, respectively.



(a)



(b)

Figure 5.10. (a) Symmetric cross-junction structure and (b) monitored voltages

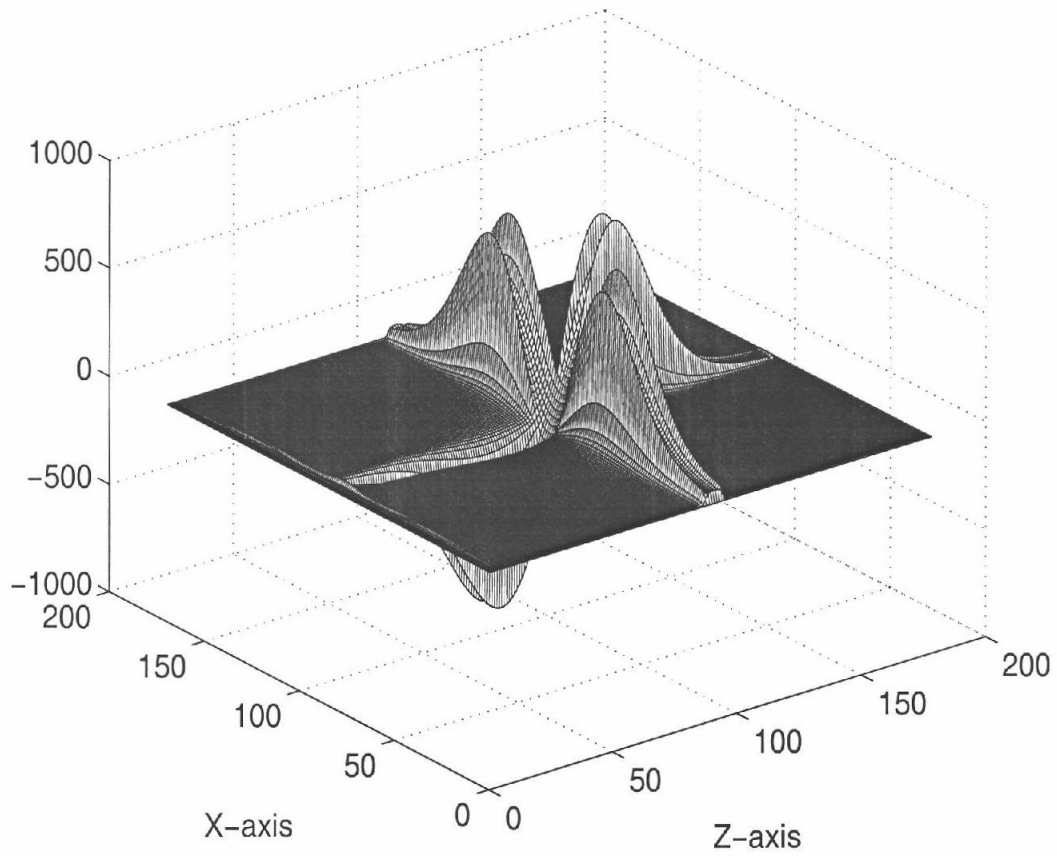
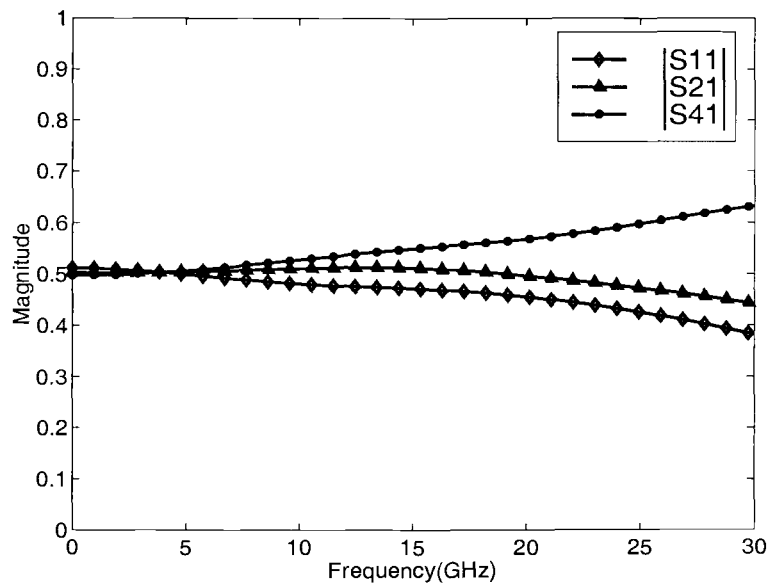
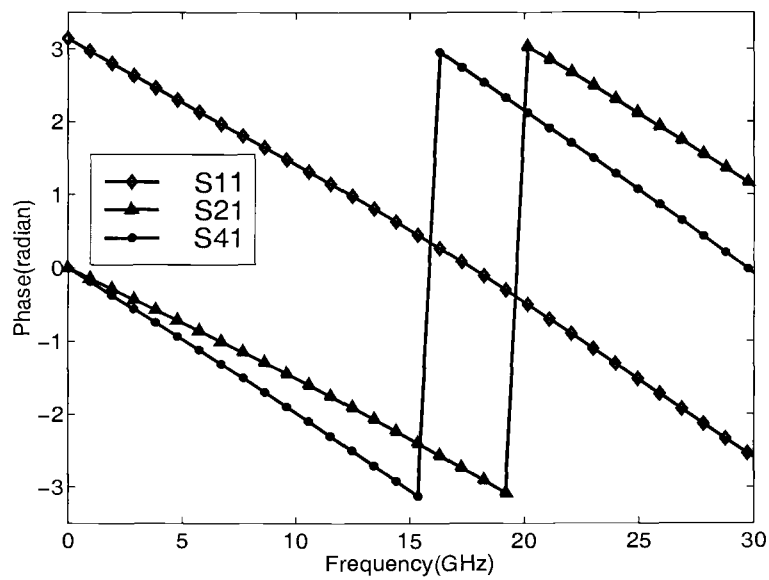


Figure 5.11. Propagation of waveform at 900 time steps for symmetric cross-junction structure.



(a)



(b)

Figure 5.12. (a) Magnitude and (b) phase of scattering parameters for symmetric cross-junction structure.

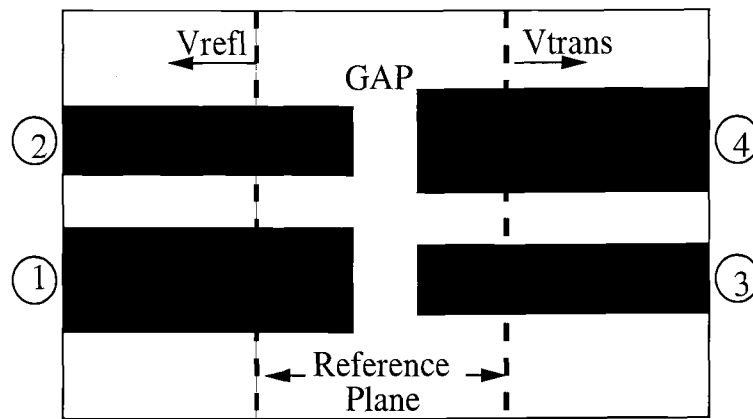


Figure 5.13. Asymmetric coupled gap structure.

5.4.1 ASYMMETRIC COUPLED GAP

The asymmetric coupled gap structure is shown in Figure 5.13. The parameters used for the example structure are: conductor widths $W1 = W4 = 600\mu\text{m}$, $W2 = W3 = 300\mu\text{m}$, gap between the two edges G and spacing between the two conductors $S = G = 300\mu\text{m}$, and $\epsilon_r = 9.6$. Figure 5.14 shows the propagation waveform at 1500 time steps. The computed S parameters are shown in Figures 5.15 and 5.16.

5.4.2 ASYMMETRIC COUPLED STEP-IN-WIDTH

The asymmetric coupled step-in-width structure is shown in Figure 5.17. The procedure for finding the S parameters and the specifications used are the same as for the asymmetric coupled gap. Figure 5.18 shows the propagation waveform at 1200 time steps. The computed S parameters for asymmetric coupled step-in-width are shown in Figures 5.19 and 5.20.

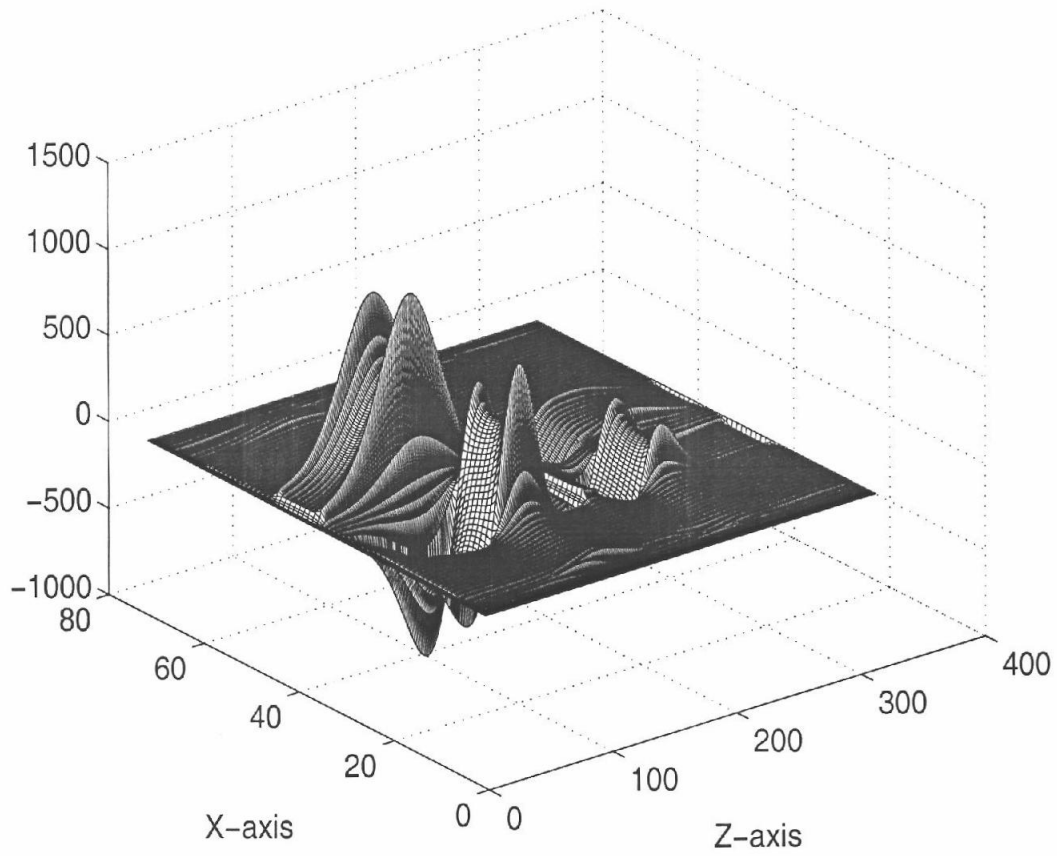
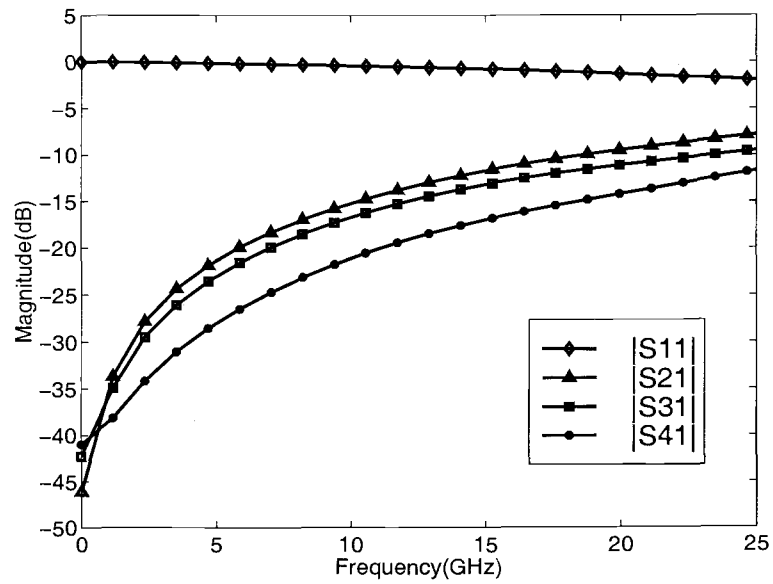
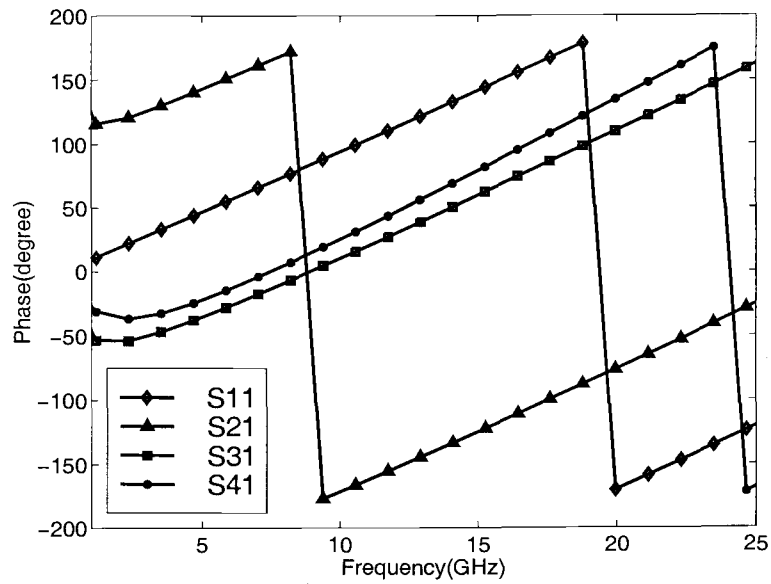


Figure 5.14. propagation waveform at 1500 time steps of asymmetric coupled gap.

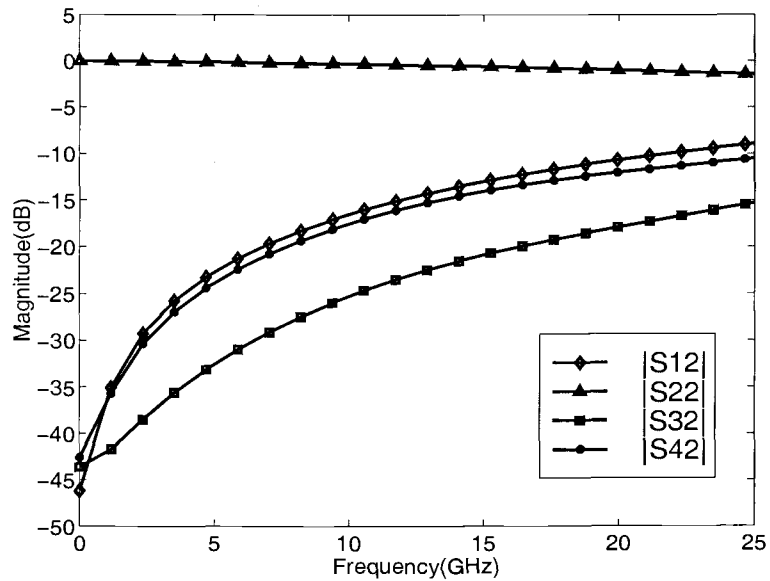


(a)

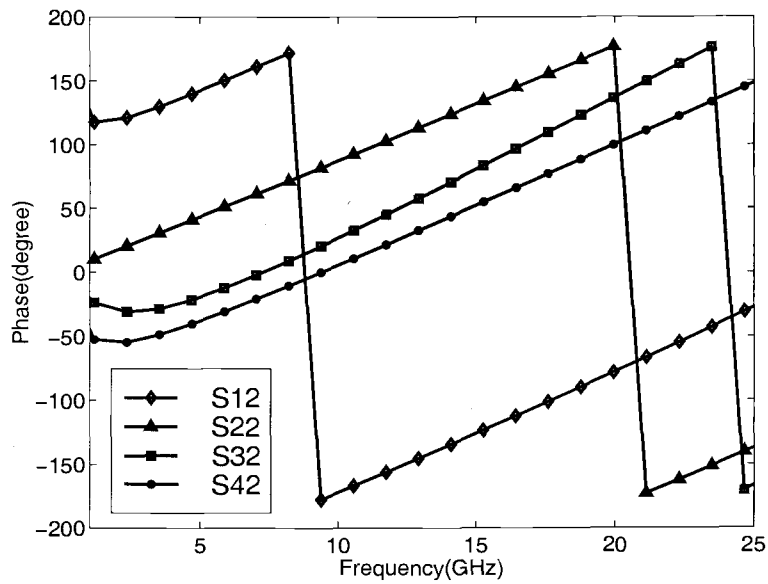


(b)

Figure 5.15. (a) Magnitude and (b) phase of scattering parameters for asymmetric coupled gap.



(a)



(b)

Figure 5.16. (a) Magnitude and (b) phase of scattering parameters for asymmetric coupled gap.

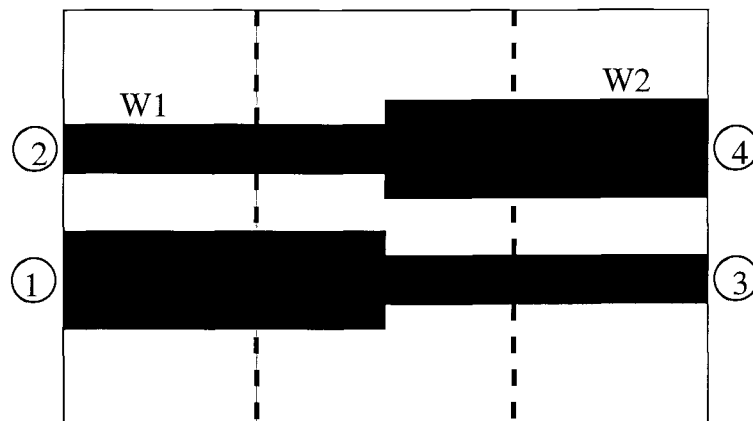


Figure 5.17. Asymmetric coupled step-in-width structure.

5.5 CONCLUDING REMARKS

In this chapter, the FDTD method has been used to find the scattering parameters for various types of single and coupled discontinuity structures. A new extraction procedure has been developed for coupled line discontinuities to take into account the additional incident wave on the coupled line. The scattering parameters for both single and coupled line structures with discontinuities show a frequency-dependence which would not be obtained with quasi-static methods.

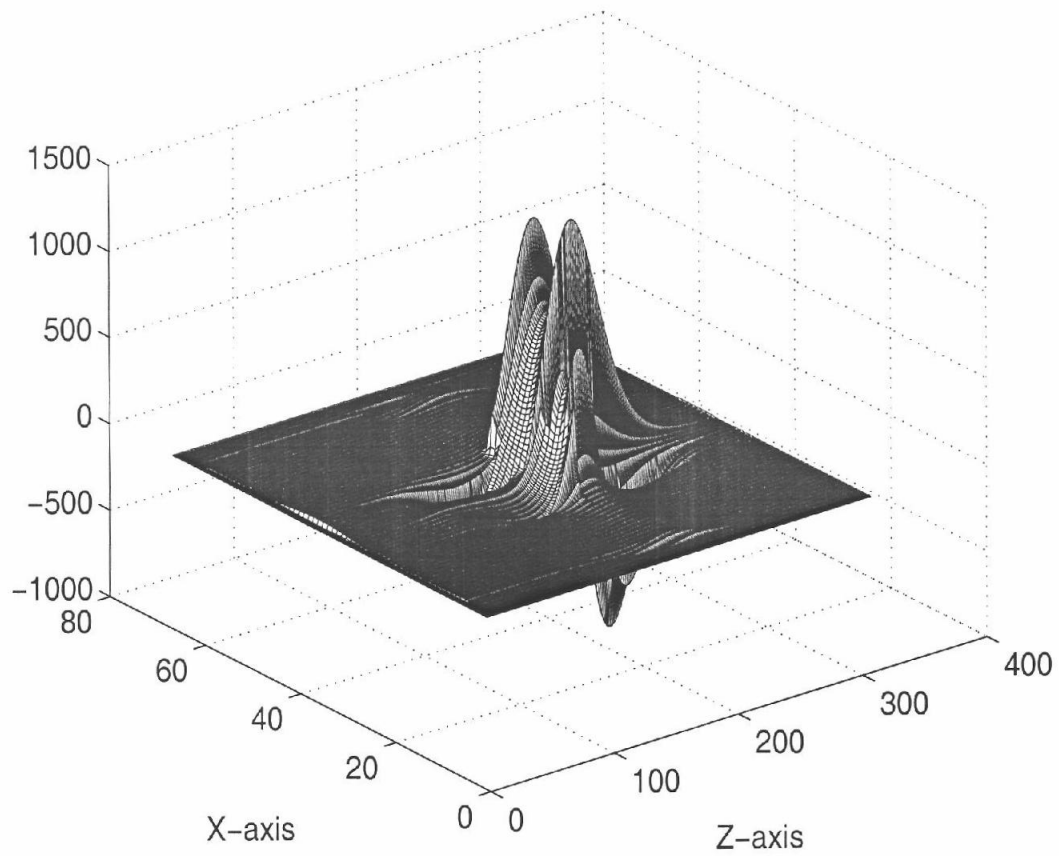
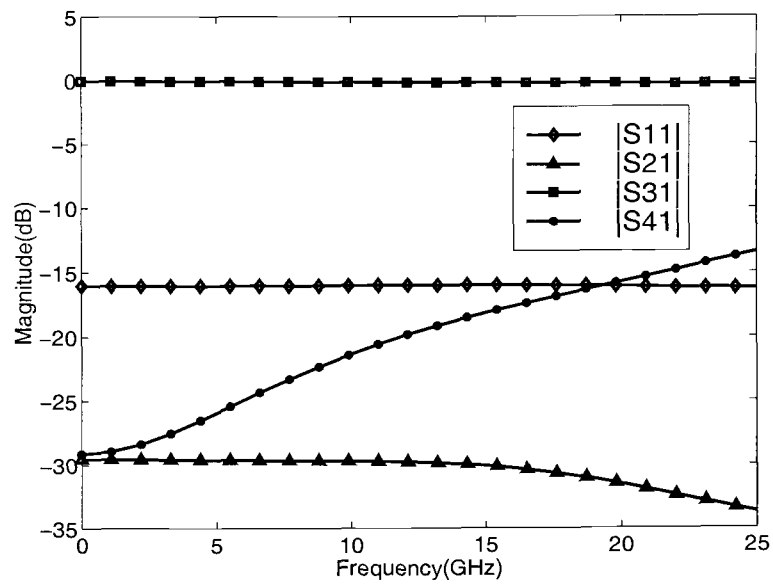
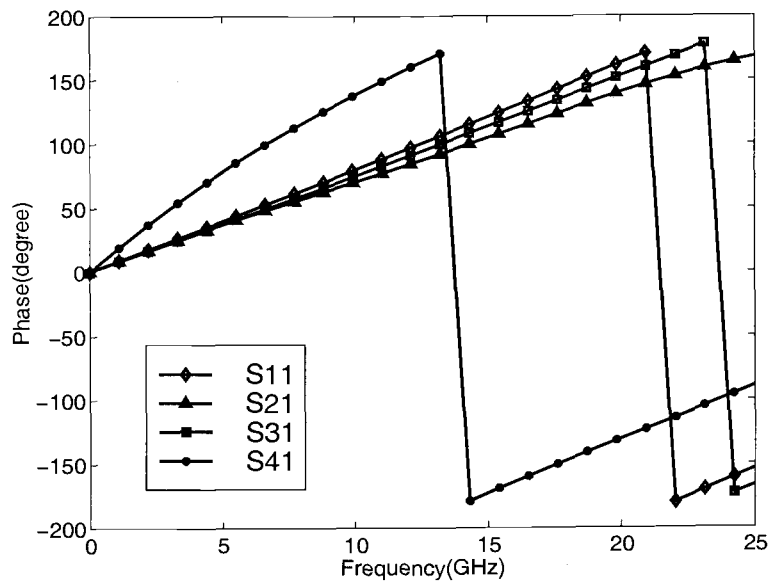


Figure 5.18. Propagation waveform at 1200 time steps for asymmetric coupled step-in-width structure.

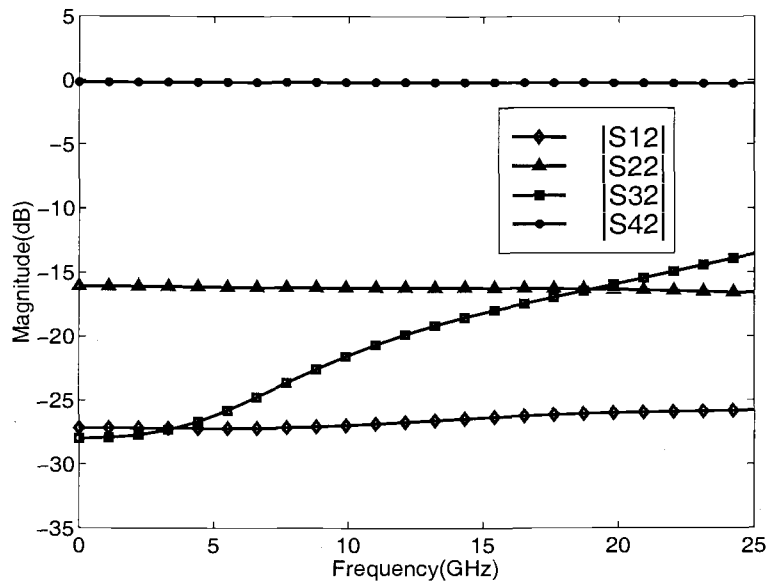


(a)

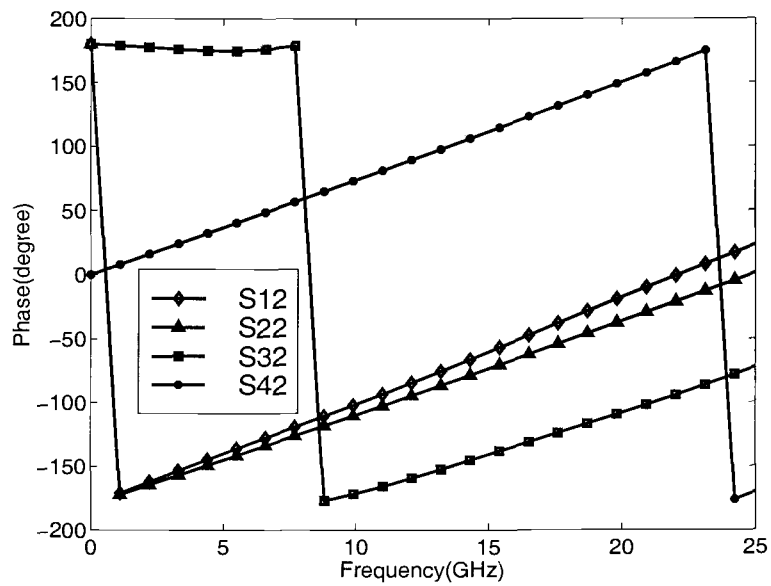


(b)

Figure 5.19. (a) Magnitude and (b) phase of asymmetric coupled step structure at port 1 excitation.



(a)



(b)

Figure 5.20. (a) Magnitude and (b) phase of asymmetric coupled step structure at port 2 excitation.

Chapter 6

CONCLUSION AND SUGGESTIONS FOR FUTURE WORK

This thesis described a new CAD-oriented methodology for the full-wave broadband characterization of coupled microstrip structures for RF/microwave and high-speed digital circuits. The characterization methodology is based on the finite difference time domain (FDTD) technique combined with a systematic extraction procedure using the normal mode approach and multiport network concepts.

After reviewing the FDTD technique and introducing the basic extraction method in Chapter 2, the characterization approach for determining the frequency-dependent propagation characteristics of uniform coupled lines on a lossless substrate was described in Chapter 3. In the proposed approach, the $2n$ -port admittance matrix corresponding to n uniform coupled lines is extracted from the port voltages and currents, which in turn provides the frequency-dependent distributed inductance and capacitance matrices. To illustrate the technique, several practical coupled line structures, including an asymmetric three-line structure, were analyzed, and results were found to be in good agreement with those obtained with a full-wave spectral-domain method.

In Chapter 4, the characterization methodology was applied to microstrip lines on lossy silicon substrate. As an example, the frequency-dependent propagation characteristics and distributed line parameters for single and symmetric coupled microstrip lines were extracted from FDTD simulation. Results show that the lossy substrate can significantly affect the transmission line characteristics. To reduce the substrate effects on the microstrip characteristics, a new substrate shielding structure consisting of grounded vertical lines at the silicon/oxide interface was examined. It was shown for a single and symmetric coupled mi-

crostrip lines that the substrate shield leads to a reduction in transmission line loss without significantly changing the characteristic impedance and effective permittivity of the microstrip structure.

In Chapter 5, the FDTD approach was combined with a new extraction procedure to determine the characteristics of several discontinuities in single and coupled microstrip lines. The new extraction procedure is based on successive excitation of each port and determination of the voltages for the incident and reflected waves. The method was validated for a single symmetric gap and single step discontinuity. Results were also shown for a general single asymmetric gap and a cross-junction. The approach was extended to coupled line discontinuities by including the additional excitation in the coupled line. Examples were shown for a coupled gap and coupled step discontinuity. In all cases, the scattering parameters for the discontinuities showed significant frequency-dependence, which would not be included in solutions based on quasi-static techniques.

Within this subject of study are plenty of opportunities for improvement, development and innovation. For future work there are many topics which could be investigated further. Several avenues of future research may include:

1. Application of the FDTD method to the simulation of multiple coupled microstrip lines on highly doped lossy media.
2. Analysis of non-uniform structures such as tapered lines.
3. Characterization of coplanar waveguides (CPW) and coplanar strips (CPS) on both lossless and lossy substrates.
4. Application of the method to study other types of substrate shielding structures.
5. Application of the method to other coupled discontinuities as well as discontinuities in microstrip lines on lossy substrates.

BIBLIOGRAPHY

- [1] T. Shibata and T. Kimura, "Analysis of microstrip circuits using three-dimensional full-wave electromagnetic field analysis in the time domain," *IEEE Trans. Microwave Theory Tech.*, vol. 36, pp. 1064–1070, June 1988.
- [2] I. Wolff, "Finite difference time-domain simulation of electromagnetic fields and microwave circuits," *International Journal of Numerical Modeling.*, vol. 5, pp. 163–182, Oct. 1992.
- [3] R. Mittra and P. Harms, "A general purpose maxwell solver for the extraction of equivalent circuits of electronic package components for circuit simulation," *IEEE Trans. Circuits and Syst. 1*, vol. 39, pp. 964–973, Nov. 1992.
- [4] V. Tripathi and J. Rettig, "A spice model for multiple coupled microstrips and other transmission lines," *IEEE Trans. Microwave Theory Tech.*, vol. 33, pp. 1513–1518, Dec. 1985.
- [5] V. Tripathi and A. Hill, "Equivalent circuit modeling of losses and dispersion in single and coupled lines for microwave and millimeter-wave integrated circuits," *IEEE Trans. Microwave Theory Tech.*, vol. 36, pp. 256–262, Feb. 1988.
- [6] V. Tripathi and H. Lee, "Spectral-domain computation of characteristic impedances and multiport parameters of multiple coupled microstrip lines," *IEEE Trans. Microwave Theory Tech.*, vol. 37, pp. 215–221, Jan. 1989.
- [7] A. Deutsch, "When are transmission-line effects important for on-chip interconnections?," *IEEE Trans. Microwave Theory Tech.*, vol. 45, pp. 1836–1846, Oct. 1997.

- [8] T. Yue and S. Wong, "On-chip spiral inductors with patterned ground shields for si-based RF IC's," *IEEE Journal of Solid-State circuits.*, vol. 33, pp. 743–751, May 1998.
- [9] T. Itoh, "Numerical techniques for microwave and millimeter-wave passive structures," John Wiley & sons, 1989.
- [10] K. Yee, "Numerical solution of initial boundary value problem involving maxwell's equations in isotropic media," *IEEE Trans. Antennas and Propagation*, vol. 14, pp. 302–307, May 1966.
- [11] D. Choi and W. Hoefer, "The finite-difference time-domain method and its application to eigenvalue problems," *IEEE Trans. Microwave Theory Tech.*, vol. 34, pp. 1464–1470, Dec. 1986.
- [12] X. Zhang, J. Fang and Y. Liu, "Calculations of the dispersive characteristics of microstrips by the time-domain finite difference method," *IEEE Trans. Microwave Theory Tech.*, vol. 36, pp. 263–267, Feb. 1988.
- [13] A. Taflove, "Review of the formulation and applications of the finite-difference time-domain method for numerical modeling of electromagnetic wave interactions with arbitrary structures," *Wave Motion*, vol. 10, pp. 547–582, July 1988.
- [14] A. Taflove and K. Umashankar, "Review of FD-TD numerical modeling of electromagnetic wave scattering and radar cross section," *Proceedings of the IEEE.*, vol. 77, pp. 682–699, May 1989.
- [15] G. Liang and K. Mei, "Full-wave analysis of coplanar waveguide and slotline using the time-domain finite-difference method," *IEEE Trans. Microwave Theory Tech.*, vol. 37, pp. 1949–1957, Dec. 1989.
- [16] T. Shibata and E. Sano, "Characterization of MIS structure coplanar transmission lines for investigation of signal propagation in integrated circuits," *IEEE Trans. Microwave Theory Tech.*, vol. 38, pp. 881–890, July 1990.
- [17] L. Wu and Y. Chang, "Characterization of the shielding effects on the frequency-dependent effective dielectric constant of a waveguide-shielded microstrip using the finite-difference time-domain method," *IEEE Trans. Microwave Theory Tech.*, vol. 39, pp. 1688–1693, Oct. 1991.

- [18] X. Zhang and K. Mei, "Time-domain finite difference approach to the calculation of the frequency-dependent characteristics of microstrip discontinuities," *IEEE Trans. Microwave Theory Tech.*, vol. 36, pp. 1775–1787, Dec. 1988.
- [19] D. Sheen, S. Ali and J. Kong, "Application of the three-dimensional finite-difference time-domain method to the analysis of planar microstrip circuits," *IEEE Trans. Microwave Theory Tech.*, vol. 38, pp. 849–857, July 1990.
- [20] D. Sheen, "Numerical modeling of microstrip circuits and antennas," *Ph.D dissertation, M.I.T.*, Boston, Massachusetts, June 1991.
- [21] J. Moore and H. Ling, "Characterization of a 90 degree microstrip bend with arbitrary miter via time-domain finite difference method," *IEEE Trans. Microwave Theory Tech.*, vol. 38, pp. 405–410, Apr. 1990.
- [22] I. Feix and B. Jecko, "Harmonical characterization of a microstrip bend via the finite difference time domain method," *IEEE Trans. Microwave Theory Tech.*, vol. 40, pp. 955–961, May 1992.
- [23] A. Reineix and B. Jecko, "Analysis of microstrip patch antennas using finite difference time domain method," *IEEE Trans. Antennas and Propagation*, vol. 37, pp. 1361–1369, Nov. 1989.
- [24] J. Maloney and W. Scott, "Accurate computation of the radiation from simple antennas using the finite-difference time-domain method," *IEEE Trans. Antennas and Propagation*, vol. 38, pp. 1059–1068, July 1990.
- [25] C. Wu, K. Wu and J. Litva, "Accurate characterization of planar printed antennas using finite-difference time-domain method," *IEEE Trans. Antennas and Propagation*, vol. 40, pp. 526–534, May 1992.
- [26] T. Kashiwa and I. Fukai, "Analysis of microstrip antennas on a curved surface using the conformal grids FD-TD method," *IEEE Trans. Antennas and Propagation*, vol. 42, pp. 423–427, Mar. 1994.
- [27] M. Gibbons and J. Prince, "Finite-difference time-domain analysis of pulse propagation in multichip module interconnects," *IEEE Trans. Components, Hybrids, and Manufacturing Technology*, vol. 16, pp. 490–498, Aug. 1993.

- [28] C. Lam and P. Nuytkens, "Three-dimensional modeling of multichip module interconnects," *IEEE Trans. Components, Hybrids, and Manufacturing Technology*, vol. 16, pp. 699–704, Nov. 1993.
- [29] R. Luebbers, K. Kunz and F. Hunsberger, "A finite-difference time-domain near zone to far zone transformation," *IEEE Trans. Antennas and Propagation*, vol. 39, pp. 429–433, Apr. 1991.
- [30] J. Moerlose and D. Zutter, "Surface integral representation radiation boundary condition for the FDTD method," *IEEE Trans. Antennas and Propagation*, vol. 41, pp. 890–896, July 1993.
- [31] O. Ramahi, "Near- and far-field calculations in FDTD simulations using Kirchhoff surface integral representation," *IEEE Trans. Antennas and Propagation*, vol. 45, pp. 753–759, July 1997.
- [32] K. Remley, A. Weisshaar and V. Tripathi, "Characterization of near- and far-field radiation from ultrafast electronic systems," *IEEE Trans. Microwave Theory Tech.*, vol. 46, pp. 2476–2483, Dec. 1998.
- [33] A. Taflove and M. Brodwin, "Numerical solution of steady-state electromagnetic scattering problems using the time-dependent Maxwell's equations," *IEEE Trans. Microwave Theory Tech.*, vol. 23, pp. 623–630, Feb. 1975.
- [34] A. Taflove, "Application of the finite-difference time-domain method to sinusoidal steady-state electromagnetic-penetration problems," *IEEE Trans. Electromagnetic Comp.*, vol. 22, pp. 191–202, Aug. 1980.
- [35] B. Engquist and A. Majda, "Absorbing boundary conditions for the numerical solution of waves," *Mathematics of Computation*, vol. 31, pp. 629–651, Nov. 1977.
- [36] G. Mur, "Absorbing boundary conditions for the finite-difference approximation of the time-domain electromagnetic-field equations," *IEEE Trans. Electromagnetic Comp.*, vol. 23, pp. 377–382, May 1981.
- [37] R. Higdon, "Absorbing boundary conditions for difference approximations to the multi-dimensional wave equations," *Mathematics of Computation*, vol. 47, pp. 437–459, Sept. 1986.

- [38] R. Higdon, "Numerical absorbing boundary conditions for the wave equation," *Mathematics of Computation*, vol. 49, pp. 65–90, Sept. 1987.
- [39] J. Berenger, "A perfectly matched layer for the absorption of electromagnetic waves," *Journal of Computational Physics*, vol. 114, pp. 185–200, Sept. 1994.
- [40] J. Berenger, "Perfectly matched layer for the FDTD solution of wave-structure interaction problems," *IEEE Trans. Antennas and Propagation*, vol. 44, pp. 110–117, Jan. 1996.
- [41] M. Falconer, "Three dimensional electromagnetic FDTD simulation of general lossy structures with nonuniform grid spacing," *Ph.D dissertation, Oregon State University, Corvallis, OR*, June 1997.
- [42] V. Tripathi, "Asymmetric coupled transmission lines in an inhomogeneous medium," *IEEE Trans. Microwave Theory Tech.*, vol. 23, pp. 734–739, Sept. 1975.
- [43] V. Tripathi, "On the analysis of symmetrical three-line microstrip circuits," *IEEE Trans. Microwave Theory Tech.*, vol. 25, pp. 726–729, Sept. 1977.
- [44] V. Tripathi, "The scattering parameters and directional coupler analysis of characteristically terminated three-line structures in an inhomogeneous medium," *IEEE Trans. Microwave Theory Tech.*, vol. 29, pp. 22–26, Jan. 1981.
- [45] E. Cristal, "Coupled-transmission-line directional couplers with coupled lines of unequal characteristic impedances," *IEEE Trans. Microwave Theory Tech.*, vol. 14, pp. 337–346, July 1966.
- [46] G. Zysman and A. Johnson, "Coupled transmission line networks in an inhomogeneous dielectric medium," *IEEE Trans. Microwave Theory Tech.*, vol. 17, pp. 753–759, Oct. 1969.
- [47] M. Krage and G. Haddad, "Characteristics of coupled microstrip transmission lines-I: Coupled-mode formulation of inhomogeneous lines," *IEEE Trans. Microwave Theory Tech.*, vol. 18, pp. 217–228, Apr. 1970.
- [48] F. Chang, "Transient analysis of lossless coupled transmission lines in a non-

- homogeneous dielectric medium," IEEE Trans. Microwave Theory Tech., vol. 18, pp. 616–626, Sept. 1970.
- [49] Y. Fukuoka, Q. Zhang and T. Itoh, "Analysis of multilayer interconnection lines for a high-speed digital integrated circuit," IEEE Trans. Microwave Theory Tech., vol. 33, pp. 527–532, June 1985.
- [50] A. Djordjevic and R. Harrington, "Time-domain response of multiconductor transmission lines," Proceedings of the IEEE., vol. 75, pp. 743–765, June 1987.
- [51] F. Romeo and M. Santomauro, "Time-domain simulation of n coupled transmission lines," IEEE Trans. Microwave Theory Tech., vol. 35, pp. 131–137, Feb. 1987.
- [52] K. Marx and R. Eastin, "A configuration-oriented spice model for multiconductor transmission lines with homogeneous dielectrics," IEEE Trans. Microwave Theory Tech., vol. 38, pp. 1123–1129, Aug. 1990.
- [53] R. Wang and O. Wing, "A circuit model of a system of VLSI interconnects for time response computation," IEEE Trans. Microwave Theory Tech., vol. 39, pp. 688–693, Apr. 1991.
- [54] T. Dhaene and D. Zutter, "Analysis and modeling of coupled dispersive interconnection lines," IEEE Trans. Microwave Theory Tech., vol. 40, pp. 2103–2105, Nov. 1992.
- [55] K. Yasumoto, "Coupled-mode formulation of multilayered and multiconductor transmission lines," IEEE Trans. Microwave Theory Tech., vol. 44, pp. 585–590, Apr. 1996.
- [56] M. Schamberger and R. Mittra, "Parameter extraction and correction for transmission lines and discontinuities using the finite-difference time-domain method," IEEE Trans. Microwave Theory Tech., vol. 44, pp. 919–925, June 1996.
- [57] C. Paul, "Decoupling the multiconductor transmission line equations," IEEE Trans. Microwave Theory Tech., vol. 44, pp. 1429–1440, Aug. 1996.
- [58] J. Zhao and Z. Li, "A time-domain full-wave extraction method of frequency-

- dependent equivalent circuit parameters of multiconductor interconnection lines," *IEEE Trans. Microwave Theory Tech.*, vol. 45, pp. 23–31, Jan. 1997.
- [59] Y. Kim, R. Settaluri and V. Tripathi, "Modeling and characterization of multiple coupled lines in multilayer structure using FDTD," *Proc. International symposium on Microelectronics.*, vol. 1, pp. 364–369, Nov. 1998.
- [60] Y. Kim, R. Settaluri and V. Tripathi, "Extraction of multiple coupled line parameters using FDTD simulation," *Proceedings of IEE Microwaves, Antennas and Propagation*, accepted.
- [61] V. Tripathi and N. Orhanovic, "Time-domain characterization and analysis of dispersive dissipative interconnects," *IEEE Trans. Circuits Syst.*, vol. 39, pp. 938–945, Nov. 1992.
- [62] Y. Chin, "Analysis and applications of multiple coupled line structures in an inhomogeneous medium," *Ph.D dissertation, Oregon State University, Corvallis, OR*, June 1983.
- [63] H. Guckel and I. Palocz, "A parallel-plate waveguide approach to micro-miniaturized, planar transmission lines for integrated circuits," *IEEE Trans. Microwave Theory Tech.*, vol. 15, pp. 468–476, Aug. 1967.
- [64] H. Hasegawa and H. Yanai, "Properties of microstrip line on Si-SiO₂ system," *IEEE Trans. Microwave Theory Tech.*, vol. 19, pp. 869–881, Nov. 1971.
- [65] V. Tripathi and R. Bucolo, "A simple network analog approach for the quasi-static characteristics of general lossy, anisotropic, layered structures," *IEEE Trans. Microwave Theory Tech.*, vol. 33, pp. 1458–1464, Dec. 1985.
- [66] M. Abushaaban and S. Scanlan, "Modal circuit decomposition of lossy multiconductor transmission lines," *IEEE Trans. Microwave Theory Tech.*, vol. 44, pp. 1046–1057, July 1996.
- [67] S. Seki and H. Hasegawa, "Analysis of crosstalk in very high-speed LSI/VLSI's using a coupled multiconductor microstrip line model," *IEEE Trans. Microwave Theory Tech.*, vol. 32, pp. 1715–1720, Dec. 1984.
- [68] H. Hasegawa and S. Seki, "Analysis of interconnection delay on very high-

- speed LSI/VLSI chips using an mis microstrip line model," *IEEE Trans. Microwave Theory Tech.*, vol. 32, pp. 1721–1727, Dec. 1984.
- [69] G. Ghione and G. Vecchi, "Modeling of multiconductor buses and analysis of crosstalk, propagaion delay, and pulse distortion in high-speed gaas logic circuits," *IEEE Trans. Microwave Theory Tech.*, vol. 37, pp. 445–456, Mar. 1989.
- [70] J. Gilb and C. Balanis, "Pulse distortion on multilayer coupled microstrip lines," *IEEE Trans. Microwave Theory Tech.*, vol. 37, pp. 1620–1628, Oct. 1989.
- [71] J. Gilb and C. Balanis, "Transient analysis of distortion and coupling in lossy coupled microstrips," *IEEE Trans. Microwave Theory Tech.*, vol. 38, pp. 1894–1899, Dec. 1990.
- [72] J. Gilb and C. Balanis, "Asymmetric, multi-conductor low-coupling structures for high-speed , high-density digital interconnects," *IEEE Trans. Microwave Theory Tech.*, vol. 39, pp. 2100–2106, Dec. 1991.
- [73] Y. Fukuoka and T. Itoh, "Analysis of slow-wave coplanar waveguide for monolithic integrated circuits," *IEEE Trans. Microwave Theory Tech.*, vol. 31, pp. 567–573, July 1983.
- [74] R. Sorrentino and A. Silbermann, "Characteristics of Metal - Insulator - Semiconductor coplanar waveguides for monolithic microwave circuits," *IEEE Trans. Microwave Theory Tech.*, vol. 32, pp. 410–416, Apr. 1984.
- [75] G. Ghione and C. Naldi, "Coplanar waveguides for mmic applications: effect of upper shielding, conductor backing, finite-extent ground planes, and line-to-line coupling," *IEEE Trans. Microwave Theory Tech.*, vol. 35, p-p. 260–267, Mar. 1987.
- [76] Y. Kwon and K. Champlin, "Quasi-tem analysis of "Slow-wave" mode propagation on coplanar microstructure MIS transmission lines," *IEEE Trans. Microwave Theory Tech.*, vol. 35, pp. 545–551, June 1987.
- [77] T. Shibata and E. Sano, "Characterization of mis structure coplanar transmission lines for investigation of signal propagation in integrated circuits," *IEEE Trans. Microwave Theory Tech.*, vol. 38, pp. 881–890, July 1990.

- [78] F. Mesa, G. Cano and M. Horno, "On the quasi-tem and full-wave approaches applied to coplanar multistrip on lossy dielectric layered media," *IEEE Trans. Microwave Theory Tech.*, vol. 40, pp. 524–531, Mar. 1992.
- [79] V. Milanovic, M. Gaitan and M. Zaghoul, "Micromachined microwave transmission lines in CMOS technology," *IEEE Trans. Microwave Theory Tech.*, vol. 45, pp. 630–635, May 1997.
- [80] C. Warns and H. Schumann, "Transmission lines and passive elements for multilayer coplanar circuits on silicon," *IEEE Trans. Microwave Theory Tech.*, vol. 46, pp. 616–622, May 1998.
- [81] V. Milanovic, M. Ozgur and M. Zaghoul, "Characterization of broad-band transmission for coplanar waveguides on CMOS silicon substrate," *IEEE Trans. Microwave Theory Tech.*, vol. 46, pp. 632–640, May 1998.
- [82] W. Heinrich, J. Gerdes and K. Strohm, "Coplanar passive elements on Si substrate for frequencies up to 110 ghz," *IEEE Trans. Microwave Theory Tech.*, vol. 46, pp. 709–712, May 1998.
- [83] A. Goel and Y. Huang, "Modeling of crosstalk among the gaas-based VLSI interconnections," *Proceedings of the IEE.*, vol. 136, pp. 361–368, Dec. 1989.
- [84] V. Tripathi and R. Bucolo, "Analysis and modeling of multilevel parallel and crossing interconnection lines," *IEEE Trans. Electron Devices.*, vol. 34, pp. 650–658, Mar. 1987.
- [85] C. Chan and R. Mittra, "The propagation characteristics of signal lines embedded in a multilayered structure in the presence of a periodically perforated ground plane," *IEEE Trans. Microwave Theory Tech.*, vol. 36, pp. 968–975, June 1988.
- [86] T. Uwano and T. Itoh, "Characterization of strip line crossing by transverse resonance analysis," *IEEE Trans. Microwave Theory Tech.*, vol. 35, pp. 1369–1376, Dec. 1987.
- [87] S. Koike and I. Fukai, "Transient analysis of coupling between crossing lines in three-dimensional space," *IEEE Trans. Microwave Theory Tech.*, vol. 35, pp. 67–71, Jan. 1987.

- [88] W. Veit and R. Pregla, "Coupling of crossed planar multiconductor systems," *IEEE Trans. Microwave Theory Tech.*, vol. 38, pp. 265–269, Mar. 1990.
- [89] R. Horton, "The electrical characterization of a right-angled bend in microstrip line," *IEEE Trans. Microwave Theory Tech.*, vol. 21, pp. 427–429, June 1973.
- [90] A. Gopinath and B. Easter, "Moment method of calculating discontinuity inductance of microstrip right-angled bends," *IEEE Trans. Microwave Theory Tech.*, vol. 22, pp. 880–883, Oct. 1974.
- [91] B. Easter, "The equivalent circuit of some microstrip discontinuities," *IEEE Trans. Microwave Theory Tech.*, vol. 23, pp. 655–660, Aug. 1975.
- [92] A. Gopinath and I. Stephenson, "Equivalent circuit parameters of microstrip step change in width and cross junctions," *IEEE Trans. Microwave Theory Tech.*, vol. 24, pp. 142–144, Mar. 1976.
- [93] W. Menzel and I. Wolff, "A method for calculating the frequency-dependent properties of microstrip discontinuities," *IEEE Trans. Microwave Theory Tech.*, vol. 25, pp. 107–112, Feb. 1977.
- [94] C. Gupta and A. Gopinath, "Equivalent circuit capacitance of microstrip step change in width," *IEEE Trans. Microwave Theory Tech.*, vol. 25, pp. 819–822, Oct. 1977.
- [95] R. Douville and D. James, "Experimental study of symmetric microstrip bends and their compensation," *IEEE Trans. Microwave Theory Tech.*, vol. 26, pp. 175–182, Mar. 1978.
- [96] P. Katehi and N. Alexopoulos, "Frequency-dependent characteristics of microstrip discontinuities in millimeter-wave integrated circuits," *IEEE Trans. Microwave Theory Tech.*, vol. 33, pp. 1029–1035, Oct. 1985.
- [97] R. Jackson and D. Pozar, "Full-wave analysis of microstrip open-end and gap discontinuities," *IEEE Trans. Microwave Theory Tech.*, vol. 33, pp. 1036–1042, Oct. 1985.
- [98] N. Koster and R. Jansen, "The microstrip step discontinuity : A revised

- description," *IEEE Trans. Microwave Theory Tech.*, vol. 34, pp. 213–223, Feb. 1986.
- [99] R. Jackson, "Full-wave, finite element analysis of irregular microstrip discontinuities," *IEEE Trans. Microwave Theory Tech.*, vol. 37, pp. 81–89, Jan. 1989.
- [100] A. Biswas and V. Tripathi, "Modeling of asymmetric and offset gaps in shielded microstrips and slotlines," *IEEE Trans. Microwave Theory Tech.*, vol. 38, pp. 818–822, June 1990.
- [101] J. Jong and V. Tripathi, "Time-domain characterization of interconnect discontinuities in high-speed circuits," *IEEE Trans. Components, Hybrids, and Manufacturing Technology*, vol. 15, pp. 497–504, Aug. 1992.
- [102] J. Jong and V. Tripathi, "Equivalent circuit modeling of interconnects from time-domain measurements," *IEEE Trans. Components, Hybrids, and Manufacturing Technology*, vol. 16, pp. 119–126, Feb. 1993.

APPENDIX

A.NORMAL MODE PARAMETERS : n Coupled Lines $2n$ -Port System

The general n Coupled Lines $2n$ -Port normal mode parameters are formulated in terms of the admittance matrix.

$$[I]_{2n \times 2n} = [Y]_{2n \times 2n} [V]_{2n \times 2n} \quad (\text{A.1})$$

$$[Y] = \begin{bmatrix} [Y_A] & [Y_B] \\ [Y_B] & [Y_A] \end{bmatrix} \quad (\text{A.2})$$

with

$$\begin{aligned} [Y_A]_{n \times n} &= [Y_{LM}]_{n \times n} * [M_V]_{n \times n} [\text{coth}(\gamma_i d)]_{\text{diag}} [M_I]_{n \times n}^T \\ [Y_B]_{n \times n} &= -[Y_{LM}]_{n \times n} * [M_V]_{n \times n} [\text{csch}(\gamma_i d)]_{\text{diag}} [M_I]_{n \times n}^T \end{aligned}$$

by using the relation of voltage and current eigenvector $[M_V]$ and $[M_I]$ ($[M_I] = [M_V]^{-T}$)

$$\begin{aligned} [Y_A]_{n \times n} &= [Y_{LM}]_{n \times n} * [M_V]_{n \times n} [\text{coth}(\gamma_i d)]_{\text{diag}} [M_V]_{n \times n}^{-1} \\ [Y_B]_{n \times n} &= -[Y_{LM}]_{n \times n} * [M_V]_{n \times n} [\text{csch}(\gamma_i d)]_{\text{diag}} [M_V]_{n \times n}^{-1} \end{aligned}$$

Where

$$[Y_{LM}]_{n \times n} = \begin{bmatrix} Y_{LM11} & Y_{LM12} & \cdot & Y_{LM1n} \\ \cdot & \cdot & \cdot & \cdot \\ \cdot & \cdot & \cdot & \cdot \\ Y_{LMn1} & \cdot & \cdot & Y_{LMnn} \end{bmatrix} \quad (\text{A.3})$$

From equations (3.4) and (3.5), a matrix $[P]$ which includes normal mode parameters $[Y_{LM}]$, $[M_V]$, and $[(\gamma_i d)]_{diag}$ can be defined as

$$\begin{aligned}
[P]_{n \times n} &= [Y_A]_{n \times n}^T [Y_B]_{n \times n}^{-T} \\
&= [M_V]_{n \times n}^{-T} [\coth(\gamma_i d)]_{diag}^T [\operatorname{csch}(\gamma_i d)]_{diag}^{-T} [M_V]_{n \times n}^T \\
&= [M_V]_{n \times n}^{-T} \begin{bmatrix} \frac{\cosh(\gamma_1 d)}{\sinh(\gamma_1 d)} & 0 & \cdot & \cdot & 0 \\ 0 & \frac{\cosh(\gamma_2 d)}{\sinh(\gamma_2 d)} & 0 & \cdot & 0 \\ 0 & 0 & \frac{\cosh(\gamma_3 d)}{\sinh(\gamma_3 d)} & 0 & \cdot \\ 0 & \cdot & \cdot & \cdot & \cdot \\ 0 & \cdot & \cdot & \cdot & \frac{\cosh(\gamma_n d)}{\sinh(\gamma_n d)} \end{bmatrix} \cdot \\
&\quad \begin{bmatrix} \sinh(\gamma_1 d) & 0 & \cdot & \cdot & 0 \\ 0 & \sinh(\gamma_2 d) & 0 & \cdot & 0 \\ 0 & 0 & \sinh(\gamma_3 d) & 0 & \cdot \\ 0 & \cdot & \cdot & \cdot & \cdot \\ 0 & \cdot & \cdot & \cdot & \sinh(\gamma_n d) \end{bmatrix} \cdot [M_V]_{n \times n}^T \quad (\text{A.4})
\end{aligned}$$

This can be simplified to

$$[P]_{n \times n} = [M_V]_{n \times n}^{-T} [\cosh(\gamma_i d)]_{diag}^T [M_V]_{n \times n}^T \quad (\text{A.5})$$

Applying the singular value decomposition

$$[P]_{n \times n} = [E]_{n \times n} [\lambda]_{n \times n} [E]_{n \times n}^{-1} \quad (\text{A.6})$$

The eigenvalues of [P] are found as

$$\begin{bmatrix} \cosh(\gamma_1 d) & 0 & \cdot & \cdot & 0 \\ 0 & \cosh(\gamma_2 d) & 0 & \cdot & 0 \\ 0 & 0 & \cosh(\gamma_3 d) & \cdot & 0 \\ 0 & 0 & \cdot & \cdot & 0 \\ 0 & 0 & \cdot & \cdot & \cosh(\gamma_n d) \end{bmatrix} = [\lambda]_{diag} \quad (\text{A.7})$$

From this, the modal propagation constants are determined as

$$\begin{bmatrix} \gamma_1 d & 0 & \cdot & \cdot & 0 \\ 0 & \gamma_2 d & 0 & \cdot & 0 \\ 0 & 0 & \gamma_3 d & \cdot & 0 \\ 0 & 0 & \cdot & \cdot & 0 \\ 0 & 0 & \cdot & \cdot & \gamma_n d \end{bmatrix} = \cosh^{-1} [\lambda]_{diag} \quad (\text{A.8})$$

$$\gamma_i d = \cosh^{-1} [\lambda_i] \quad (\text{A.9})$$

Where $i = 1$ to n ,

The voltage eigenvector matrix is expressed as

$$[M_v]_{n \times n} = \begin{bmatrix} \beta_{11} & \beta_{12} & \cdot & \cdot & \beta_{1n} \\ \beta_{21} & \beta_{22} & \cdot & \cdot & \beta_{2n} \\ \beta_{31} & \beta_{32} & \cdot & \cdot & \beta_{3n} \\ \cdot & \cdot & \cdot & \cdot & \cdot \\ \beta_{n1} & \beta_{n2} & \cdot & \cdot & \beta_{nn} \end{bmatrix} \quad (\text{A.10})$$

This can be easily normalized as shown below

$$[M_v]_{n \times n} = \begin{bmatrix} 1 & 1 & \cdot & \cdot & 1 \\ \frac{\beta_{21}}{\beta_{11}} & \frac{\beta_{22}}{\beta_{12}} & \cdot & \cdot & \frac{\beta_{2n}}{\beta_{1n}} \\ \frac{\beta_{31}}{\beta_{11}} & \frac{\beta_{32}}{\beta_{12}} & \cdot & \cdot & \frac{\beta_{3n}}{\beta_{1n}} \\ \cdot & \cdot & \cdot & \cdot & \cdot \\ \frac{\beta_{n1}}{\beta_{11}} & \frac{\beta_{n2}}{\beta_{12}} & \cdot & \cdot & \frac{\beta_{nn}}{\beta_{1n}} \end{bmatrix} \quad (\text{A.11})$$

$$[M_v]_{n \times n} = \begin{bmatrix} 1 & 1 & \cdot & \cdot & 1 \\ \alpha_{1,1} & \alpha_{1,2} & \cdot & \cdot & \alpha_{1,n} \\ \alpha_{2,1} & \alpha_{2,2} & \cdot & \cdot & \alpha_{2,n} \\ \cdot & \cdot & \cdot & \cdot & \cdot \\ \alpha_{n-1,1} & \alpha_{n-1,2} & \cdot & \cdot & \alpha_{n-1,n} \end{bmatrix} \quad (\text{A.12})$$